



MONASH University

**Towards Augmented Reality:
MRI-TRUS Fusion for Prostate
Cancer Interventions**

Mohammad Ali Jan Ghasab

A thesis submitted for the degree of Doctor of Philosophy at
Monash University in 2019

Clayton School of Information Technology

Copyright Notice

©Mohammad Ali Jan Ghasab (2019)

I certify that I have made all reasonable efforts to secure copyright permissions for third-party content included in this thesis and have not knowingly added copyright content to my work without the owner's permission.

Abstract

Prostate cancer is one of the most commonly occurring cancers in males. Medical imaging plays an important role in its early detection and treatment. Transrectal ultrasound (TRUS) and magnetic resonance imaging (MRI) are two commonly used medical imaging technologies. TRUS is used intra-operatively to guide biopsies and treatments such as brachytherapy. However, TRUS images have a low signal to noise ratio, with poor contrast, making it difficult to differentiate between tissue types and identify anatomical structures. This potentially leads to high false negative rates in biopsies or inaccurate seed placement during template-guided brachytherapy procedures. MRI, on the other hand, provides high-quality images with good tissue contrast, enabling major anatomical structures and tumours within the prostate to be located. However, the equipment needed and amount of time taken for MRI scanning make it unsuitable for routine intra-operative use.

In order to exploit the advantages of each imaging modality, MRI-TRUS fusion has been proposed, whereby a 3D model of the prostate is created from both the pre-operative MRI and intra-operative TRUS, which are then co-registered. In this way, high-quality image data from the MR imaging can be registered onto the TRUS image of a patient's prostate to provide real-time guidance, thereby improving the accuracy of biopsies and other medical interventions.

Image segmentation and registration are necessary for creating a computer-assisted MRI-TRUS fusion system. Existing approaches for MRI-TRUS fusion typically employ manual segmentation and/or rigid

registration. Manual segmentation is time consuming, and rigid registration typically fails to compensate for deformations of the prostate that may occur between the times the MR images are acquired and the TRUS fusion occurs. This potentially leads to uncertainties in registration.

The aim of this research is to provide the necessary techniques for performing reliable MRI-TRUS fusion suitable for use in applications of image-guided prostate interventions. To achieve this goal, the current study has contributed to developing an active appearance model (AAM) for automatic segmentation of MR images to a high level of accuracy, that is computationally faster than comparable approaches. For MRI-TRUS fusion, a new surface-based registration method (the GLTSD-FEM algorithm) has been developed that is robust to local and global deformations of the prostate. Experimental results, based on clinical data, indicate that each of the methods developed has the potential to increase the accuracy of MRI-TRUS fusion. This would, in turn, improve the clinical efficacy of image-based guidance for prostate biopsy and other medical interventions.

Declaration

This thesis contains no material which has been accepted for the award of any other degree or diploma at any university or equivalent institution and that, to the best of my knowledge and belief, this thesis contains no material previously published or written by another person, except where due reference is made in the text of the thesis.

Publications During Candidature

- M. A. J. Ghasab, A. P. Paplinski, J. M. Betts, and A. Haworth, “Robust MRI-TRUS fusion for image-guided prostate interventions,” in *International Conference on Medical Image Computing and Computer-Assisted Intervention (MICCAI)*, 2019, submitted
- M. A. J. Ghasab, A. P. Paplinski, J. M. Betts, H. M. Reynolds, and A. Haworth, “Automatic 3D modelling for prostate cancer brachytherapy,” in *IEEE International Conference on Image Processing (ICIP)*, 2017, pp. 4452–4456.
- M. A. J. Ghasab, A. P. Paplinski, J. M. Betts, H. M. Reynolds, and A. Haworth, “Towards augmented reality: Intraoperative prostate modelling for biopsy and brachytherapy,” 26th Annual Scientific Meeting of the Australasian Brachytherapy Group, 23–25 Feb. 2017, Melbourne, Australia.

Acknowledgements

First and foremost, I would like to express my sincere gratitude to both my supervisors, Professor Andrew Paplinski and Dr John Betts, for their continuous support during my PhD study, and for their patient guidance, motivation and immense knowledge.

I would like to thank my external supervisors. Professor Annette Haworth and Dr Hayley Reynolds, for helping me obtain the necessary background knowledge for this medical domain. I also wish to acknowledge the help provided by our medical partners, Dr Ryan Smith and Professor Jeremy Millar, at the Alfred Hospital for obtaining and preparing the medical images used in this research.

I would like to express my gratitude to Professor Aron Fenster for enabling me to pursue a part of my research in his laboratory at the Robarts Research Institute. I am grateful to the members of his lab, David Tessier, Lori Gradi, Igor Gyackov and Derek Gillies, for their assistance in obtaining and analysing a large set of medical images.

I also want to thank Julie Holden for her language support during my annual milestone reports preparation. Professional accredited editor Mary-Jo O'Rourke AE provided copyediting and proofreading services according to the university-endorsed 'Guidelines for editing research theses' (2019).

I wish to thank various people for their support over the course of my PhD program, specially my fellow officemates for the stimulating discussions in the sleepless nights when we worked together to meet deadlines. In particular, I

thank Amar and Chaluka for all the fun we have had over the last four years.

My special thanks are extended to Hooman, Keyvan, Poorya, Ali, and Zohreh. You feel more like family than friends to me. Words fail me in expressing my appreciation to my parents for their dedication, love, endless support and prayers. To my sister, thank you for being a supportive and caring sibling.

Contents

Abstract	ii
Declaration	iv
Publications	v
Acknowledgements	vi
1 Introduction	1
1.1 Motivation	1
1.2 Problem Background	2
1.3 Research Objectives	3
1.4 Research Scope	4
1.5 Contributions of the Research	5
1.6 Significance of the Research	6
1.7 Thesis Outline	7
2 Prostate Cancer Diagnosis, Imaging and Treatment	9
2.1 Anatomy of the Prostate Gland	10
2.2 Prostate Cancer Diagnosis Methods	10
2.3 Treatment of Prostate Cancer	11
2.4 Prostate Imaging Techniques	11
2.4.1 Transrectal Ultrasound	12
2.4.2 Magnetic Resonance Imaging	13
2.5 Current Use of TRUS in Image-Guided Prostate Procedures	14
2.6 MRI-TRUS Fusion	15

2.7	Implications for the Current Research	18
3	Literature Review: Prostate Segmentation	19
3.1	Region-Based Models	20
3.1.1	Region-Based Level Sets	20
3.1.2	Atlas-Based Models	21
3.2	Supervised/Unsupervised Learning Models	23
3.3	Shape-Based Models	25
3.3.1	Edge-Based Models	25
3.3.2	Deformable Models	26
3.3.2.1	Level Sets	27
3.3.2.2	Active Contour Model	28
3.3.2.3	Active Shape Model	29
3.4	Summary	30
3.5	Research Directions	31
4	Elliptical Filter-Based Segmentation	33
4.1	Initialisation of Ellipses	34
4.2	Toroidal Elliptical Filter	35
4.3	Prostate Localisation Procedure	37
4.4	Algorithm Setup	39
4.5	Experimental Results	41
4.6	Summary	42
5	Active Shape Model Segmentation	44
5.1	Creating an ASM of the Prostate Gland	45
5.1.1	Landmark Annotation of Training Images	45
5.1.2	Alignment of Training Shapes	47

5.1.3	Statistical Model of the Prostate Shape	50
5.2	Fitting the ASM to a New Prostate Image	53
5.2.1	Search Procedure	54
5.2.2	Building a Greyscale Model	54
5.2.3	Objective Function	55
5.3	ASM Setup and Results	57
5.4	Summary of Prostate Segmentation Using ASM	59
6	Active Appearance Model Segmentation	61
6.1	Active Appearance Model of the Prostate	62
6.1.1	Shape Model	62
6.1.2	Texture Model	62
6.2	3D AAM of the Prostate	66
6.3	Fitting the AAM to a New Prostate Image	67
6.4	Results and Discussion	70
6.5	Summary of Prostate Segmentation Using AAM	74
6.6	Constructing the Prostate Surface Model	76
7	Literature Review: Medical Image Registration	78
7.1	Rigid Registration	79
7.2	Deformable Registration	80
7.2.1	Coherent Point Drift	81
7.2.2	Robust Point Matching	87
7.3	Registration Methods for MRI-TRUS Fusion	92
7.3.1	Rigid Registration	92
7.3.2	Deformable Registration	94
7.4	MRI-TRUS Fusion Challenges and Implications for Current Research	100

8	MRI-TRUS Fusion	103
8.1	Proposed Fusion Method	103
8.1.1	Correspondence Estimation	105
8.1.1.1	Global Topological Structure	105
8.1.1.2	Local Topological Structure	106
8.1.1.3	Combined GTS and LTS Differences	107
8.1.2	Transformation Estimation	109
8.1.3	Optimisation Strategy	112
8.1.4	Proposed GLTSD-FEM Algorithm	114
8.2	Experimental Results	115
8.2.1	Data	116
8.2.2	Parameter Settings of GLTSD-FEM Algorithm	117
8.2.3	Evaluation of GLTSD-FEM Algorithm	118
8.2.3.1	Qualitative Registration Results	119
8.2.3.2	Quantitative Registration Results	120
8.2.3.3	Validation of Proposed MRI-TRUS Fusion Method	121
8.3	Analysis and Discussion	123
8.4	Summary	128
9	Conclusions and Future Directions	130
9.1	Contributions of the Thesis	131
9.2	Future Work	133
	References	135

List of Figures

1.1	Proposed workflow for MRI-TRUS fusion	4
2.1	Prostate anatomy	10
2.2	An example of a TRUS image of the prostate gland	12
2.3	Prostate visualisation in TRUS based on different sections of view	13
2.4	Prostate visualisation in MRI based on different sections of view	14
2.5	Proposed surgical biopsy workflow using MRI-TRUS fusion . . .	16
2.6	An example of inter-patient variation in the central region of the prostate	17
2.7	Endorectal coil deforming the prostate	17
3.1	Workflow of atlas-based prostate segmentation	22
4.1	1D Petrou–Kittler half-edge filter	36
4.2	2D toroidal elliptical filtering based on Petrou–Kittler filter . . .	37
4.3	Color-based and surface-based view of the elliptical filter	38
4.4	Prostate segmentation results using elliptical filtering	41
4.5	Example of poor segmentation from elliptical filtering	42
4.6	Examples of well-performed segmentation using elliptical filtering	43
5.1	Manual landmark annotation of the prostate boundary.	46
5.2	Automatic landmark annotation of prostate boundary	47
5.3	Aligning two variations of the one prostate shape	50
5.4	Generating prostate shapes based on three modes of variation .	53

5.5	Search strategy for targeting the prostate edges.	55
5.6	The search space for finding the prostate potential edges.	56
5.7	Prostate shape segmentation using the proposed ASM method	58
5.8	Flowchart of ASM training phase.	59
5.9	Flowchart for fitting the ASM to new slices of MR image.	60
6.1	Prostate appearance warping using a piecewise affine function.	63
6.2	Prostate shape triangulation for piecewise affine warping	65
6.3	3D AAM of the prostate along with its modes of variation.	66
6.4	Prostate qualitative segmentation results by the proposed AAM	73
6.5	A flowchart for constructing a 3D AAM of the prostate image	74
6.6	Diagram of fitting the 3D AAM to a new prostate image.	75
6.7	3D surface model of the prostate.	77
7.1	2D point mapping from X to Y using function T	82
7.2	Schematic diagram of a registration framework using TPS method	95
7.3	Workflow for landmark-based non-rigid registration	96
7.4	Overview of MRI-TRUS fusion using the model-to-image method	98
7.5	Overview of the MR-TRUS fusion workflow by SSM-FEM method	100
8.1	The proposed MRI-TRUS fusion workflow.	104
8.2	Measuring GTS for the current point $\mathbf{x}_i \in X$	106
8.3	Measuring LTS for the current segment $L_k(\mathbf{x}_i)$	107
8.4	Qualitative comparison of surface matching given by five methods	119
8.5	Quantitative comparison of MR-TRUS fusion results	120
8.6	Comparison of TRE for all registration methods	122
8.7	Qualitative TRE given by the GLTSD-FEM method for DAPs	124
8.8	Analysing the model parameters on the registration performance	125
8.9	Average computation times of all registration methods on 38 cases	127

List of Tables

6.1	Segmentation accuracy of ASM and AAM during training . . .	71
6.2	Comparison of ASM and AAM for segmentation of unsighted images	72
8.1	Comparison of 5 registration algorithms based on MSE, HD, and DSC metrics	120
8.2	TRE comparison of all methods based on using 14 DAPs	122
8.3	Time taken by elements of the GLTSD-FEM algorithm for MRI-TRUS fusion	128

Chapter 1

Introduction

Prostate cancer (PCa) is one of the most commonly diagnosed cancers amongst males in many developed countries. Recent statistics given by the Australian Institute of Health and Welfare (2019) show that for males, PCa is expected to be the most common cancer diagnosed in 2020 with an estimated 25,300 cases [109]. The detection of clinically significant tumours in the prostate gland is therefore critical for treatment planning. Conventional procedures to diagnose prostate cancer are the prostate-specific antigen (PSA) blood test, digital rectal exam (DRE) and biopsy. The main treatment options for localised prostate cancer are surgery and radiation therapy. For cancer diagnosis and treatment, imaging plays an important role in obtaining detailed information about the location and size of suspicious tumours.

1.1 Motivation

Magnetic resonance imaging (MRI) and transrectal ultrasound (TRUS) are two of the main imaging modalities used in prostate cancer diagnosis and treatment. TRUS enables a surgeon to spatially identify regions of the prostate

(called zones) and surrounding anatomy such as the urethra. It is used for biopsy and radioactive source implantation for brachytherapy procedures. The benefits of TRUS are that images are created in real time, it is simple to set up and use, and it has a relatively low cost. The major disadvantage of TRUS is that images are of low quality, meaning that small structures are difficult to discern. As a result, biopsy specimens are generally acquired using a standard template rather than a patient specific plan targeted at specific high risk regions, potentially leading to a high false negative rate in cancer detection [133, 38]. MRI is mainly used for prostate cancer staging and treatment planning due to its high-quality images and ability to discriminate between soft tissues. The high quality of MRI images enables more accurate lesion recognition and assessment of the stage of the cancer [11]. However, MRI is not suitable for routine intra-operative use since it requires the patient to be placed in an MRI scanner, and the scanning process is expensive and relatively lengthy.

1.2 Problem Background

Recent advances in technologies such as augmented reality (AR) have given rise to the idea of integrating medical images of anatomy, based on a computerised multi-modal image fusion, for use during clinical procedures [160, 140, 27]. Motivated by this, the current research is directed towards achieving an AR system to intra-operatively locate anatomical structures with a high degree of reliability for biopsies, or for image-guided interventions for PCa such as brachytherapy [28, 10, 99]. One approach is MRI-TRUS fusion, whereby the pre-operative MR images are non-rigidly transformed with intra-operative TRUS images using image segmentation and registration. Segmentation,

the delineation of the prostate boundary, from MRI and TRUS images is performed, from which two 3D models are created. Registration is then used to superimpose these 3D models. If this can be performed successfully, the location of suspicious lesions identified from the MRI data could be superimposed on to the real-time TRUS images during the clinical procedure.

Segmentation and registration of prostate images are non-trivial tasks. One of the main difficulties is the current need for manual segmentation of the prostate boundary from both MRIs and TRUS images. This manual process is slow and requires highly skilled medical staff. Furthermore, the prostate gland is a soft organ and its shape may be deformed by certain conditions such as a full bladder, rectal wall motion, US probe, or surgical intervention. Because the MRI scans are made prior to the procedure and TRUS images during the procedure, there is a possibility that the prostate shape may change in the interval between MRI and TRUS imaging. These deformations need to be addressed when registering the MRI and TRUS images to achieve clinically acceptable fusion accuracy.

1.3 Research Objectives

The goal of this study is to develop techniques that achieve reliable MRI-TRUS fusion accuracy for use in image-guided PCa procedures. The specific objectives of this study are:

- to propose an automatic method for segmentation of the prostate,
- to create a 3D surface model of the prostate from the segmented images,
- to develop a registration algorithm for MRI-TRUS fusion, that is robust to deformations of the prostate present in the image sets of each modality.

Figure 1.1 shows a possible workflow to achieve this.

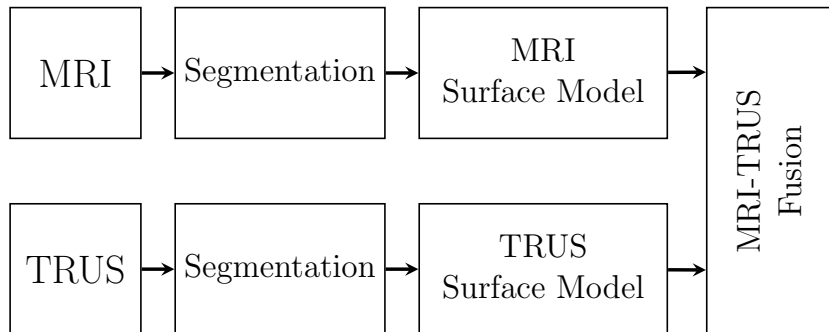


Figure 1.1: Proposed workflow for MRI-TRUS fusion

1.4 Research Scope

Three approaches were investigated for automatic segmentation of the prostate. These included edge-based filtering, active shape modelling (ASM), and active appearance modelling (AAM) techniques. All three methods achieved reasonably accurate results for segmenting the prostate from MRI. The AAM approach was used to segment the prostate from the TRUS images. The accuracy of the results was low due to insufficient data for training the model. Segmentation of the prostate from ultrasound images was not investigated further using this method because new technologies such as convolutional neural networks (CNNs) are emerging and demonstrating more accurate results than the AAM approach. These advanced methods are beyond the scope of the current research.

For non-rigid MRI-TRUS registration, the 3D prostate surface model was created using each modality, and manually segmented images to provide ground truth data. This was done to validate the co-registration surface without propagating potential errors resulting from automatic segmentation.

1.5 Contributions of the Research

The following contributions have been made in the course of this thesis:

- A statistical deformable model, based on an active appearance model (AAM), was developed to automate prostate segmentation from MR images to a high degree of accuracy. This new AAM method uses a fast optimisation strategy for estimating the shape and the texture parameters of the AAM and therefore has a low computation time. This work was presented at the IEEE International Conference on Image Processing (ICIP 2017) [54].
- A fully automatic active shape model (ASM) of the prostate was created, on which the AAM method is based. The ASM method can automatically annotate a set of landmark points based on rotation at equi-angular increment around the prostate boundary to produce an accurate contour. The preliminary results of this method was presented at the Annual Scientific Meeting of the Australasian Brachytherapy Group (ABG 2017) [6].
- To automatically locate the prostate, an elliptical filtering model was developed and fitted to each axial MR image slice to approximate the initial shape of the prostate with an ellipse under a fast searching strategy. Using this information, the deformable model created by either ASM or AAM methods can propagate close to the region where the prostate gland is located. As a result, a priori knowledge obtained by the elliptical filtering approach contributes to improving the accuracy of the segmentation as well as computation speed.
- A new surface-based registration algorithm (GLTSD-FEM) was

developed for performing MRI-TRUS fusion. The GLTSD-FEM algorithm uses the global-local topological structures of the prostate gland to establish an accurate correspondence between MRI-TRUS surface points. It uses a single form optimisation framework to simultaneously estimate the correspondence and the transformation components within a few seconds, for fusing the 3D models. This work has been submitted to the MICCAI 2019 conference¹.

- The GLTSD-FEM algorithm was validated by measuring the targeted registration error (TRE) between pairs of distinct anatomical points (DAPs) within the prostate gland from both MRI and TRUS images, from real brachytherapy patient data. The results obtained show that the proposed method is robust in registering the two models with a low degree of error.

1.6 Significance of the Research

This research could potentially have clinical applications for prostate cancer diagnosis and treatment. This research envisages a scenario where the prostate structure data is extracted (segmentation phase) from pre-operative MR images of a patient, with locations of suspicious lesions within the gland marked by a physician or an automated segmentation method [145]. A 3D model created from the segmented MRI is registered (fusion phase) with the TRUS surface model during the surgical procedure. Multimodal image fusion in this fashion can provide an augmented location estimation for a surgeon to perform accurate needle positioning during prostate biopsy procedures while using TRUS imaging for guidance, and pinpoint the position of suspicious

¹<http://www.miccai2019.org/>

lesions from high-quality MR images. This same approach can also improve the accuracy of prostate cancer treatments such as seed implantation for focal brachytherapy [14].

1.7 Thesis Outline

This thesis is structured as follows:

- Chapter 2, introduces prostate anatomy, cancer diagnosis and treatment methods. This is followed by a review of current imaging technologies used in prostate cancer procedures.
- Chapter 3 provides a literature review of techniques and methods used to analyse and segment the prostate gland from medical images.
- In Chapter 4, an elliptical filter model is proposed to approximate the initial shape of the prostate with an ellipse for computationally fast segmentation of the region of interest (ROI) in each image slice where the prostate is located.
- Segmentation is improved in Chapter 5 by developing an active shape model (ASM), where the prostate shape is estimated by fitting a statistical deformable shape model to 2D image slices.
- The ASM is extended to the active appearance model (AAM) in Chapter 6 to incorporate a statistical model of the prostate texture information for more accurate segmentation.
- Chapter 7 reviews image registration techniques and their applications relating to MRI-TRUS fusion.

- In Chapter 8, a new surface-based registration algorithm is developed for robust fusion of prostate 3D models constructed from MRI and TRUS images. Using the proposed GLTSD-FEM algorithm, to establish a correspondence between the 3D points in TRUS and MRI surface models, a distance-based metric is used to measure both global and local similarities between topological structures of the two point sets. A biomechanical model of the prostate created by a finite element model is then incorporated into an objective function for robust transformation of the corresponding points from MRI into TRUS space. The GLTSD-FEM method is validated using a set of distinct anatomical points (DAPs) obtained from clinical images of patients.
- Chapter 9 summarises the research and outlines potential future research directions.

Chapter 2

Prostate Cancer Diagnosis, Imaging and Treatment

Overview

This chapter provides a general overview of prostate cancer diagnosis, treatment procedures, and the types of imaging methods used in cancer detection and treatment. The anatomy of the prostate gland is described in Section 2.1. Methods for prostate cancer diagnosis are given in Section 2.2. A brief description of treatment planning is given in Section 2.3. Section 2.4 introduces two imaging modalities commonly used for prostate cancer diagnosis and treatment: TRUS and MRI, which underpin the techniques and modelling developed in this thesis. A clinical workflow of an image-guided prostate procedure is described in Section 2.5. Current proprietary tools for performing MRI-TRUS fusion for prostate biopsy are described in Section 2.6. Finally, implications for the current study are outlined in Section 2.7.

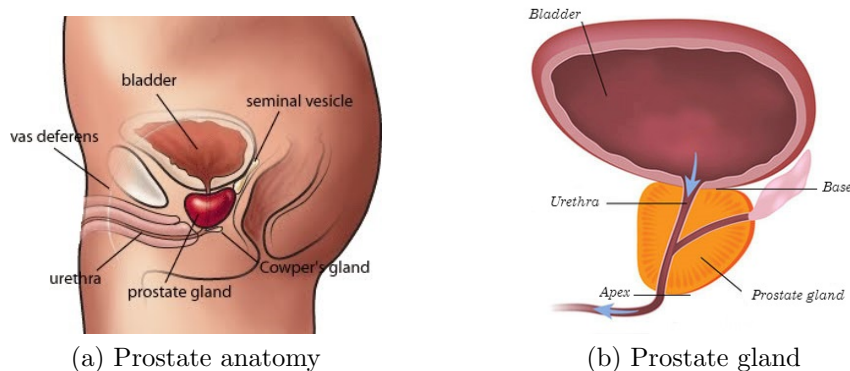


Figure 2.1: Prostate anatomy¹

2.1 Anatomy of the Prostate Gland

The prostate gland is a walnut-sized organ forming part of the male genitourinary system. It is located adjacent to the bladder and rectum, and has the urethra passing through its centre, as shown in Figure 2.1a. By convention, the base of the prostate is adjacent to the bladder and its apex is located at the inferior part of the gland, as shown in Figure 2.1b. The weight of a typical healthy prostate gland is approximately 20 to 25 grams with dimensions of approximately $4 \times 2 \times 3$ centimetres. Size varies between men, increasing with age and disease status.

2.2 Prostate Cancer Diagnosis Methods

Conventional procedures to diagnose prostate cancer are digital rectal exam (DRE) and the prostate-specific antigen (PSA) blood test.

- The DRE is performed by a physician to detect any irregularities in the shape or size of the prostate gland by palpation of the prostate through the wall of the rectum.

¹ Source: <http://www.optimalhealthnetwork.com/Prostate-Health-s/336.htm>

- PSA is a protein produced by the prostate gland. If the amount of PSA in the blood is higher than normal (around 4.0 ng/ml), it may be a symptom of prostate enlargement due to benign conditions, or cancer [20].

If there are suspicious abnormalities detected on a DRE or PSA test, patients are typically advised to undergo a prostate biopsy to determine whether there are malignant or benign lesions in the prostate tissue. Biopsy is performed by either transrectal ultrasound or transperineal template-guided procedures [88, 43].

2.3 Treatment of Prostate Cancer

There are several treatment options for PCa, based on the stage of the cancer, the patient's age and clinical preference status. These include:

- radical prostatectomy: the surgical removal of the prostate gland along with surrounding tissue
- external beam therapy: a radiation therapy, in which high-energy X-ray beams generated outside the patient's body are focused on the prostate
- brachytherapy: the permanent or temporary implantation of radioactive seeds into the prostate to sterilise the cancer cells using either Low Dose Rate (LDR) or High Dose Rate (HDR) approaches

2.4 Prostate Imaging Techniques

Imaging is used for both cancer diagnosis and treatment. For diagnostic procedures such as prostate biopsy, MRI with "cognitive fusion" is typically

used to qualitatively identify suspicious regions and the extent of disease for example, in seminal vesicles or extra-capsular extension. Biopsy information, along with a diagnostic MRI, DRE, and PSA blood test is used to determine the stage (that is, the likelihood of progress to a metastatic state) of the disease and recommended treatment. TRUS and MRI are two commonly used imaging modalities. These are described in the following sections.

2.4.1 Transrectal Ultrasound

TRUS imaging is commonly used to locate regions within the prostate gland during surgical interventions. Images are created in real-time enabling it to be used intra-operatively. It is cost-efficient, portable, and as a consequence, TRUS units are widely available. To produce images using TRUS, an ultrasonic transducer (probe), with diameter of approximately 2 cm, is inserted into a patient's rectum. Low-spectrum audio sound waves are emitted and reflected, from which an image is reconstructed showing regions of different density and hence anatomical structures. An example of a TRUS image is shown in Figure 2.2, in which the surface of the prostate reflects sound waves with a low echogenicity (darker area). There are two types of ultrasound

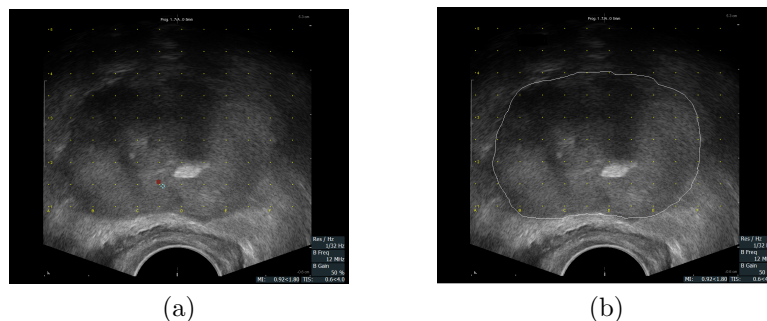


Figure 2.2: The prostate is shown by a solid dark mass in (a). To give a better insight, the prostate boundary is outlined in (b). (Image source: Peter MacCallum Cancer Centre)

probes, side-fire and end-fire, which are used for different sectional views of the prostate. The side-fire probe provides a sagittal plane view, while the end-fire transducer gives an axial (transverse) plane view of the prostate. Examples of TRUS images showing both axial and sagittal sections are given in Figure 2.3.

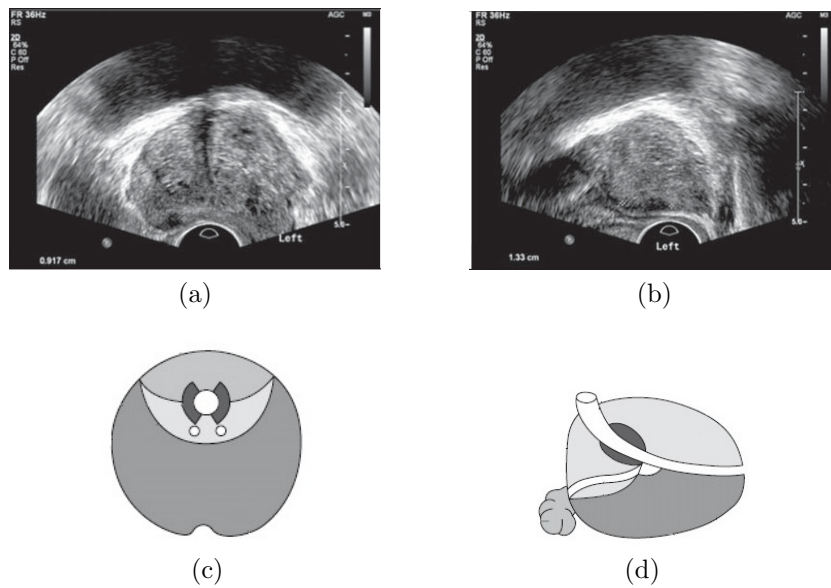


Figure 2.3: Ultrasound images of a prostate based on different sections of view. (a) and (c) axial view, (b) and (d) sagittal view.

2.4.2 Magnetic Resonance Imaging

MRI is used to create high-quality images of body structures along with their detailed characteristics. To provide MR images, impulsive radio wave energies and strong magnetic fields are delivered to the area of the body being studied (pelvic region). Radio wave pulses excite nuclear spin (an intrinsic form of angular momentum carried by elementary particles) energy transition, and magnetic field gradients localise the radio-frequency signal in space. By forming the signal into an image format, different contrasts between tissues are generated based on varying the parameters of the pulse sequence. For the

purpose of this project, MRI images were acquired as a stack of 2D slices that describe the prostate gland along with surrounding tissue. These individual slices can be reconstructed in the three orientations of axial (transverse), sagittal and coronal, as shown in Figure 2.4.

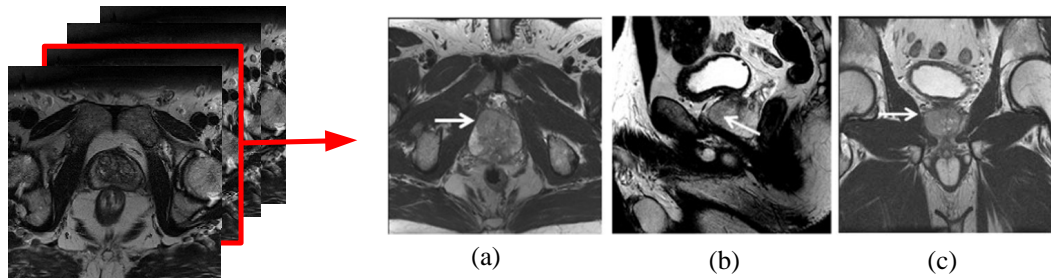


Figure 2.4: An example of MRI taken from the prostate gland (a) axial; (b) sagittal; (c) coronal. (Image source: MICCAI²)

Multiparametric MRI (mpMRI) of the prostate is an imaging technique that combines several types of MRI scan, namely: diffusion-weighted imaging (DWI) and dynamic contrast-enhanced (DCE) to provide parametric and pharmacokinetic data that can be used in cancer staging. This enables clinicians to more accurately define regions of clinically significant disease [15, 2].

2.5 Current Use of TRUS in Image-Guided Prostate Procedures

This section briefly describes the ways in which TRUS imaging is currently used for guidance during procedures such as prostate biopsy and brachytherapy.

During transrectal or transperineal biopsies, TRUS imaging is used intra-operatively to guide the biopsy needles. In the case of transrectal biopsies, a surgeon typically works from a diagram of the regions to be sampled.

²<http://promise12.grand-challenge.org/>

For transperineal biopsies, a template with a grid with regular hole spacing is used to improve accuracy of needle placement. In both these methods, there is the possibility of failing to sample small volume, high grade tumours. This potentially reduces the accuracy of biopsy, which could lead to either an overdiagnosis of low-risk prostate cancer or underdiagnosis of high-risk cases [134, 26].

For LDR brachytherapy, TRUS is used to acquire images of the prostate for planning and implantation of the radioactive seeds. High dose rate (HDR) brachytherapy uses a single radioactive source that steps through multiple catheters (or needles) that have been implanted into the prostate. Once the source has finished delivering the radiation dose, the catheters (and source) are removed. As for LDR brachytherapy, TRUS is used for guidance (of the catheter placement) as well as for producing the images used for planning. However, when delivering either of these treatments, using TRUS images alone may not provide a sufficiently accurate guidance to identify regions of the prostate that contain clinically significant tumours to receive an intensified radiation dose.

2.6 MRI-TRUS Fusion

Researchers have been investigating how to locate clinically significant tumour foci using pre-operative MR images and incorporating this information into real-time TRUS images obtained during the procedure, in order to improve the accuracy of prostate surgical interventions [15, 2, 4]. One approach is MRI-TRUS fusion, whereby data from both imaging modalities is combined into a single model to provide detailed information about the location of suspicious lesions inside the prostate gland. The MRI-TRUS fusion task is

underpinned by image segmentation and registration. Segmentation is required to find the outline of the prostate shape in both MRI and TRUS images in order to create a 3D model of the prostate under each imaging modality. Registration is then used to overlay these models so that common regions coincide.

In the case of biopsy, the benefit that could be achieved by this procedure is that the MRI can guide a clinician to defined parts of the prostate that may contain clinically significant tumours. Hence the fused / co-registered images enable targeted biopsies that will: reduce the rate of false negative diagnoses, reduce the rate of re-biopsy, and potentially decrease the number samples taken at biopsy. This would improve the accuracy of staging, hence direct patients to the most appropriate form of treatment, and reduce the risk of infection by reducing biopsy sampling rates. A proposed workflow, showing how prostate biopsy could occur using MRI-TRUS fusion is shown in Figure 2.5.

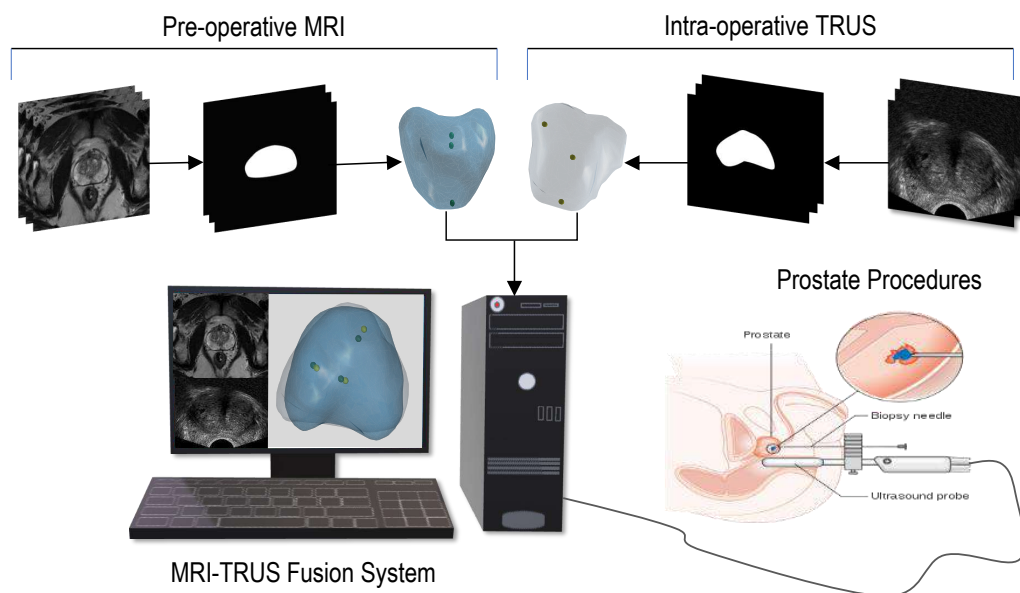


Figure 2.5: Proposed surgical biopsy workflow using MRI-TRUS fusion

There are several existing commercial products available including Artemis, Koelis, Uronav, and BioJet, that are used for performing MRI-TRUS fusion

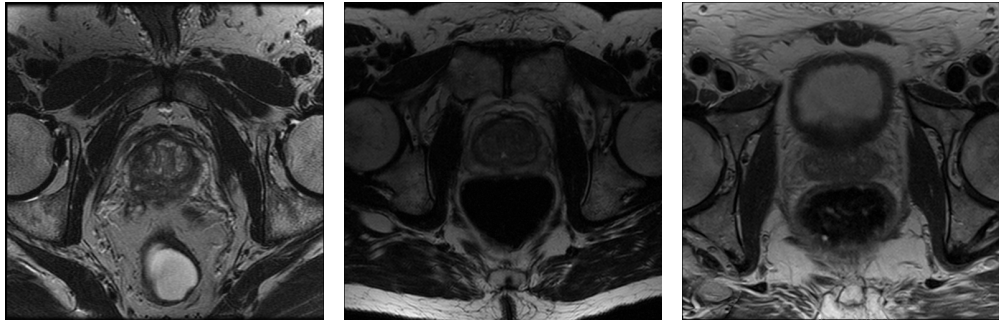
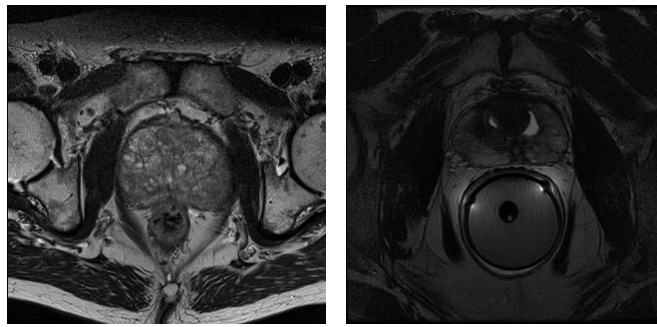


Figure 2.6: An example of inter-patient variation in the central region of the prostate size, shape, and volume. (Image source: MICCAI²)



(a) Without endorectal coil (b) With endorectal coil

Figure 2.7: Prostate shape deformation and contrast variation due to using endorectal coil for MR imaging.

[62, 50, 94]. Even though publicly available information is limited, it appears that some of these devices are limited to manual or semi-automatic methods for segmenting the prostate. This is because outlining the prostate boundary is a difficult task due to considerable inter-patient difference in prostate size, shape and volume, as shown in Figure 2.6. In addition, the use of an endorectal coil for MR imaging causes some intensity variations through the prostate and considerable deformation of the gland. An example of this can be seen in Figure 2.7. Added to this, the US probe in the TRUS imaging itself distorts the prostate shape significantly. Segmentation of the prostate from TRUS is also difficult because the quality of images is low. Contrast in TRUS images may vary between different machine manufacturers. Also, tuning the TRUS

acquisition parameters of the same machine may yield images with different quality. An example of parameter tuning for prostate imaging by TRUS can be seen in Figure 2.2a and Figure 2.3a, in which axial views of the prostate taken from different machine manufacturers are shown.

Some of the current commercial products use rigid registration for transforming the location of suspicious regions from MRIs to TRUS images. Even when non-deformable registration methods are available, validation of the registration accuracy is challenging. This is because the extracted prostate shape from the 3D MRIs maybe very different to the segmented prostate shape from the 2D TRUS images.

2.7 Implications for the Current Research

In order to address the current limitations of existing approaches to 3D fusion of MRI-TRUS images, this research attempts to achieve the following goals:

1. automate the segmentation of MR images,
2. construct a 3D model of the prostate from 2D segmented images for each imaging modality,
3. develop a registration algorithm for robust fusion of MRI and TRUS models.

Achieving these goals will contribute to the development of a multi-modal image fusion platform for use in image-guided prostate interventions such as prostate biopsy and brachytherapy.

Chapter 3

Literature Review: Prostate Segmentation

Overview

This chapter reviews methods for automatic segmentation (that is, delineating the prostate boundary) in TRUS and MR images. Manual prostate segmentation is time-consuming and this makes achieving a real-time MRI-TRUS fusion difficult. Therefore, researchers have been investigating how to automate this process. Automatic detection of the prostate boundary from medical images is non-trivial because large deformations of the prostate make the boundary edges indistinct. In addition, scanning devices that made by different manufacturers produce images with different variations of contrast where this could potentially limit the performance of automatic segmentation methods.

Method used to segment the prostate boundary from medical images are categorised into groups and presented as region-based models in Section 3.1, as supervised and unsupervised learning models in Section 3.2, and as

shape-based models in Section 3.3.

3.1 Region-Based Models

Region-based methods deal with local intensity relationships between pixels/voxels of homogeneous regions for segmentation of the region of interest. These segmentation techniques are further classified into region-based level sets and atlas-based methods.

3.1.1 Region-Based Level Sets

In region-based level-set methods, from manually segmented images, statistical information of the prostate region such as mean and standard deviation are extracted to maximise the margin between the background and the prostate based on region-based statistical moments. This is followed by propagating a pre-defined deformable model implicitly between the two regions for separating the prostate from the background based on minimising the energy of the model [56, 163, 21].

Fan et al. used a region-based level set to segment boundaries of the prostate gland from 3D TRUS images [48]. In their work, a fast discriminative technique was initially developed to identify the prostate region by considering intensity likelihood, in which a cubical window was used for sliding over the 3D TRUS image to measure the difference between maximum and minimum intensity values in the current window. The value of the voxel located at the centre of the current cubical window was set to zero if the difference measurement was less than two. Otherwise, the voxel value was set to one for measurements of greater than two but below a threshold defined by the user. This information was then integrated into a level-set framework for segmenting

the prostate. In recent work, variants of region-based level sets have been combined with statistical models for contouring the prostate boundary from MRIs [121, 150, 179].

3.1.2 Atlas-Based Models

In multi atlas-based (MAS) approaches, a specific model of the organ of interest is created by using a set of manually labelled images of that anatomical structure which are aligned and mapped into a common coordinate system [36, 158, 167, 71]. The obtained model (atlas) acts as a reference in the segmentation algorithm for determining the prostate boundary from images of new patients.

Proposed by Klein et al. [83], a MAS method was applied to 3D MR images of 50 different cases to segment the prostate (including the seminal vesicles). In this approach, each pre-labelled atlas image was matched to the target image by a rough alignment using affine transformation, followed by a flexible (non-rigid) registration using cubic B-splines. Mutual information was used as a similarity measure to evaluate and select a set of best matches. To create a final result, the two methods of majority voting and STAPLE [169], were used to combine the deformed label images into a single segmentation of the target image. This method was followed by an approach, in which the diffeomorphic demons method was utilised to speed up the required time for non-rigid registration [45]. In addition, different metrics such as normalised cross correlation (NCC), normalised mutual information (NMI) and mean reciprocal square difference (MRSD) were used as similarity measures of each atlas image after registration with the target image.

To improve the segmentation accuracy, an approach incorporated combinations of global, regional and local metrics into a multi-atlas framework,

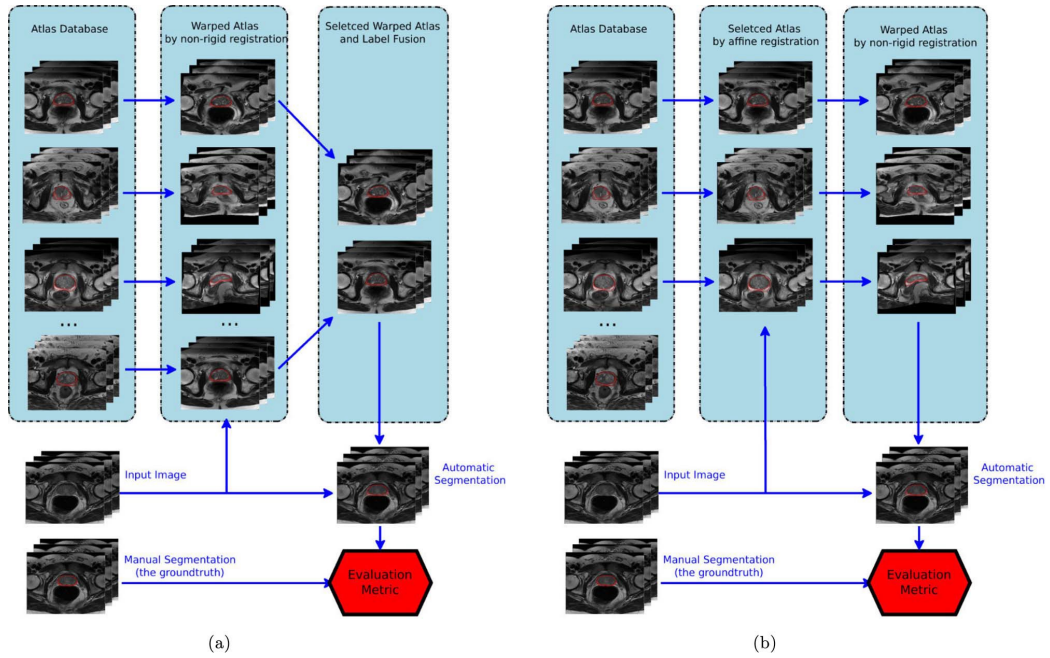


Figure 3.1: “(a) Conventional atlas-based segmentation (b) Proposed atlas-based segmentation”. (Image source: [170])

while decreasing the required number of non-rigid registrations [170]. The proposed workflow, as the authors presented in their publication, is shown in Figure 3.1. To perform the affine registration, a global mean squared error (gMSE) metric was used to roughly align each atlas image to the target. With a modification to conventional atlas-matching methods, a “target-specific regional MSE (rMSE)” was used prior to non-rigid registration in order to select a plausible subset of training atlas. This way, only training atlas images with small values of gMSE were (non-rigidly) registered to the targeted image, where minimisations of the weighted sum of gMSE and rMSE were used as similarity measures. Finally, a weighted voting scheme was performed to combine the aligned labels into a single form based on incorporation of the rMSE and local MSE (lMSE) discrepancy with respect to a proper “total-variation-based spatial regularisation”. Contrary to such conventional voting schemes that assign the same weight to all samples, a patch-based

scheme was introduced [177] to equally weight those samples which have a close similarity according to their local patch-based anatomical feature.

Several studies in this context, for improving the accuracy of prostate extraction from MRIs or TRUS images, investigated different strategies for multi atlas-based segmentation. While some focused on combining a MAB framework with other methods such as graph cuts [84] and edge-detection techniques [149] to refine the segmented prostate in a post-processing step, others proposed innovative methods to prune irrelevant atlases by defining strong a priori knowledge to provide nearly optimal subsets for performing robust atlas registration [108, 7]. Alternatively, to avoid errors accumulated as a result of atlas registration, one approach created a MAB model based on contouring specific slices of the prostate volume and specifying the bounding box of the prostate as a region-of-interest (ROI) based on the key slices [185]. To segment the whole volume, the initial model was propagated to adjacent slices in order to exploit the inter-slice similarity.

3.2 Supervised/Unsupervised Learning Models

Using concepts from pattern recognition, supervised methods create classifiers by means of extracting measurable features from a set of labelled training data in order to classify future unlabelled data. This is in contrast to unsupervised methods, which use feature vectors to assign labels to individual objects as a goal based on an objective function. This way, similarly labelled objects are clustered into the same groups.

One of the earliest unsupervised learning methods for prostate segmentation from TRUS images was proposed by Richard et al. in [125],

in which a classifier was designed to assign individual pixels to their related cluster. A texture-based feature extraction approach was used for determining the mean of each cluster. Pixels were classified according to a probabilistic labelling scheme. The initial segmentation result was then refined by incorporating the compatibility coefficients and pixels spatial information. In recent studies, unsupervised clustering methods were combined with other techniques such as active shape models, Markov random field, etc. for segmenting the prostate boundary, where the clustering part was mainly used to isolate the prostate region in TRUS or MR images as an initial ROI [156, 93, 114, 97].

Utilising a supervised learning method, one approach proposed a random decision forest algorithm to classify the prostate under a probabilistic framework from MR images [55]. The segmentation task comprised two main steps, a representation of the prostate's voxels in a probabilistic search space and propagating a region-based level set in this space to perform a binary segmentation of the prostate. To build the classifier, spatial information of individual pixels, along with the mean and standard deviation of grid-sized neighbouring pixels, were used as features for training the model. The authors of this work improved the prostate segmentation by using a new schema for feature extraction based on a multiple mean statistical shape [57]. A similar work built separate random forest classifiers from multi-channel (T1 and T2) MR images for segmenting the prostate [53]. Alternatively, kernel-based support vector machine (SVM) methods were broadly used by some researchers for prostate segmentation in which the classifier was commonly trained based on a set of features extracted from statistics of the prostate shape, texture information and intensity of pixels [42, 176, 5, 22].

Currently, the latest advances in artificial neural networks (ANNs) have led

to fast-growing deep learning methods, where convolutional neural networks (CNNs), as a family of deep nets, have shown a high capability for improving the accuracy of prostate segmentation. [188, 181, 178, 151, 153]. In contrast with traditional ANNs, which use a set of hand-crafted features to approximate a model, CNNs learn these features directly from the sample images based on a variation of multilayer perceptrons. Conceptually, for prostate segmentation, MRI (or TRUS) images along with the corresponding labels are used as an inputs to a CNN. In lower layers, a set of basic tiny features such as edges and curves are learned from images. These features are propagated into higher layers accordingly. This hierarchical architecture transforms the learned features in the lower levels into semantic anatomical information at the higher levels. To approximate a model for accurate segmentation of the prostate, a back-and-forth propagation of gradient flow and information is used to improve convergence and boundary discrimination rates, respectively.

3.3 Shape-Based Models

Shape-based models are mainly concerned with edge features or boundary information of the prostate for segmentation. These methods can be categorised into three main groups, edge-based, filter-based, and deformable models, where the last one is further subdivided into edge-based level sets, active contour models, and active shape models in turn.

3.3.1 Edge-Based Models

In edge-based methods, a series of mathematical operations are applied on digital images to detect locations of those pixels/voxels (potential edges) indicating a sharp change in their brightness. The popular methods for edge

detection are gradient filters such as Canny, Sobel and Prewitt [137].

Introduced by a work in [1], a multi-resolution framework was designed to detect the prostate boundary edges from TRUS images. To detect the edges by using a proper filter size, the homogeneous regions, identified by small local standard deviation, were filtered out in coarse resolution. To improve the edge localisation, areas with larger local standard deviation were filtered with smaller kernels to preserve the potential prostate edges in these regions. To compensate for missing edges, one approach proposed a semi-automatic method for delineation of the prostate boundary [117]. As reported, to enhance the TRUS images, two type of filter, so-called stick and anisotropic diffusion, were in turn used to remove speckles and smooth the images, respectively. This was then followed by extraction of a set of primitive features from the prostate shape and echo patterns to identify the most likely edges representing the prostate boundary. Finally, broken edges were manually linked together through a manual editing by a user. Alternatively, several studies investigated semi-automatic methods for contouring of the prostate boundary from MR images based on a priori knowledge of the prostate shape [189, 131, 51].

3.3.2 Deformable Models

Deformable model approaches use concepts from physics, geometry, and optimisation techniques for segmenting a deformable shape [100]. Physical theories are used to explain the evolution of the deformable shape in space, geometry is used to constrain the shape model and optimisation is used for fitting the model to new data. Such methods are often concerned with external and internal energies. External energies deform the initial model towards the boundary of the deformable shape, while smoothness of the contour is preserved by internal energies during the deformation. To optimise the process,

both energy forces are united in a single energy-minimisation framework for segmentation of the deformable shape.

Common deformable methods utilised in medical image analysis are edge-based level sets, active contour models and active shape models. These are separately discussed in following sections.

3.3.2.1 Level Sets

Level sets is a conceptual framework for the study of developing curves in higher dimensions [113]. Starting from a seed point, an edge-based level set is perpendicularly propagated towards the curve surface to target the boundary edges. The speed of evolution is inversely proportional to the intensity gradient. Reaching the highest intensity difference in a local neighbourhood leads the evolution process to a stopping criterion.

For segmenting the prostate from TRUS images, one of the earlier research studies, applied a fast discrimination method to initially identify the prostate region [48]. Instead of using the image intensity gradient, the information extracted from this region was incorporated into a level-set model to improve the boundary-leaking problem. The main challenge for full segmentation of the prostate gland using typical level sets was found to be the initialisation of seed points [120], since high-level user interaction was required to initiate the model. One approach used Gaussian and morphological filtering methods in turn to classify the mid-gland TRUS images into two groups, prostate and non-prostate regions [76]. The prostate region was then used by an elliptical level-set model for segmenting the prostate based on first and second moments of a probabilistic Gaussian density function. Further, the authors employed modified local binary patterns to extract texture features from the prostate region for use as an external energy to drive the elliptical level set for improving

the prostate segmentation [75]. Similarly, an elliptical level-set model was developed by one approach for automatic segmentation of the prostate from diffusion-weighted MR images [92]. The prostate shape was initially fitted by a deformable ellipse model and used as the starting point for the level set to evolve. Post-processing techniques were then applied to refine the prostate boundaries.

3.3.2.2 Active Contour Model

The active contour model (ACM) or snake, introduced by Kass et al. [79], is a framework which is used for outlining an object from a possibly noisy image. Initialising the ACM close to an object, it evolves a deformable spline model towards the object's boundary edges where external and internal energies are minimised. Subject to the problem in hand, different external energies may be applied to improve the segmentation by ACM [3, 186, 166].

Using ACM, an energy-based algorithm was used for segmentation of the prostate from TRUS images [183] where a feature map, extracted from the prostate image by a non-linear dot-pattern operator, along with an average geometric model of the prostate shape was utilised to drive the deformable ACM for targeting the prostate contour. To initialise a 3D ACM close to the prostate edges in MRIs, a research study applied a modified gradient vector flow (GVF) to govern the ACM external force [141]. The GVF, presented in [171], was derived from MR images based on minimisation of a certain energy function in a variational framework. Added to this, a prostate shape constraint in the form of an ellipse model was used as a priori knowledge to improve the boundary detection. On the contrary, an external force, known as vector field convolution (VFC) [89], was used in an active contour-based approach for segmentation of the prostate from MRIs [129]. Based on using a

multilayer perceptron neural network for initiating the seed points, the VFC was in turn used to extract the prostate region.

Alternatively, a hybrid method, presented by authors of the work in [152], segmented the prostate in two steps based on using different approaches. At first, a superpixel-based 3D graph cut was used to capture the prostate surface. As an starting point, the initial result of the first step was incorporated into a 3D ACM to update the segmentation. This was followed by iterating between the 3D graph cut and 3D active contour model to obtain a smooth prostate surface.

3.3.2.3 Active Shape Model

The active shape model (ASM), introduced by Cootes et al. [32], creates a statistical model of an object's shape based on two components: average shape, and its typical variability, which are constructed from a set of training images. The typical variability of the shape is determined by computation of principal component analysis (PCA) of a point distribution model (PDM) [31]. Basically, a PDM is obtained by annotating and collecting a set of points around the boundary of the object of interest on every single training image. Once, the shape model of the object is created and initialised, it is used for segmenting the shape from new unsighted images.

A semi-automatic algorithm based on a 2D active shape model was used for segmentation of the prostate boundary from ultrasound images [65]. Three different techniques for landmark placement on boundaries of the prostate were used to build the point distribution model. Shape alignment was determined using a similarity transformation and projection into the tangent space of the prostate mean shape [33]. To create a compact shape model, PCA was further used to identify and retain the most significant components among all possible

options. An image-searching algorithm then used the created ASM to search along the normal profile of each model point to find the best location where the boundary pixels of the targeted prostate were located. Post-processing was also considered by a user to manually correct the model points that were far from the corresponding prostate boundary point. Cosío [34] used a pixel classification procedure to automatically estimate the prostate region in order to initialise the ASM close to the target. To improve automatic prostate segmentation of TRUS images, a partial ASM was used to estimate missing boundaries of the prostate [175]. This was followed by using a discrete deformable model under a multi-resolution framework in order to minimise an energy function for the prostate segmentation. Likewise, a method was proposed by authors of a study in [157] to automatically initialise an ASM for segmentation of prostate images created by MRI via automated identification of MR spectra that lie within the prostate.

3.4 Summary

This chapter has reviewed the literature on segmentation techniques for contouring the prostate boundary from TRUS and MR images. These techniques use shape and texture information for segmentation. Edge features and pixel intensities are the common characteristics used by many of the shape-based and region-based approaches for segmenting the prostate boundary. Other approaches use combinations of shape and texture features, extracted from a large set of prostate images, to create statistical models by using machine learning algorithms to segment the prostate. Although the reviewed approaches report reasonable accuracy in segmentation of the prostate, it is difficult to compare the quantitative aspects of these methods

due to using different datasets, evaluations metrics, and system setups. To the best of our knowledge, automatic prostate segmentation is still an open question due to the following limitations:

- Manual prostate segmentation is currently the most accurate method. However, its long processing time impedes achieving intra-operative MRI-TRUS fusion.
- The prostate may deform either by body motions or by the US probe. These deformations are mainly not compensated for in segmenting the prostate boundary using the current approaches.
- The segmentation accuracy is often low at the apex and base of the prostate and this is mainly because of the poor tissue contrast and the ambiguity between surrounding anatomical structures.
- The majority of prostate segmentation methods are not fully automated and require some level of intervention.
- Time efficiency is another important factor in performing a fully automated prostate segmentation. For example, edge-based methods are not robust against TRUS images and they often identify false edges, resulting in a chain of broken edges. Linking these edges in a post-processing step requires computationally expensive algorithms to combine such methods with texture and intensity information for an accurate segmentation of the prostate.

3.5 Research Directions

To address the current segmentation challenges, this research will focus on improving a statistical deformable model based on the ASM method. Of all

methods, ASMs, although computationally inefficient, have shown promising results for 2D segmentation of the prostate boundary from MRI and TRUS images. The research will extend the ASM method by:

- automatic annotation of the boundary points from the training images for creating a prostate shape model
- optimal initialisation of the shape model close to the prostate region automatically
- development of an objective function for distinguishing the actual edges from noisy pixels.

Automatic annotation of the boundary points and automatic initialisation of the prostate shape model make the segmentation task more time efficient. Likewise, incorporating an objective function into the search algorithm, as a priori knowledge, enables for robust edge detection. Overall, achieving these could potentially provide an automatic algorithm for accurate segmentation of the prostate boundary.

Although new technologies in the field of deep learning such as CNNs provide a potential path for improving the accuracy of automatic prostate segmentation with a high degree of reliability, they are beyond the scope of the current study.

Chapter 4

Elliptical Filter-Based Segmentation

Overview

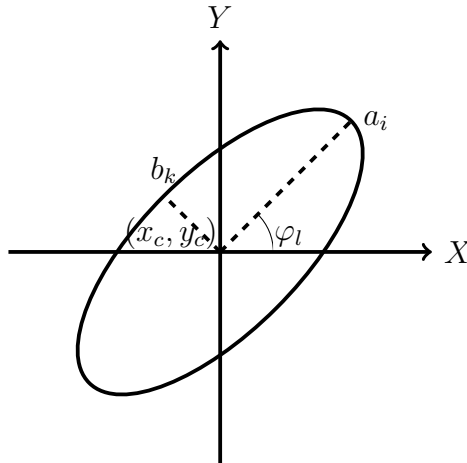
In this chapter, we propose an algorithm for automatic segmentation of the prostate boundary by fitting a pre-designed 2D elliptical filter to slices of the MR image. The proposed method approximates the general shape of the prostate slices by ellipses. To do this, a set of ellipses of different sizes are generated parametrically. Toroidal elliptical filters are then created by rotating a 1D edge filter around the boundary of the generated ellipses. Each filter is then convolved with the 2D image slice to find the location where that elliptical filter gives the best match with the prostate boundary. This is obtained by finding the location that results in the maximum value of the convolution. This value is recorded for each elliptical filter. The highest value against all recorded values is considered best, since it corresponds to an ellipse of certain size that best match to the prostate boundary in the image. This method can be considered a task of parametric modelling such that the target model is

defined as an ellipse and the aim is to estimate and optimise its representative parameters. Such an elliptical filter is robust to blurred edges, a situation that is typical with MRI and TRUS images. This advantage can make the elliptical filter method an excellent candidate for locating the initial boundary of the prostate with a high degree of reliability.

4.1 Initialisation of Ellipses

The general equation for an ellipse in complex coordinates is:

$$Z_T = [a_i \cdot \cos(\theta) + jb_k \cdot \sin(\theta)] \cdot e^{j\varphi_l} \quad ; \quad 0 \leq \theta \leq 2\pi. \quad (4.1)$$



The semi-major and semi-minor lengths of the ellipse are described by parameters a_i and b_k respectively. The parameter φ_l determines the angle between the major axis and horizontal. The semi-major and semi-minor lengths of the ellipse are described by parameters a_i and b_k respectively. The parameter φ_l determines the angle between the major axis and horizontal. To best approximate the prostate shape in each image slice by an ellipse, we generate a set of ellipses of different size and rotation, and then loop over all parameters to obtain their optimal values. To create a search space

for individual parameters of the ellipse, a range of values is defined for each parameter as:

$$\begin{cases} a_i & ; & i = 1, 2, \dots, q \\ b_k & ; & k = 1, 2, \dots, t \\ \varphi_l & ; & l = 1, 2, \dots, s \\ (x_c, y_c) =? & & \end{cases} . \quad (4.2)$$

Hence, the number of generated ellipses Z_T is equal to N , ($T = 1, 2, \dots, N$), where N is equal to $q \times t \times s$. The centre of the ellipse, (x_c, y_c) is further determined through convolution. Each of the generated ellipses is then used for creating a 2D elliptical filter.

4.2 Toroidal Elliptical Filter

A 1D Petrou–Kittler edge filter [118], is used to create the toroidal filter. The Petrou–Kittler filter is chosen because it is fairly robust for optimal detection of ramp edges, which are prevalent in the MR image. The 1D Petrou–Kittler edge filter is represented as follows:

$$s(r) = \begin{cases} 1 + be^{-r} - r_1e^{-ar} \cos(ar + \alpha_1) + r_2e^{ar} \cos(ar + \alpha_2) & 0 \leq r \leq \omega \\ 0 & \text{Otherwise} \end{cases} \quad (4.3)$$

where ω controls the span of half the filter such that a larger amount of it results in filters with wider spans. To select different values for ω , other parameters a, b, r_1, r_2, α_1 and α_2 are also modified according to a given table in [118, 116]. The 1D Petrou-Kittler half-edge filter is shown in Figure 4.1 based on several values of ω .

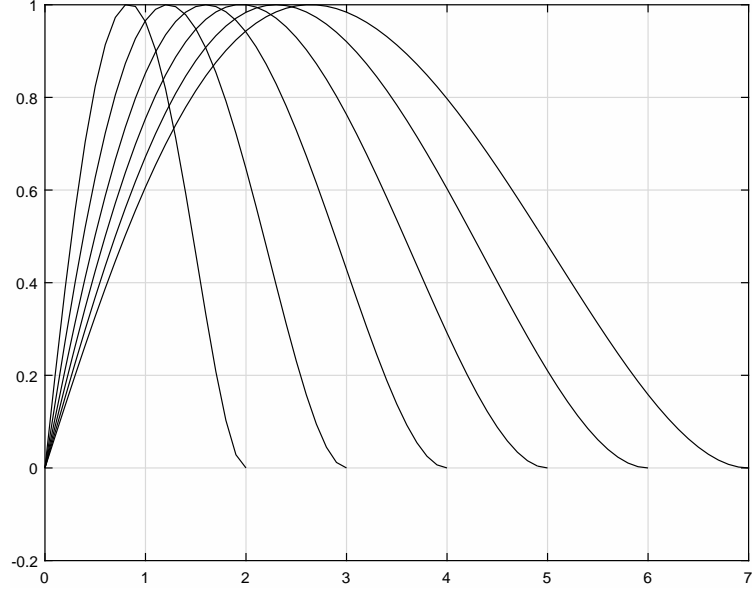


Figure 4.1: 1D Petrou–Kittler half-edge filter with different values of ω .

To create a 2D toroidal filter, the approach in [96] is modified to rotate the 1D Petrou–Kittler edge filter around an ellipse, in order that the centre of the Petrou–Kittler filter is placed at a distance Z from the origin $(0,0)$ in a complex plane and is rotated to form a 2D toroidal filter, as shown in Figure 4.2. Mathematically, the proposed toroidal filter is defined as:

$$H(Z_r) = \begin{cases} s(\| Z_r(\alpha) - Z_c(\alpha) \|) & Z_m \leq Z_r \leq Z_c \\ -s(\| Z_r(\alpha) - Z_c(\alpha) \|) & Z_c \leq Z_r \leq Z_p \\ 0 & \text{Otherwise} \end{cases} \quad (4.4)$$

where Z_r is the complex mode of vector r in eqn (4.3) and α is the angle of the vector Z_r with the horizontal axis of the coordinate. To calculate the weights, $s(\| Z_r(\alpha) - Z_c(\alpha) \|)$, for each half of the Petrou–Kittler filter, the three ellipses Z_m, Z_c, Z_p are defined as constraints to control the vector Z_r within allowable regions of the intended ellipse. These ellipses are described

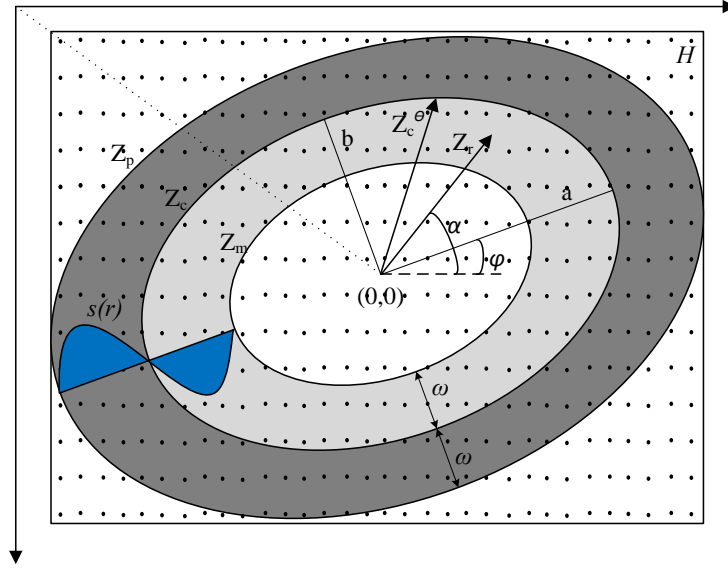


Figure 4.2: The proposed 2D toroidal elliptical filtering shape based on the 1D Petrou–Kittler filter.

based on the parameters a, b and ω as follows:

$$\begin{aligned}
 Z_p(\theta) &= (a + \omega)\cos(\theta) + j(b + \omega)\sin(\theta) \\
 Z_c(\theta) &= (a)\cos(\theta) + j(b)\sin(\theta) \\
 Z_m(\theta) &= (a - \omega)\cos(\theta) + j(b - \omega)\sin(\theta)
 \end{aligned} \tag{4.5}$$

where Z_m, Z_c , and Z_p are complex vectors based on θ , the rotational angle defined from 0 to 2π . After creating the ellipses, they are rotated based on the angle φ using the expression $(Z_m, Z_c, Z_p) \cdot e^{j\varphi}$. The function $H(Z_r)$ outputs a 2D toroidal filter which is represented as $H(j, k)$ with dimensions of $2(a + \omega) + 1 \times 2(a + \omega) + 1$. An example of a 2D toroidal filter is shown in Figure 4.3.

4.3 Prostate Localisation Procedure

Once the proposed filter is created, it is convolved with slices of the given MR image to find the boundary of the prostate. During convolution, the toroidal

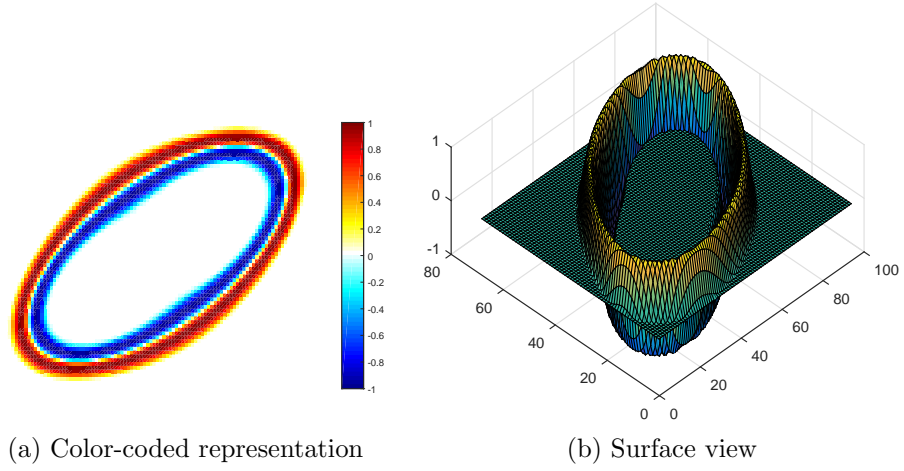


Figure 4.3: Example of elliptical filtering shape derived from 1D Petrou–Kittler edge filter.

filtered is moved over each image pixel and the sum of products of the filter values and the corresponding pixels is calculated. Convolution of the proposed filter $H(j, k)$ with the image $I(x, y)$ is expressed as:

$$\eta = H(j, k) \circ I(x, y) = \sum_{j=1}^n \sum_{k=1}^n H(j, k) I(x - j, y - k) \quad (4.6)$$

where η is a matrix with dimensions equal to the size of the original image I . The maximum value of matrix η is extracted from every convolved filter and recorded in the vector Π_T , where $T = 1, 2, \dots, N$. Elements of vector Π_T correspond to indexes (x_T, y_T) of the related convolution matrix η_T . Hence, the resulting maximum value of the vector Π_T locates the centre of the global best elliptical filter as below:

$$(x_c, y_c) = \arg \max_{x, y, N} \Pi_T. \quad (4.7)$$

Finally, the ellipse located at (x_c, y_c) with optimally estimated parameters a, b , and φ is the best approximation of the given prostate image slice.

4.4 Algorithm Setup

To generate a set of filters, the first step was to define a range of values for each parameter a, b and φ of the ellipse by considering feasible variations of prostates. For instance, observing a considerable number of MR images shows that the angular position of the prostate is almost parallel to the horizontal axis. This means that the angle φ tends to converge to zero in most cases. Hence, defining a small range of values between $[-\pi/12 \ \pi/12]$ was sufficient for this parameter. The other two parameters, semi-major and semi-minor lengths, were initialised with an appropriate range of values accordingly. To make the algorithm efficient, the convolution search space was limited to the region where the prostate is located. This constraint could be obtained based on prior information about the prostate shape and its potential location in MR images. Prior to the convolution process, a Gaussian median filter was used to smooth image slices in order to remove salt-and-pepper noises [59]. The pseudo code of the proposed elliptical algorithm is shown in Algorithm 1.

Data: MR images

- Noise reduction and enhancement of the current image slice $I(x, y)$;
- Initialisation: $\omega, a_i, b_k, \varphi_l$;
- **Step 1:** Generate N elliptical filters $H_T(j, k)$ based on ellipse parameters;

begin

foreach a_i **do**

foreach b_k **do**

foreach φ_l **do**

- Compute three constraints Z_p, Z_c, Z_m ellipses \rightarrow eqn (4.5);
- Create the elliptical filters $H_T(j, k) \rightarrow$ eqn (4.3) and (4.4);

end

end

end

end

- **Step 2:** Convolve the generated $H_T(j, k)$ with the current image $I(x, y)$;

begin

foreach $H_T(j, k)$ **do**

- $\eta = H_T(j, k) \circ I(x, y) \rightarrow$ eqn (4.6);
- Store maximum value of $vec(\eta)$, and current ellipse parameters in matrix Π_T ;

end

- $(x_c, y_c) = \arg \max_{x,y,N} \Pi_T \rightarrow$ eqn (4.7) ;

end

- Segment the prostate by fitting an ellipse using the estimated parameters $(a, b, \varphi, x_c, y_c)$;

Algorithm 1: The proposed elliptical filter-based algorithm.

4.5 Experimental Results

To test the ability of the elliptical filter to locate the prostate, a set of 50 mid-gland MRI images¹ were convolved with the filters generated at varying sizes and orientation. The segmentation result was compared with a manual segmentation provided by a radiologist. Thus, a segmentation with a good performance is one where there is no distinct offset between the boundary of the ground truth and the ellipse. Qualitative evaluations of prostate segmentation with 2D elliptical filters are shown in Figure 4.4.

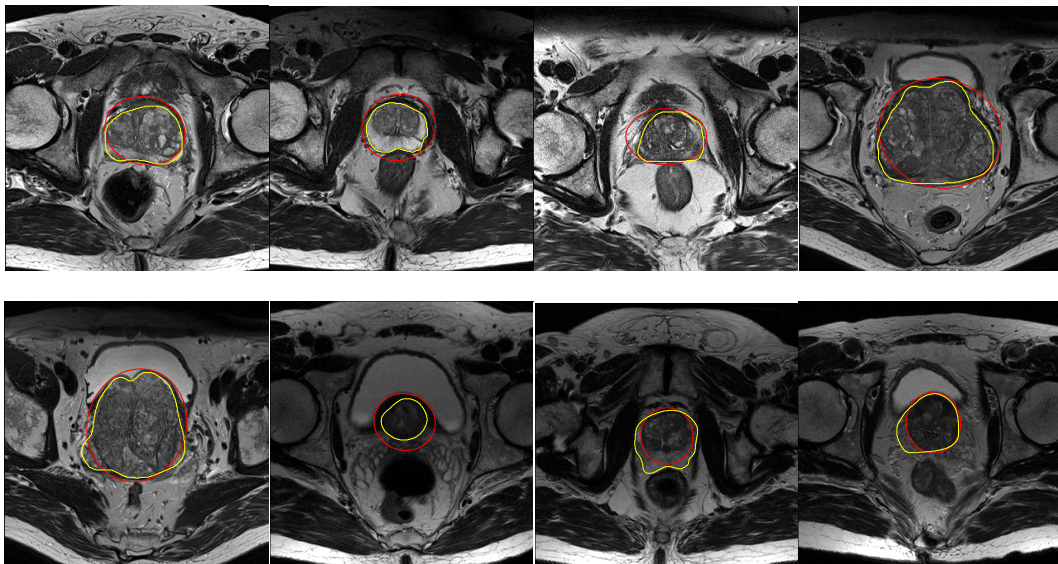


Figure 4.4: Examples of prostate shape segmentations using elliptical filtering. The segmented prostates with the toroidal filter and reference are shown with red and yellow colours respectively.

The proposed filter was able to detect the region where the prostate gland is located in almost all images. It also performed well to localise the prostate at its base in some images. Localising the prostate base is difficult since it is located close to the bladder and this makes it hard to find its border. The second image of the second row, from left to right, in Figure 4.4 shows an

¹<http://promise12.grand-challenge.org/>

example of prostate base segmentation by the method.

Although the elliptical filter found the prostate region in images, it failed to fit the ellipse close to the boundary of the prostate gland in some cases. Figure 4.5 shows some examples of prostate segmentation, where the filter did not perform well. This can be due to conditions such as poor tissue contrast overlapping of the prostate boundary with surrounding organs like the bladder and rectum. For instance, the top and bottom sides of the prostate boundary in the third image, from left to right in Figure 4.5, overlap with the boundaries of the bladder and rectum respectively. Also, an evident example of poor tissue contrast can be observed in the last image of the current figure. The proposed

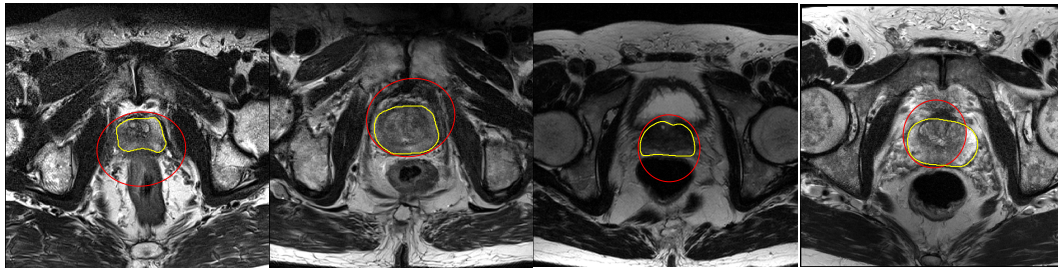


Figure 4.5: Examples of prostate images on which the proposed method algorithm failed to perform well. The segmented prostates with the toroidal filter and reference are shown with red and yellow colours respectively.

algorithm worked surprisingly well for segmentation of some prostate images with a considerable level of difficulty, as shown in Figure 4.6.

To further improve the above method, the ellipses can be replaced with ellipsoids and related 3D filters applied not to slices, but to 3D images. We decided to consider this in future work.

4.6 Summary

This chapter provided an automatic algorithm for the initial segmentation of the prostate boundary. With the assumption that the prostate shape is almost

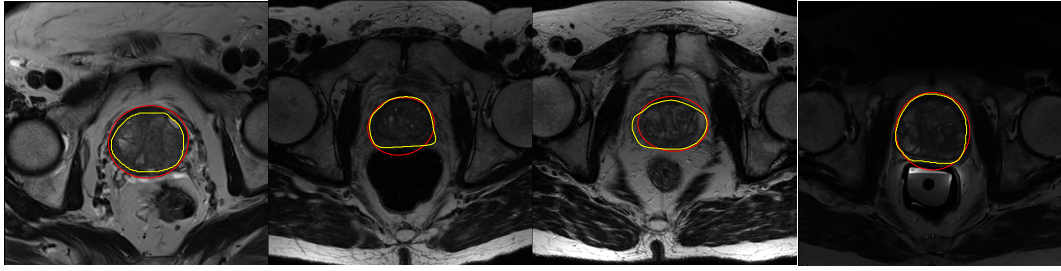


Figure 4.6: Examples of well-performed segmentations using the method on some difficult images. The segmented prostates with the toroidal filter and reference are shown with red and yellow colours respectively.

ellipsoidal, a template-matching strategy was proposed to approximate the prostate with an ellipse by fitting an elliptical-shaped filter to the MRI slices. To do this, a set of 2D elliptical filters were created based on the rotation of a 1D edge filter around the boundary of ellipses of different size. Each filter was convolved with MRI slices and its maximum matching value was recorded accordingly. This process repeated for all filters having different ellipse sizes. Finally, the prostate boundary was best approximated by the elliptical filter that achieved the global maximum among all filters. Implementation of the algorithm and applying the created filter to a set of MRI data demonstrated encouraging results. It is worth noting that there was no need for the toroidal filter to learn from training a dataset to segment the prostate by the toroidal filter. This advantage saved significant computation time.

The elliptical filter method could be used as the initialisation for deformable shape models to improve the accuracy of prostate segmentation, such that the elliptical filter is used to roughly fit an ellipse to the boundary of the prostate and the deformable model is used to refine the initial segmentation. We will consider this approach in future work.

Chapter 5

Active Shape Model

Segmentation

Overview

This chapter describes the construction of an active shape model (ASM) of the prostate gland and its application for segmentation of new prostate shapes from unsighted MR images. An ASM is a statistical representation based on the general form of the prostate (mean shape) and its typical variability as derived from the prostate instances [32]. ASMs are created by training on a set of data. Once created, an ASM can be fitted to a new, unsighted instance of the model, enabling features of the new instance to be located. The steps required to create the ASM of the prostate are described in Section 5.1. This outlines landmark annotation of training images, alignment of training shapes and statistical model of the prostate shape. In Section 5.2, the model is used to segment new examples based on optimising an objective function in an iterative search procedure. The segmentation results of the ASM method are shown in Section 5.3. Finally, Section 5.4 summarises the proposed method

into the two general phases of training and fitting the shape model.

5.1 Creating an ASM of the Prostate Gland

Successive steps are considered to build a model of the prostate shape, such that:

- The boundary of the prostate in each MRI slice is annotated with a set of points. This reduces the input data to vectors of the labelled points, creating shape vectors.
- All vectors are aligned with a reference (initial mean shape) using the general procrustes analysis (GPA) approach.
- Averaging the aligned shape vectors results in the prostate mean shape.
- The principal component analysis (PCA) method is then used to find the significant principal axes from the distributed shape points in order to account for the typical variability of the prostate.

The ASM of the prostate is accordingly constructed based on the obtained prostate mean shape and the PCA results. This model is further used for segmentation of the prostate from unsighted MR images. The following three subsections describe the required steps to create an ASM of the prostate.

5.1.1 Landmark Annotation of Training Images

To describe the prostate outline by a vector, each visible shape of the prostate in training MR images is manually annotated with a set of landmark points. The landmark points are placed on the boundary of the prostate to describe the prostate curvatures, giving its outline accurately. An example of a prostate

annotated with 20 landmark points is shown in Figure 5.1 for a given slice of an MR image. Manual landmark annotation is somewhat difficult and

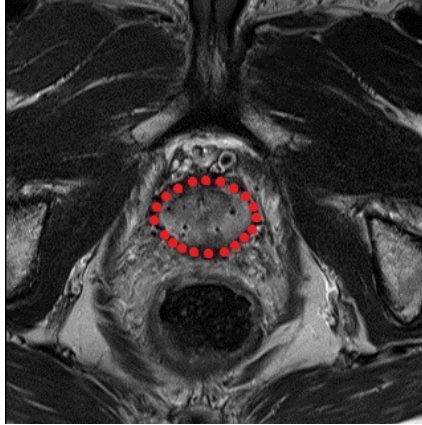


Figure 5.1: Manual landmark annotation of the prostate boundary.

time-consuming, since the quantity and sequence of points should be consistent over all images of the training dataset.

In this study, to automate the process, an algorithm was proposed to select landmark points from the boundary of the prostate, consistent over all training images. The proposed algorithm works based on the assumption that the prostate boundary is a closed line. It then selects a specific number of boundary points by rotating a vector in a polar coordinate originating from the centre of the prostate shape. Since finding the exact location of the prostate boundaries from greyscale images is difficult, the labelled training images are instead used to identify the intersections of the rotating vector with the prostate edges as the boundary points. An example of automatic landmark annotation by our proposed algorithm is shown in Figure 5.2. To preserve consistency over all training images, the rotating vector starts from where its angle with the x axis is zero, and rotates counter clockwise with a fixed amount of degree. Changing the rotation angle can lead to different numbers for selecting the landmark points, such that for selecting n points the rotation angle is defined

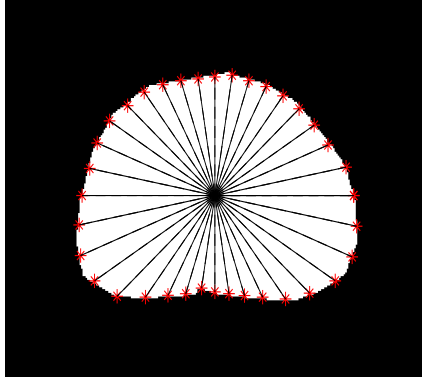


Figure 5.2: Automatic landmark annotation of the prostate boundary from binary images using the proposed algorithm.

as $\frac{2\pi}{n}$.

5.1.2 Alignment of Training Shapes

After storing the annotated points in a vector, the GPA approach is used to align all shape vectors obtained from training data [60]. The alignment is performed by applying a set of linear operations such as translation \mathbf{t} , scaling s and rotation $R(\theta)$ on the shape data. A least squares approach is used to minimise the distance between identical points from individual shapes so that they correspond as closely as possible.

A prostate shape containing n landmark points is described by:

$$\mathbf{x}_k = \begin{bmatrix} x \\ y \end{bmatrix}_{2 \times 1} \quad k = 1, 2, \dots, n \quad (5.1)$$

$$X = [\mathbf{x}_1, \mathbf{x}_2, \dots, \mathbf{x}_n].$$

where all points \mathbf{x}_k are kept in X , representing a 2D shape of the prostate.

The alignment of two given shapes X and Y is performed using the transformation function G as shown below:

$$\mathbf{z}_k = G\hat{\mathbf{x}}_k \quad ; \quad G = \begin{bmatrix} sR(\theta) & \mathbf{t} \end{bmatrix} \quad ; \quad \hat{\mathbf{x}}_k = \begin{bmatrix} \mathbf{x}_k \\ \mathbf{1} \end{bmatrix} \quad (5.2)$$

where $Z = [\mathbf{z}_1, \mathbf{z}_2, \dots, \mathbf{z}_n]$ is the estimation of shape X transformed by parameters obtained from Y . The parameters $s, R(\theta)$ and \mathbf{t} are scaling, rotation and translation, respectively, which constitute the transformation function. The translation \mathbf{t} is defined by a 2×1 vector and $R(\theta)$ is a 2×2 orthogonal matrix. Reformulating the transformation matrix G results in:

$$G = \begin{bmatrix} A & \mathbf{t} \end{bmatrix} \quad ; \quad A = \begin{bmatrix} \mathbf{a}_1 & \mathbf{a}_2 \end{bmatrix}_{2 \times 2} \quad ; \quad \mathbf{t} = \begin{bmatrix} t_x \\ t_y \end{bmatrix}. \quad (5.3)$$

To find the transformation giving the best fit between X and Y , a least squares approach is used to minimise the sum of squared distances between corresponding points in both Y and Z . This is performed by differentiating the error function with respect to each of the variables (elements) in matrix A and vector \mathbf{t} as follows:

$$E = \arg \min \left\{ \sum_{k=1}^n \|\mathbf{z}_k - \mathbf{y}_k\|^2 \right\} \quad ; \quad \frac{\partial E}{\partial \boldsymbol{\phi}} = 0 \quad ; \quad \boldsymbol{\phi} = \begin{bmatrix} \text{vec}(A) \\ \text{vec}(\mathbf{t}) \end{bmatrix} \quad (5.4)$$

where the transformation parameters of A and \mathbf{t} can be arranged into the vector $\boldsymbol{\phi}$ as pose parameters. Then:

$$\begin{aligned} \frac{\partial E}{\partial \boldsymbol{\phi}} &= \frac{\partial E}{\partial \mathbf{z}_k^T} \cdot \frac{\partial \mathbf{z}_k^T}{\partial \boldsymbol{\phi}} \\ &= 2 \sum_{k=1}^n \frac{\partial \mathbf{z}_k^T}{\partial \boldsymbol{\phi}} \cdot (\mathbf{z}_k - \mathbf{y}_k) = 0 \end{aligned} \quad (5.5)$$

Since Z is a linear function of parameters in vector $\boldsymbol{\phi}$, $\frac{\partial \mathbf{z}_k^T}{\partial \boldsymbol{\phi}} = B_k$ is a matrix independent of $\boldsymbol{\phi}$. Hence, based on eqns (5.2) and (5.5):

$$\begin{aligned}
\frac{\partial E}{\partial \boldsymbol{\phi}} &\Rightarrow \sum_{k=1}^n B_k \mathbf{z}_k = \sum_{k=1}^n B_k \mathbf{y}_k \\
&= \sum_{k=1}^n B_k G \hat{\mathbf{x}} = \sum_{k=1}^n B_k \mathbf{y}_k
\end{aligned} \tag{5.6}$$

Finding the matrix G in eqn (5.6) leads to solving a set of six linear equations as modified into the following form:

$$GP = C \Rightarrow G = CP^{-1} \quad ; \quad \boldsymbol{\phi} = \text{vec}(G) \tag{5.7}$$

where P is a full rank square matrix obtained from the left side of eqn (5.6). Thus, solving eqn (5.7) results in unique answers for all parameters in the vector $\boldsymbol{\phi}$. The procedure for calculation of matrices B_K, P and C is shown below:

$$\mathbf{z}_k = G \hat{\mathbf{x}}_k = A \mathbf{x}_k + \mathbf{t} \tag{5.8}$$

$$Z = [\mathbf{a}_1 \quad \mathbf{a}_2] \begin{bmatrix} x \\ y \end{bmatrix} + \begin{bmatrix} t_x \\ t_y \end{bmatrix} = [x\mathbf{a}_1 + y\mathbf{a}_2 + \mathbf{t}]_{2 \times 1} \tag{5.9}$$

$$\begin{aligned}
B_k &= \frac{\partial \mathbf{x}_k^T}{\partial \boldsymbol{\phi}} \Rightarrow \\
\frac{\partial \mathbf{x}_k^T}{\partial \mathbf{a}_1} &= xI_2 \quad ; \quad \frac{\partial \mathbf{x}_k^T}{\partial \mathbf{a}_2} = yI_2 \quad ; \quad \frac{\partial \mathbf{x}_k^T}{\partial \mathbf{t}} = I_2. \\
B_k &= \begin{bmatrix} \mathbf{x}_k \\ \mathbf{1} \end{bmatrix} \otimes I_2 = \hat{\mathbf{x}}_k \otimes I_2
\end{aligned} \tag{5.10}$$

Matrix B_k is the Kronecker product of the shape matrix X with the 2D unit matrix. The matrices P and C are calculated using eqn (5.6) as follows:

$$C = \sum_{k=1}^n B_k \mathbf{y}_k = \hat{\mathbf{x}}_k \otimes \mathbf{y}_k = \text{vec} \left(\sum_{k=1}^n \mathbf{y}_k \hat{\mathbf{x}}_k^T \right) \quad (5.11)$$

$$\begin{aligned} \sum_{k=1}^n B_k \mathbf{z}_k &= (\hat{\mathbf{x}}_k \otimes I_2) \mathbf{z}_k = \mathbf{z}_k \hat{\mathbf{x}}_k^T = G \hat{\mathbf{x}}_k \hat{\mathbf{x}}_k^T \quad ; \quad P_k = \hat{\mathbf{x}}_k \hat{\mathbf{x}}_k^T \\ \sum_{k=1}^n B_k \mathbf{z}_k &= \text{vec} \left(G \sum_{k=1}^n P_k \right) \end{aligned} \quad (5.12)$$

Finally, based on eqns (5.12), (5.11) and (5.7), the value of the unknown parameters in vector ϕ can be computed. The given example in Figure 5.3 illustrates the alignment of two variations of the 2D prostate shape from different MR image slices.

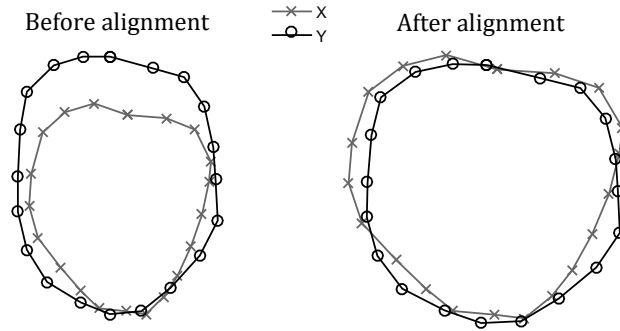


Figure 5.3: An example of aligning two variations of the prostate shape from the training set.

5.1.3 Statistical Model of the Prostate Shape

Upon shape alignment, a PCA is used to capture the significant principal axes across all distributed prostate shape points [73]. Reducing the dimensionality can greatly help to simplify the distribution and present the point cloud as

compactly as possible. Each principal axis describes a mode of variation of the prostate shape, such that landmark points tend to move together along the direction of this principal axis as shape varies.

To find the principal components, each prostate shape vector is defined as:

$$\mathbf{x} = (x_1, x_2, \dots, x_n, y_1, y_2, \dots, y_n)^T \quad (5.13)$$

and followed by:

$$\bar{\mathbf{x}} = \frac{1}{S} \sum_{i=1}^S \mathbf{x}_i \quad (5.14)$$

where $\bar{\mathbf{x}}$ is the prostate mean shape and S is the number of shape vectors. Deviation of each shape in the training set with respect to $\bar{\mathbf{x}}$ is calculated as follows:

$$\mathbf{dx} = \mathbf{x}_i - \bar{\mathbf{x}}. \quad (5.15)$$

The covariance matrix $\boldsymbol{\sigma}$ with dimensions of $2n \times 2n$ is computed using:

$$\boldsymbol{\sigma} = \frac{1}{S} \sum_{i=1}^S \mathbf{dx}_i \mathbf{dx}_i^T. \quad (5.16)$$

Finding the eigenvectors $\mathbf{p}_k (k = 1, \dots, 2n)$ of the covariance matrix provides all modes of variations in the cloud of landmark points so that the distribution can be described based on a set of orthogonal axes defined by the eigenvectors of $\boldsymbol{\sigma}$ in a $2n$ -dimensional space as:

$$\boldsymbol{\sigma} \mathbf{p}_k = \lambda_k \mathbf{p}_k \quad (5.17)$$

where λ_k is the k^{th} eigenvalue of the covariance matrix and $\lambda_k \geq \lambda_{k+1}$. The eigenvectors of $\boldsymbol{\sigma}$, corresponding to the largest eigenvalues, define the longest

axes of the elliptical distribution. In the other words, the eigenvector with the largest eigenvalue describes the most significant mode of variation (principal axis) of the prostate shapes. The typical variability of the shapes can be represented by a relatively small number of modes of variations t . This means that the $2n$ dimensional cloud of landmark points can be approximated by a t dimensional space such that ($t \ll 2n$). One option to calculate t is to choose as few modes as possible in order that the sum of their variances describes an appropriately large proportion of the total variance λ_T , where:

$$\lambda_T = \sum_{k=1}^{2n} \lambda_k. \quad (5.18)$$

Alternatively, the number of variations modes in the model can be selected in such a way that the model is able to reconstruct its training shapes with a sufficient level of accuracy based on the selected modes. In this research, t is determined by selecting the most significant eigenvectors necessary to reconstruct the training shapes at a 90% accuracy.

Taking the mean of the aligned training shapes $\bar{\mathbf{x}}$ and their mode of variation Φ , any shape in the training set \mathbf{x} can be approximated as:

$$\mathbf{x} = \bar{\mathbf{x}} + \Phi \mathbf{b} \quad (5.19)$$

where $\Phi = [\mathbf{p}_1, \mathbf{p}_2, \dots, \mathbf{p}_t]$ is the matrix of the first t eigenvectors and \mathbf{b} is a vector of weights known as the shape parameters.

It is essential to define limits for the shape parameters \mathbf{b} such that the new prostate shapes will be similar to those in the training set. This can be achieved by limiting the \mathbf{b}_i within $\pm 3\sqrt{\lambda_i}$ of distribution. Figure 5.4 shows an example of generated prostate shapes using the first three shape parameters of \mathbf{b} in turn within the specified limit. Therefore, the eqn (5.19) is defined as the

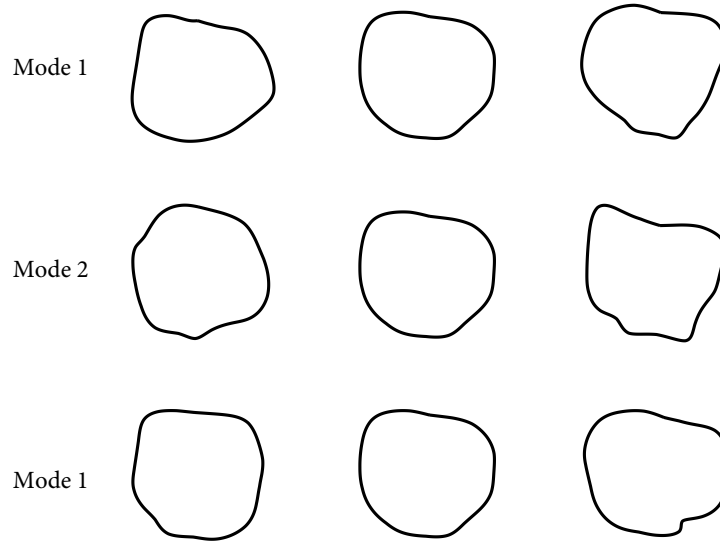


Figure 5.4: Example of generated prostate shapes based on the first three modes of variation.

shape model of the prostate. This can be applied to slices of new MR images in order to extract and segment the boundary of the prostate.

5.2 Fitting the ASM to a New Prostate Image

Once the shape model of a typical prostate is created, a search procedure is required to use the current model for segmenting the prostate from new unsighted MR images. The search procedure should involve finding both shape (\mathbf{b}) and pose (ϕ) parameters which describe the shape and position of the prostate in the new image. This procedure can be thought of as an optimisation problem, where a set of parameters are optimally estimated under an iterative search framework. An objective function is also incorporated into the optimisation process to measure the quality of the estimated parameters in each iteration. The parameters that best minimise the objective function are selected as the global solution. Putting these parameters in the shape model, eqn (5.19), results in segmenting the prostate.

5.2.1 Search Procedure

In the search method, the initial shape of the prostate is estimated by the mean shape using eqn (5.19) and by assigning the shape parameter \mathbf{b} equal to zero. The mean shape model is aligned with a default pose ϕ and located on the unsighted image roughly near the prostate boundary. Each model point then searches an area of the image to find the prostate boundary edges in each iteration. Once a better location (a stronger edge point) is found, the current model point is relocated to that new location in order to become closer to the intended boundary. These local movements of model points modify the shape and pose parameters. Constraining the shape parameter \mathbf{b} preserves the global shape of the prostate similar to those of the training set. The search procedure is stopped when no significant changes result.

5.2.2 Building a Greyscale Model

One way to determine the next movement for each model point is to search along normal to the current model points. Moving along the normal of each model point can lead to targeting stronger edges relating the prostate boundary. The search procedure is shown in Figure 5.5. This may not be always possible in practice, or model points may be located on a weaker secondary edge or so. Hence, a grey intensity model of each contour point from the training set is created to help in learning what search for in the image.

To create a statistical model of the greyscale for each model point, κ pixels are sampled along the profile from either side of each shape point in the i^{th} training image. Thus, $2\kappa + 1$ samples of the j^{th} training image can be stored in a vector \mathbf{g}_i . It should be noted that derivatives of grey pixels are sampled along

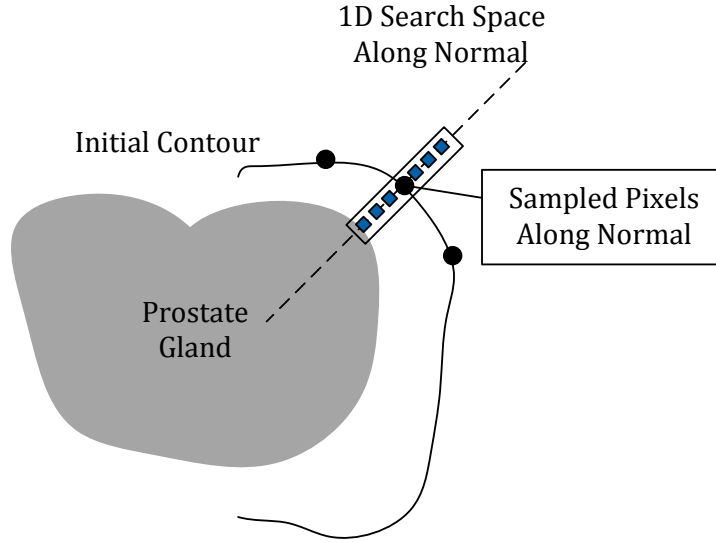


Figure 5.5: Search strategy for targeting the prostate edges.

the profile rather than their absolute value in order to minimise the effect of global intensity changes. Samples of vector \mathbf{g}_i are normalised through division by the sum of absolute elements values as:

$$\mathbf{g}_i \rightarrow \frac{1}{\sum_j |g_{ij}|} \mathbf{g}_i. \quad (5.20)$$

This is repeated for all S training images in order to obtain a set of normalised samples for each model point as $[\mathbf{g}_1, \mathbf{g}_2, \dots, \mathbf{g}_s]$. The obtained distribution is assumed to be a multivariate Gaussian, where its mean and covariance are estimated by $\bar{\mathbf{g}}$ and $\boldsymbol{\delta}_k$ respectively. It results in a statistical model of grey-level profile for the given model point. This is repeated for all model points to create their related grey-level model.

5.2.3 Objective Function

A objective function is incorporated in the searching procedure to evaluate each movement made by the shape model points. In the proposed function, a

vector of sampled pixels \mathbf{g}_k (along the normal of a model point) and a grey model of the current shape point (obtained in advance) are used to measure the Mahalanobis distance as:

$$\Gamma(\mathbf{g}_k) = (\mathbf{g}_k - \bar{\mathbf{g}}_k)^T \delta_g^{-1} (\mathbf{g}_k - \bar{\mathbf{g}}_k). \quad (5.21)$$

The Mahalanobis distance measures the distance of a point (new sample) from the mean of a distribution (grey-scale model) [37]. Minimising the objective function $\Gamma(\mathbf{g}_k)$ is interpreted as maximising the probability that \mathbf{g}_k belongs to the distribution, such that it can be the expected location for movement of the current model point.

To search for new locations, a 1D space is defined along the normal line by sampling m pixels either side of each model point such that ($m > \kappa$). As shown in Figure 5.6, the search space provides $2(m - \kappa) + 1$ possible locations where new grey pixels are sampled. The quality of fitting is then evaluated

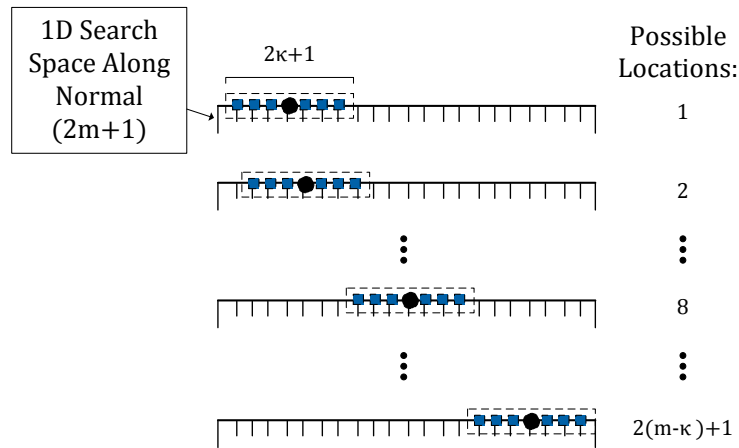


Figure 5.6: The search space for finding the prostate potential edges.

by the objective function for each possible location and the one which results in the lowest value is chosen for the next move. Searching and evaluation are repeated for all model points, giving a new location for each.

5.3 ASM Setup and Results

To implement and evaluate the ASM of the prostate gland, a set of image data, consisting of 40 MRIs from the MICCAI¹, were used for the training process. Ten MR images were reserved for testing. The outline of each prostate in each image slice was annotated with 60 points. Subject to the number of slices, each prostate shape was annotated with 800 points on average in this experiment. To create a greyscale model of the prostate mean shape, $\kappa = 8$ pixels were sampled along the profile from either side of the model points. By initialising the parameter m with 14, a search space with 29 pixels length provided 15 potential locations to be evaluated by the objective function.

The created shape model was used to segment new prostate images using an iterative procedure. To initialise the ASM, the mean shape model (an initial contour of the prostate) was placed on the new image, roughly overlapping the prostate boundary, which had been identified using elliptical filtering. Then, each model point was evaluated by the objective function for determining the next move towards a stronger edge (prostate boundary edges) in 100 iterations.

Although a very small set of training images (ten slices) was used in our experiment to build the shape model, the ASM of the prostate demonstrated promising results for fitting the shape model to new prostate images. Figure 5.7 shows some qualitative results of prostate segmentation with the ASM algorithm. It can be seen from the figure that in this preliminary experiment a wide variety of slices of MR images was used to evaluate the ability of the ASM method for coping with difficult conditions such as poor contrast, deformations of the prostate shape and presence of an endorectal coil in images. The average time of segmentation with the ASM method was less than a minute.

¹<http://promise12.grand-challenge.org/>

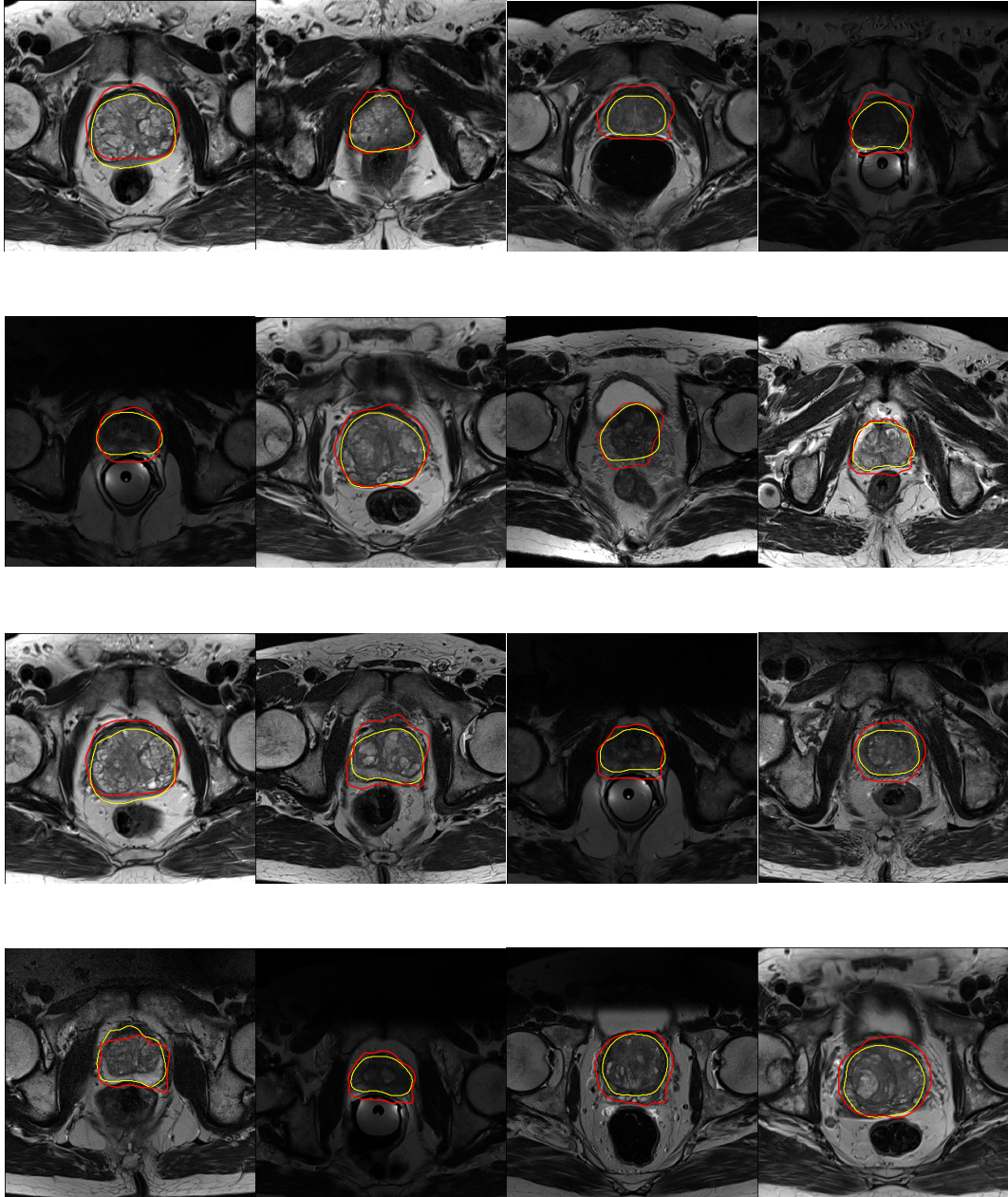


Figure 5.7: Prostate segmentations using the ASM method. The segmented prostates with the proposed method and reference are shown with red and yellow colours respectively.

5.4 Summary of Prostate Segmentation Using ASM

The proposed ASM method for segmentation of prostate shapes from slices of MR images can be summarised as consisting of two components: a training phase and shape model fitting.

1. **Training phase:** In the training phase, a model of the prostate's shape is created from a dataset of medical images. This is followed by the creation of a statistical grey-level model for the individual points of each aligned shape from the training images. Using the ASM and grey-level models, the prostate is detected and extracted from a given new image. The training phase needs to be executed once only. The flowchart of the training phase is illustrated in Figure 5.8.

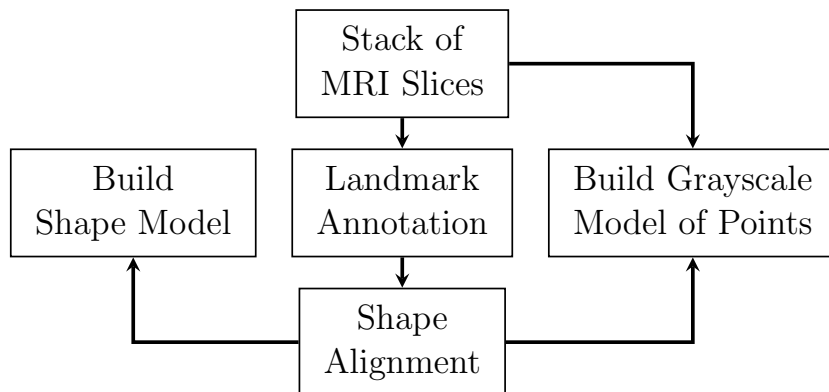


Figure 5.8: Flowchart of ASM training phase.

2. **Shape model fitting:** To do this, an initial shape of the prostate is generated using the shape model and considering the shape parameter \mathbf{b} equal to zero. To locate the initial shape on the image, a set of pose parameters (ϕ) as default is considered to transform the shape from model coordinate to image coordinate. A gray-level model for each

current model point is built and evaluated by the objective function to determine the movement of the corresponding model point to a better location. Repeating this for all current model points results in a new shape vector $\hat{\mathbf{x}}$. The shape parameter \mathbf{b} is computed through transforming the new shape back to the model coordinate. Thus, the new shape is regenerated based on the prostate ASM. This process continues until it satisfies the stopping criteria. Therefore, the segmented shape of the targeted prostate in the new image is represented by the last regenerated shape model. The procedure of fitting the shape model to a new image is given in Figure 5.9.

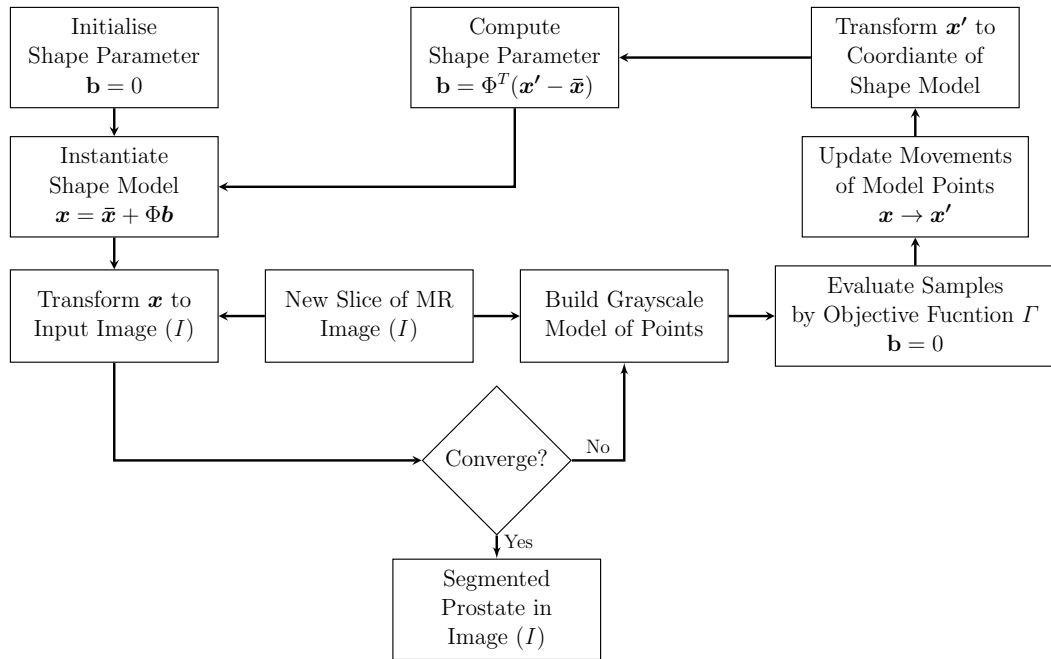


Figure 5.9: Flowchart for fitting the ASM to new slices of MR image.

Chapter 6

Active Appearance Model Segmentation

Overview

In this chapter, an active appearance model (AAM) of the prostate is proposed for improving the performance of the prostate segmentation. The AAM is an extension of the ASM method [29, 30]. In this context, in addition to the shape model, the proposed AAM method also explains the appearance of the prostate by a statistical texture model. Having created both shape and texture models, the AAM is applied to a new unsighted image for targeting the prostate region through minimising a cost function. It is expected that incorporating the shape and texture models will improve the accuracy of segmentation. Upon segmentation by the proposed AAM algorithm, a 3D surface model of the prostate is created from the segmented images slices.

A description of how an AAM of the prostate gland is constructed is given in Section 6.1. A number of well-known methods used to fit the AAM to new images are explained in Section 6.3. The experimental results of prostate

segmentation using the proposed AAM method are given in Section 6.4. The proposed AAM method is summarised in Section 6.5, accordingly. Finally, Section 6.6 describes the procedure for creating a 3D surface model of the prostate gland from the segmented images.

6.1 Active Appearance Model of the Prostate

An AAM of the prostate is created by modelling its typical shape and texture. Similar to ASM approaches, the shape model is learned by training with a set of images. The texture model is accordingly obtained by averaging the greyscale of the prostate's region over all training images, accompanied by the principal axes explaining the significant texture variabilities. For averaging, a transformation is used to warp the texture information of the prostate from each sample image into a reference template. Following sections describe how to create the models of shape and texture.

6.1.1 Shape Model

To create a shape model of the prostate, several steps are undertaken such as landmark annotation of each training image, alignment of shape vectors and application of the PCA to the aligned vectors. A detailed description of these steps is available in Section 5.1.

6.1.2 Texture Model

A statistical greyscale model of the prostate is constructed by sampling voxels from the region of the prostate in each training image and mapping them to the mean shape (reference) by means of a piecewise affine warping. This transformation results in a set of shape-free texture patches. A general flow

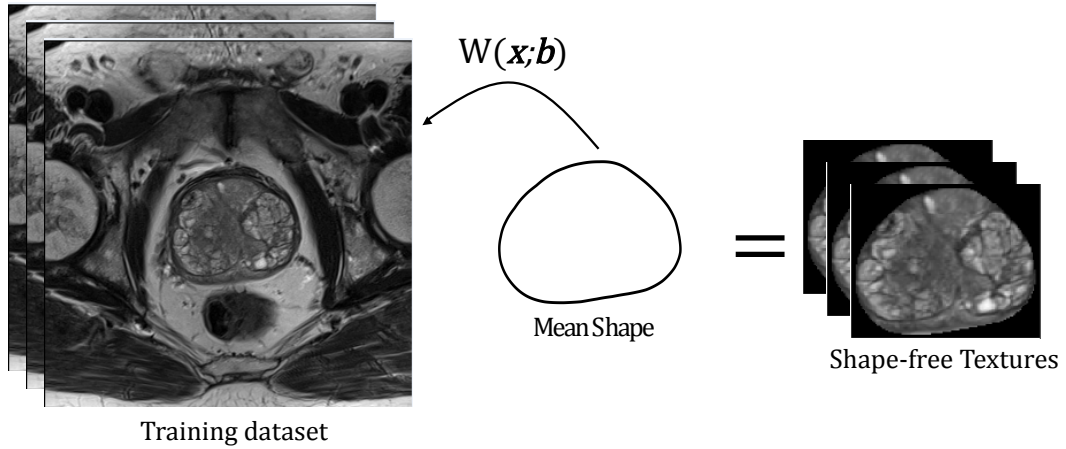


Figure 6.1: Prostate appearance warping using a piecewise affine function.

for warping the prostate appearance to the mean shape by a piecewise affine function $W(\mathbf{x}; \mathbf{b})$ is shown in Figure 6.1. Prior to warping an image using a piecewise affine function, the area of interest is triangulated using the Delaunay triangulation (DT) method [87, 138]. Although DT is a popular method for triangulation, it produces chaotic triangles when dealing with an irregular shape like the prostate. To overcome this, a innovative rotational triangulation was proposed in this research in order to produce organised triangles with respect to the centre of the prostate. Once it is created, the piecewise affine function is used to warp an image $I_{(x,y)}$ and sample voxels (bilinearly interpolated) in the image coordinate $I(W(\mathbf{x}; \mathbf{b}))$ and map the sampled intensity values to corresponding locations (pixel) in the mean shape coordinate. Each pixel \mathbf{v} in the mean shape is located inside a triangle with three vertices $\mathbf{x}_i, \mathbf{x}_j, \mathbf{x}_k$. Thus, one way to specify the location of the pixel \mathbf{v} is based on a linear combination of the triangle vertices (Barycentric coordinate) as follows:

$$\mathbf{v}_{(x,y)} = \begin{bmatrix} \mathbf{x}_i & \mathbf{x}_j & \mathbf{x}_k \end{bmatrix} \begin{bmatrix} \alpha \\ \beta \\ \gamma \end{bmatrix}, \quad (6.1)$$

for $0 \leq \beta, \gamma, \alpha \leq 1$:

$$\beta = \frac{v_y x_k - x_i v_y - x_k y_i - y_k v_x + x_i y_k + v_x y_i}{-x_j y_k + x_j y_i + x_i y_k + x_k y_j - x_k y_i - x_i y_j}$$

$$\gamma = \frac{v_x y_j - v_x y_i - x_i y_j - x_j v_y + x_j y_i + x_i v_y}{-x_j y_k + x_j y_i + x_i y_k + x_k y_j - x_k y_i - x_i y_j}, \quad (6.2)$$

$$\alpha = 1 - (\beta + \gamma)$$

where $(x_i, y_i), (x_j, y_j), (x_k, y_k)$, and (v_x, v_y) are locations of the related points in vectors $\mathbf{x}_i, \mathbf{x}_j, \mathbf{x}_k$, and \mathbf{v} , respectively. After obtaining the parameters from eqn (6.2), the corresponding pixel in the image coordinate can be computed as:

$$W(\mathbf{x}; \mathbf{b}) = \begin{bmatrix} \mathbf{x}'_i & \mathbf{x}'_j & \mathbf{x}'_k \end{bmatrix} \begin{bmatrix} \alpha \\ \beta \\ \gamma \end{bmatrix} \quad (6.3)$$

where $\mathbf{x}'_i, \mathbf{x}'_j, \mathbf{x}'_k$ denote the vertices of the corresponding triangle in the AAM mesh, as shown in Figure 6.2. These vertices are calculated from eqn (5.19) and based on the current shape parameters \mathbf{b} relating to each training image. Thus, combination of eqns (6.2), (6.3) results in an affine function as follows:

$$W(\mathbf{x}; \mathbf{b}) = \begin{bmatrix} a_2 & a_3 \\ a_5 & a_6 \end{bmatrix} \begin{bmatrix} v_x \\ v_y \end{bmatrix} + \begin{bmatrix} a_1 \\ a_4 \end{bmatrix} \quad (6.4)$$

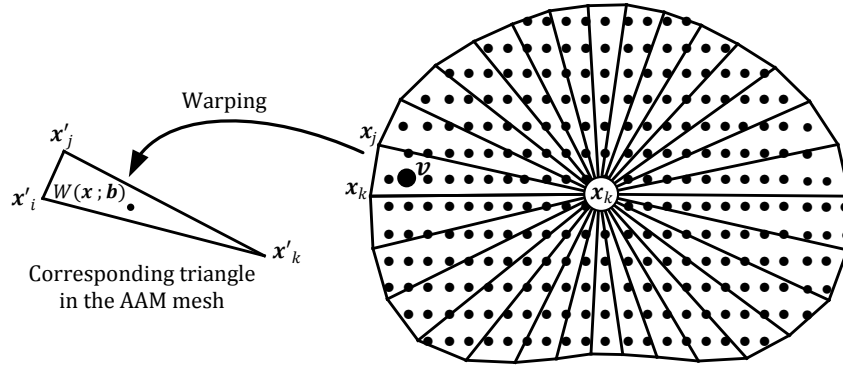


Figure 6.2: An example of prostate shape triangulation for piecewise affine warping.

where $(a_1, a_2, a_3, a_4, a_5, a_6)$, as 6 parameters of the warp function, are obtained from the shape parameters \mathbf{b} by combining eqns (5.19), (6.2) and (6.3). Note that the affine warp is computed for each triangle, not for each pixel.

Once computed, the warp function is applied on each training image and sample voxels in order to constitute a greyscale vector \mathbf{g}_{im} containing the intensity values of the prostate region. The vector \mathbf{g}_{im} is normalised in order to remove effects of illumination and lighting variation. The texture model is then represented as below:

$$\mathbf{g} = \bar{\mathbf{g}} + \Omega \mathbf{c} \quad (6.5)$$

where $\bar{\mathbf{g}}$ is the average of all greyscale vectors, Ω is the significant mode of appearance variations and \mathbf{c} denotes the texture parameters. As with the shape model, Ω is calculated by applying PCA to a set of greyscale vectors. Having created the texture model, the appearance of any prostate image in the training dataset can be reconstructed using eqn (6.5) and the corresponding texture parameters.

6.2 3D AAM of the Prostate

Constructing a 3D AAM of the prostate gland from 2D image slices is a non-trivial task. One way to build a 3D AAM is to perform the above steps for each set of corresponding slices from training images. For example, each slice from each training image that corresponds to the prostate is used to create an AAM for that specific part. To do this, patient MRIs are manually categorised based the region of the prostate they come from. To build the model in the thesis, 18 slices were used. In cases when the number of patient slices is different to this, interpolation can be used to transform the data to accord to the model. Once the MRI slices not containing the prostate have been manually removed, the subsequent process of interpolation and segmentation is automatic. These AAMs can be trained independently in a parallel manner. This enables us to construct a surface model of the prostate using a stack of 2D AAMs, each explaining a particular part of the prostate organ. An example of this can be seen in Figure 6.3, which shows a prostate surface along with its possible shape variations.

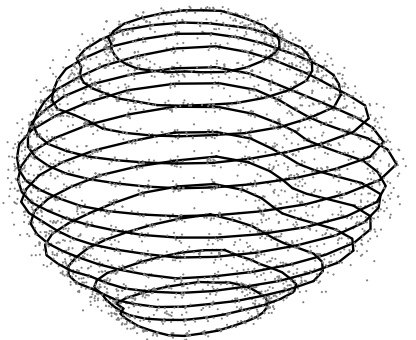


Figure 6.3: 3D AAM of the prostate along with its modes of variation.

6.3 Fitting the AAM to a New Prostate Image

Fitting a 3D AAM of the prostate to a new unsighted image is defined as a non-linear optimisation problem [8]. Thus, a non-linear least squares (NLS) technique is employed as an objective function to minimise the difference between a synthesised prostate image (obtained from AAM) and the test image. The objective function is denoted as:

$$E(\mathbf{q}) = \arg \min \left[T(\mathbf{x}) - I(W(\mathbf{x}; \mathbf{b})) \right]^2 \quad ; \quad \mathbf{q} = \begin{bmatrix} \mathbf{b} & \mathbf{c} \end{bmatrix}^T \quad (6.6)$$

where $T(\mathbf{x})$ is a synthesised prostate image (obtained from $\bar{\mathbf{g}}$) and $I(W(\mathbf{x}; \mathbf{b}))$ is the warped test image with respect to the shape parameters \mathbf{b} . The fitting goal is then to minimise eqn (6.6) with respect to the shape parameters \mathbf{b} and the texture parameters \mathbf{c} . Although the standard gradient descent is a well-known optimisation method to solve a NLS problem, it is computationally slow and inefficient since the image gradient and Jacobian and Hessian matrices need to be calculated in each iteration. To overcome this issue, the fitting problem is redefined as an image alignment problem, where a modified version of the Lucas–Kanade method known as simultaneous inverse compositional algorithm (SIC) is used to speed up the fitting process [98, 61].

The SIC algorithm performs the Gauss–Newton gradient descent simultaneously on the warp function $W(\mathbf{x}; \mathbf{b})$ with respect to shape parameters \mathbf{b} and texture parameters \mathbf{c} . The main difference between the SIC algorithm and the conventional gradient descent methods is that, instead of updating the shape parameters incrementally ($\mathbf{b} \leftarrow \mathbf{b} + \delta\mathbf{b}$), the SIC algorithm updates the warping function in an inverse compositional manner. This way of updating leads to pre-computing the Jacobian and image gradient matrices, hence saving

considerable computation time. The updating part at each iteration (t) is determined as follows:

$$W_{t+1}(\mathbf{x}; \mathbf{b}) \longleftarrow W_t(W(\mathbf{x}; \delta \mathbf{b})^{-1}; \mathbf{b}) \longleftarrow W_t(\mathbf{x}; \mathbf{b}) \circ W(\mathbf{x}; \delta \mathbf{b})^{-1} \quad (6.7)$$

where symbol \circ denotes the compositional operation and $W(\mathbf{x}; \delta \mathbf{b})$ the incremental warp. The incremental warp is inverted because it is computed with respect to the synthesised image $T(\mathbf{x})$ rather than the test image $I(W(\mathbf{x}; \mathbf{b}))$. Thus, reversing the role of the synthesised image and the test image in eqn (6.6) establishes the SIC algorithm, minimising:

$$E(\mathbf{q}) = \arg \min \left[T(W(\mathbf{x}; \delta \mathbf{b})) + \Omega(W(\mathbf{x}; \delta \mathbf{b}))(c + \delta c) - I(W(\mathbf{x}; \mathbf{b})) \right]^2. \quad (6.8)$$

Taking a first order Taylor expansion of eqn (6.8) and assuming $W(\mathbf{x}; \mathbf{0})$ as the identity warp gives:

$$\left[T(\mathbf{x}) + \nabla T \frac{\partial W}{\partial \mathbf{b}} \delta \mathbf{b} + (\Omega + \nabla \Omega \frac{\partial W}{\partial \mathbf{b}} \delta \mathbf{b})(c + \delta c) - I(W(\mathbf{x}; \mathbf{b})) \right]^2 \quad (6.9)$$

where ∇T , as the gradient of the synthesised image in directions $(\nabla T_x, \nabla T_y)$, and $\frac{\partial W}{\partial \mathbf{b}}$, as the Jacobian of the warp function, are computed in advance. Omitting second-order terms simplifies the above expression as:

$$E(\delta \mathbf{q}) = \arg \min_{\delta \mathbf{b}, \delta \mathbf{c}} \left[T(\mathbf{x}) + \Omega \mathbf{c} - I(W(\mathbf{x}; \mathbf{b})) + J \delta \mathbf{b} + \Omega \delta \mathbf{c} \right]^2 \quad ; \quad \delta \mathbf{q} = \begin{bmatrix} \delta \mathbf{b} & \delta \mathbf{c} \end{bmatrix}^T \quad (6.10)$$

where:

$$J = \left(\nabla T + \nabla \Omega \mathbf{c} \right) \frac{\partial W}{\partial \mathbf{b}} \delta \mathbf{b}. \quad (6.11)$$

The error between the given image and the model instance in eqn (6.10) is simultaneously minimised using a ℓ_2 norm with respect to the model

parameters. This requires the steepest descent image ($J\delta\mathbf{b} + \Omega\delta\mathbf{c}$) to be calculated in every iteration because it depends on the texture parameters $\delta\mathbf{c}$. In this study, we modified the initial SIC algorithm based on the work presented in [159], where a faster optimisation framework was used to estimate the two parameters of $\delta\mathbf{q}$ in eqn (6.10), such that:

$$\arg \min_{\delta\mathbf{b}, \delta\mathbf{c}} E(\delta\mathbf{b}, \delta\mathbf{c}) = \min_{\delta\mathbf{b}} \left[\min_{\delta\mathbf{c}} E(\delta\mathbf{b}, \delta\mathbf{c}) \right]. \quad (6.12)$$

Using this concept, eqn (6.10) is first optimised with respect to $\delta\mathbf{c}$ as:

$$\delta\mathbf{c} = \Omega^T \left(I(W(\mathbf{x}; \mathbf{b})) - T(\mathbf{x}) - \Omega\mathbf{c} - \nabla T \frac{\partial W}{\partial \mathbf{b}} \delta\mathbf{b} \right), \quad (6.13)$$

and then the solution (function of $\delta\mathbf{b}$) is sent back to the current equation. For the second time, it is optimised with respect to $\delta\mathbf{b}$ as below:

$$\delta\mathbf{b} = H^{-1} \Psi^T \left(I(W(\mathbf{x}; \mathbf{b})) - T(\mathbf{x}) \right), \quad (6.14)$$

where H and Ψ are the Hessian and steepest descent matrices, respectively, and are calculated as follows:

$$\Psi = \left(\nabla T \frac{\partial W}{\partial \mathbf{b}} \right) - \Omega \Omega^T \left(\nabla T \frac{\partial W}{\partial \mathbf{b}} \right) \quad ; \quad H = \Psi^T \Psi. \quad (6.15)$$

These steps are repeated in each iteration and the model parameters are updated accordingly until the stopping criterion is met. The texture parameters are updated in a common additive manner ($\mathbf{c} \leftarrow \mathbf{c} + \delta\mathbf{c}$), while the shape parameters are indirectly updated using eqn (6.7).

6.4 Results and Discussion

The MICCAI¹ dataset was used to construct an AAM of the prostate gland. The model was created from 10 cases, having an average voxel size of $0.3905 \times 0.3905 \times 3.3$ mm. In order to compare the AAM results with the ASM approach presented in Chapter 5, the same image set was used for training and testing of the ASM under identical conditions. To reproduce the training examples at a 90% accuracy the first 4 significant eigenvectors (modes) were used. Leave-one-out cross validation (LOOCV) was used to evaluate the performance of each proposed algorithm during the training phase. This meant that each image was removed in turn from the training set and a model created. The image that had been removed was then automatically segmented using the model.

The two common measures of the dice similarity coefficient (DSC) and Hausdorff distance (HD) were used to measure the accuracy of the segmentation results against a manually segmented reference. The DSC specifies the overlap between the segmented image (X) and its reference (Y) with a number from zero (minimum) to one (maximum) and computed as:

$$D(X, Y) = \frac{2|X \cap Y|}{|X| + |Y|}. \quad (6.16)$$

HD is a metric that specifies how much (in terms of distance) two surfaces are dissimilar. It returns the farthest distance of a surface point in X from any point in Y and vice versa, meaning that, if the HD distance is (d), then each surface point of X must not be beyond a distance (d) of some point of Y and

¹<http://promise12.grand-challenge.org/>

Table 6.1: Segmentation accuracy of ASM and AAM during the model training using leave-one-out cross validation of 10 cases.

Methods	DSC		95% HD	
	Mean	Median	Mean	Median
ASM	0.79	0.78	33.57	27.73
AAM	0.82	0.83	19.48	20.91

vice versa. It is computed as:

$$\begin{aligned} \text{HD}(X, Y) &= \max\{h(X, Y), h(Y, X)\} \\ h(X, Y) &= \max_{x \in X} \{\min_{y \in Y} \mathbf{d}(x, y)\}, \end{aligned} \tag{6.17}$$

where the operator (\mathbf{d}) indicates the Euclidean distance. Since the HD is susceptible to outliers, the 95th percentile of the HD is usually used rather than its maximum.

The segmentation accuracy of both ASM and AAM during the model training based on LOOCV is shown in Table 6.1. Although the ASM and the AAM algorithms both resulted in a close mean DSC of 0.79 and 0.82 in turn, the AAM obtained a considerably lower HD than the ASM during the training phase. This is mainly because the ASM point models are susceptible to noise for finding the actual prostate edges.

Once the training was completed, the accuracy of each model was tested by automatically segmenting the adjacent images to the prostate mid-gland, which had not been included in the dataset for model building. Table 6.2 compares the accuracy of the proposed AAM algorithm against the ASM method for segmentation of unsighted images of 10 cases. Based on the obtained results, the AAM achieved an average DSC of 0.87 and HD of 17.56, while an average DSC of 0.78 and HD of 38.03 was found by the ASM approach. The AAM algorithm was also fairly robust in achieving consistent DSC rate for different

Table 6.2: Comparing the accuracy of the proposed AAM against the ASM approach for segmenting unsighted images of 10 cases.

Images	ASM		AAM	
	95% HD	DSC	95% HD	DSC
Case 26	66.73	0.66	12.94	0.91
Case 27	59.47	0.68	20.51	0.80
Case 28	61.05	0.7	9.8	0.94
Case 29	33.19	0.87	15.5	0.92
Case 30	19.93	0.88	19.31	0.84
Case 31	43.34	0.76	23	0.82
Case 32	21.13	0.84	11.77	0.90
Case 33	34.10	0.81	13.07	0.85
Case 34	38.23	0.69	21.56	0.80
Case 36	23.14	0.86	28.17	0.90
Average±std	38.03±16.35	0.78±0.08	17.56±5.28	0.87±0.04

cases. Overall, the experimental results indicate that the proposed AAM improved the accuracy of prostate segmentation when compared to the earlier ASM approach.

Figure 6.4 shows the qualitative results of prostate segmentation using the AAM algorithm for each of the 10 cases in the test data set. It can be seen that a wide variety of MR images was used to evaluate the AAM method under a variety of difficult conditions, including poor contrast and deformations of the prostate. The qualitative results of the ASM approach have already been shown in Figure 5.7.

To evaluate computation speeds, the AAM and ASM algorithms were run under the same conditions for prostate segmentation of MICCAI image sets on a PC with a 2.5 GHz Intel CPU and 8 GB of RAM. The average computation times of 20.6 and 8.5 seconds per slices were recorded for the ASM and AAM, respectively. The AAM algorithm computes the model parameters at least twice faster than the ASM approach. It is worth noting that the

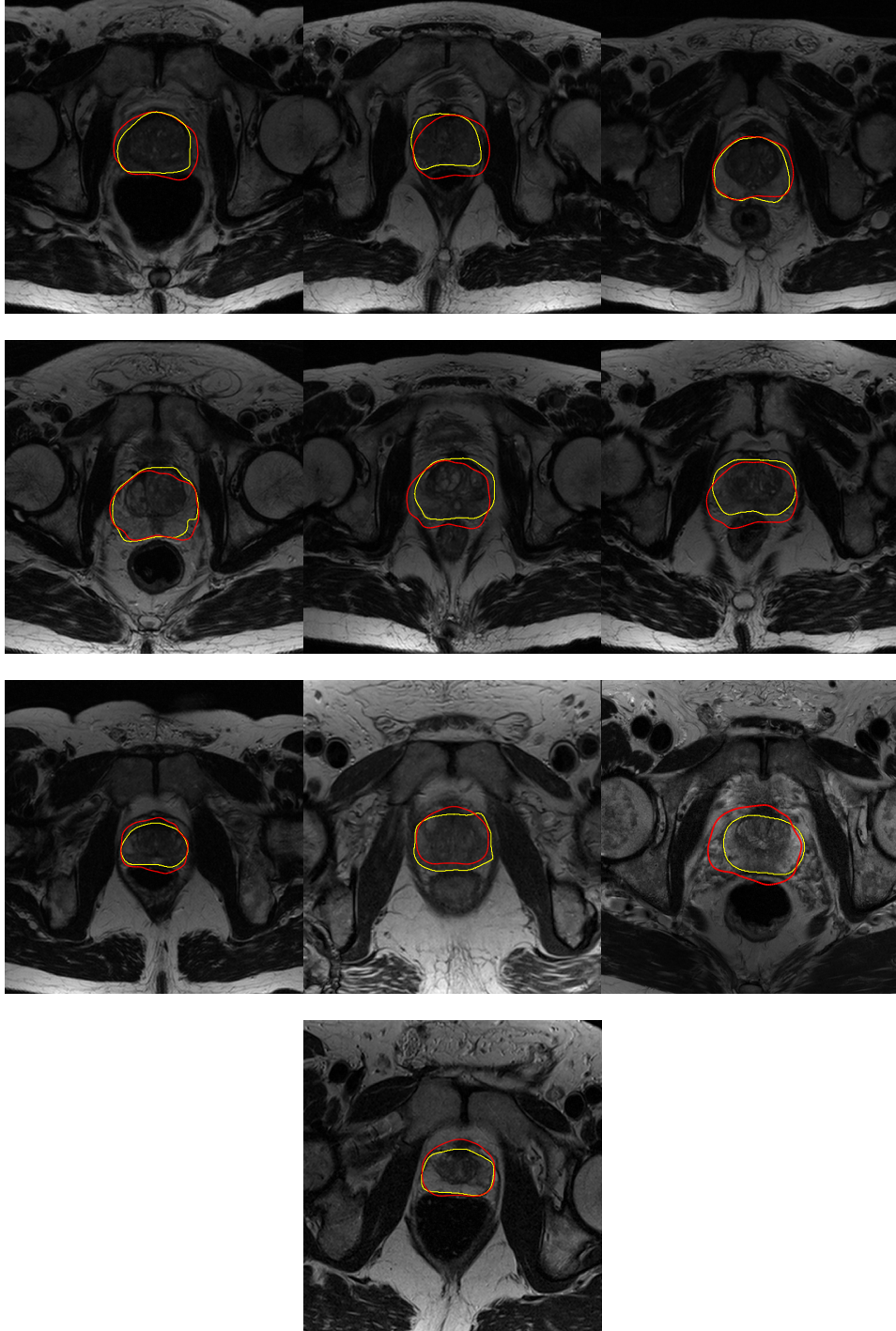


Figure 6.4: Qualitative segmentation results of 10 cases (from upper left) using the proposed algorithm. The segmented prostates with our method and reference are shown with red and yellow colours, respectively.

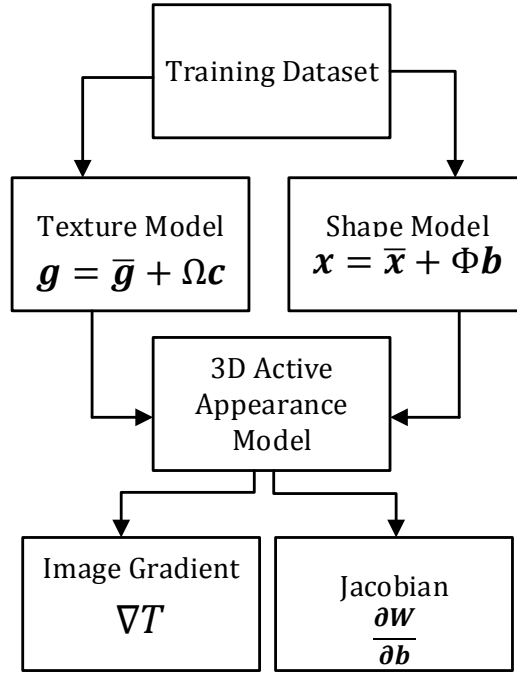


Figure 6.5: A flowchart for constructing a 3D AAM of the prostate image

ASM algorithm estimates the shape parameters only, whereas in the AAM both shape and texture parameters are estimated. To compensate for the computation cost, the proposed AAM algorithm employs a modified version of the SIC to estimate the shape and texture parameters using a computationally fast iterative optimisation scheme.

6.5 Summary of Prostate Segmentation Using AAM

The AAM, as an extension of ASM, accompanies the prostate shape model with a texture model explaining the prostate appearance. A surface model of the prostate is then constructed from a set of 2D AAMs, each corresponding to a particular region of the gland. A schematic diagram of constructing a 3D AAM of the prostate is shown in Figure 6.5. Fitting the 3D AAM to

a new prostate image is a non-linear optimisation problem. A modified SIC algorithm is proposed to perform an accurate prostate segmentation which is computationally faster than conventional gradient descent algorithms. In the SIC algorithm, the initial image gradient and Jacobian matrices are precomputed in advance during the training phase and the AAM shape parameters are updated in an inverse compositional manner. Also, the steepest descent is calculated in the subspace orthogonal to the texture vector space. In the modified version, an optimisation procedure is used to estimate the model parameters more efficiently, leading to a faster and more accurate segmentation. A diagram of AAM fitting can be seen in Figure 6.6.

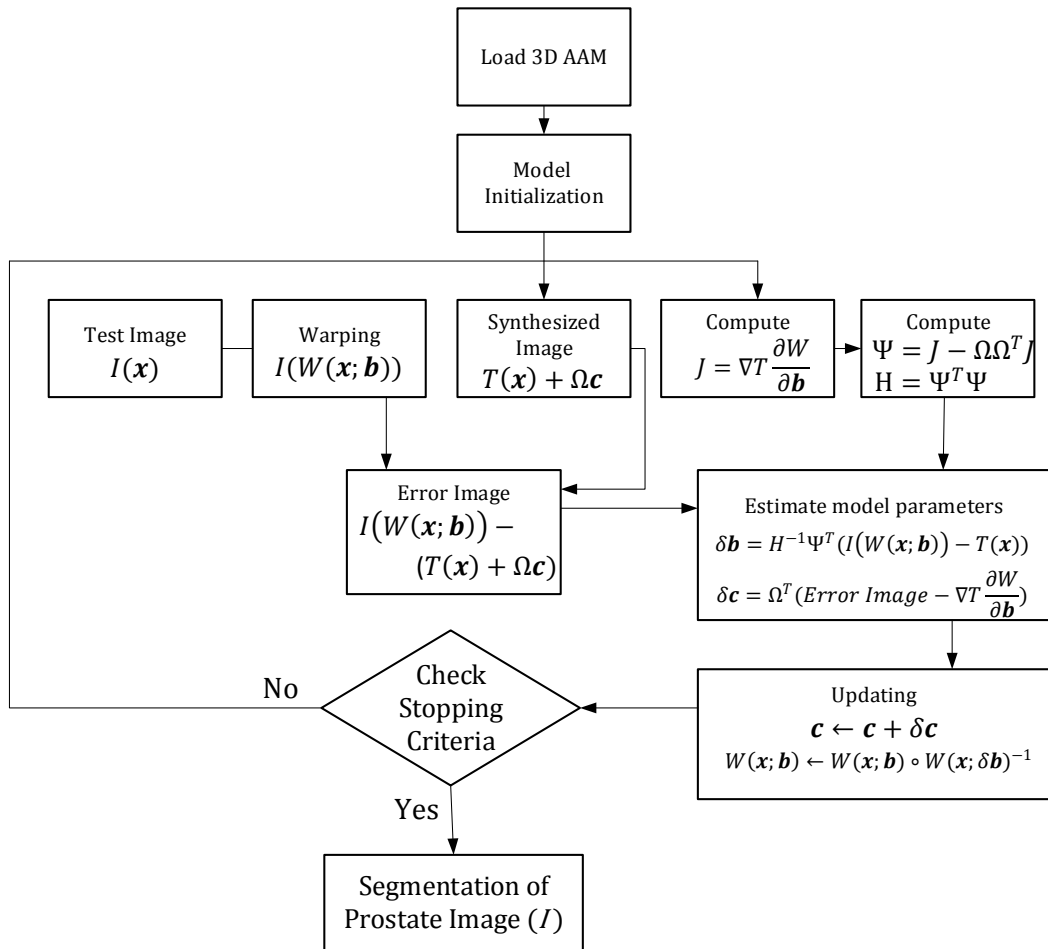


Figure 6.6: Diagram of fitting the 3D AAM to a new prostate image.

6.6 Constructing the Prostate Surface Model

Before constructing a 3D model of the prostate, to follow the same order, each segmented slice in each image set is stacked along the z axis, covering from the base to the apex located at either sides of the prostate. Moreover, slices not containing the prostate are automatically removed from the dataset. Automatic detection of these slices is trivial since the segmented images are in a binary format.

Posed in this manner, a set of points is extracted from the boundary of the prostate in each remaining slice. Boundary point extraction is similar to the point annotation step for ASM and AAM described in Section 5.1.1, where we developed a rotational-based algorithm for automatic point selection from the boundary of a rounded object, including the prostate gland. Hence, the prostate surface is represented by a compact model based on a set of 3D points, where this significantly reduces the dimensionality of the data. To get a better insight into the topology of the points, the DT algorithm is used to triangulate the prostate surface points to retain the connectivity information. Thus, as shown in Figure 6.7, the prostate model is represented by a 3D mesh which is constructed from a set of polygons containing the 3D point as vertices and the connectivity information as faces. For visualising the prostate model, computer graphic techniques are used to account for camera positioning and lighting effects.

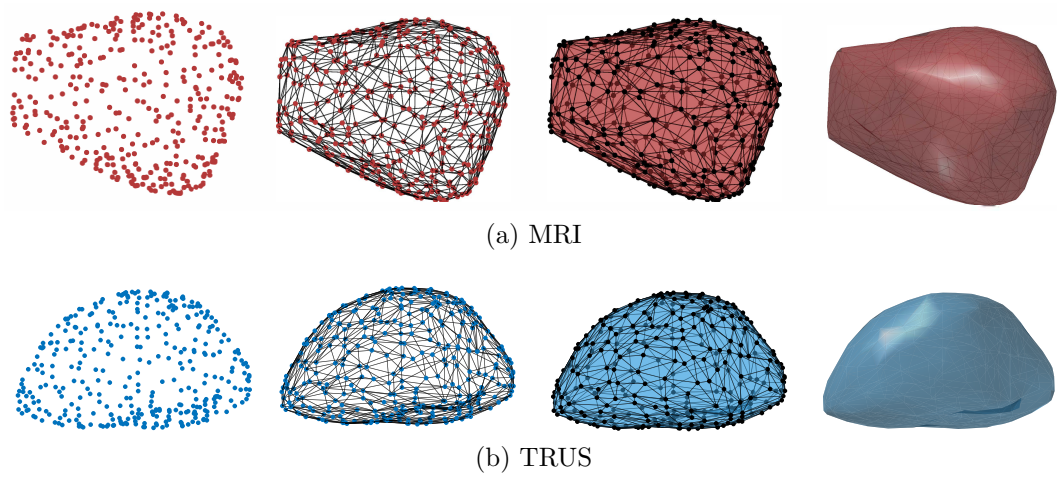


Figure 6.7: 3D surface model of the prostate.

Chapter 7

Literature Review: Medical Image Registration

Overview

Depending on the medical image content, a registration problem can be categorised as either an intensity-based approach or a surface-based approach. Intensity-based methods register a source image to the target image by finding and matching intensity patterns in both images using mathematical criteria. These methods perform well for mono-modal registration applications, where the intensity of the imaging modality does not dramatically change over the course of registration [148, 142, 39]. In surface-based methods, a correspondence between identical landmarks (geometrical features) of source and target images is established and used to drive a spatial transformation function for point mapping from the source into the target with the objective of minimising the error between the two surfaces. Surface-based methods underpin the current study as they are commonly used for multi-modal image fusion.

Surface-based registration methods are conventionally classified into rigid and deformable (non-rigid) groups [35, 126]. Rigid methods perform a set of linear transformations on the object of interest in order to map the object into the target, whereas deformable methods use non-linear transformations to enable a more flexible movement of points. The rest of this chapter describes both rigid and non-rigid registration methods and their applications for MRI-TRUS fusion.

7.1 Rigid Registration

The key property of rigid-body transformation methods is that they do not deform the shape of an object, thereby preserving the distance between each pair of points. A simple version of a rigid transformation consists of applying rotation, R , and translation, \mathbf{t} , as:

$$\hat{\mathbf{x}} = T(\mathbf{x}) = R\mathbf{x} + \mathbf{t}, \quad (7.1)$$

where $\hat{\mathbf{x}}$ is the transformed version of a given point \mathbf{x} and R is an orthogonal matrix ($R^T = R^{-1}$) whose determinant is unity. A rigid registration is a special case of affine transformation in which scaling, reflection and shearing transformations are avoided. In general, an isotropic scaling factor s can be multiplied to the rotation matrix in eqn (7.1) to mitigate the global scaling difference between the two point sets. A solution to rigid registration of two surfaces is equivalent to the alignment problem described in Section 5.1.2.

7.2 Deformable Registration

Deformable registration (non-rigid) methods allows the local warping of an object's shape. This feature enables a registration method to capture both global and local changes while dealing with elastic phenomena. In general, a non-rigid registration of two surfaces X and Y is represented in the form of an objective function as:

$$\mathcal{M}(Y, T(X, \Theta)) + \mathcal{R}(\Theta), \quad (7.2)$$

where the goal is to estimate the optimal parameters Θ of a transformation model T that optimise the above equation [142]. The objective function typically consists of three main components: a similarity measure, a transformation model, and a regularisation term. The matching criterion or similarity measure, $\mathcal{M}(\cdot)$, quantifies the degree of match between two surfaces. The regularisation term, $\mathcal{R}(\cdot)$, constrains the transformation parameters that cause abnormal deformations in the shape of the structure of interest. It is mainly used to guarantee convergence and mitigate the difficulty associated with solving an ill-posed problem of non-rigid registration. The optimisation method to either maximise or minimise this objective function is counted as an additional component of the algorithm and it is determined based on how a similarity measure is chosen. In surface-based registration approaches, the similarity measure is defined as either sum of squared distances or the probability of points in one set of matching points in the other set.

Of all existing non-rigid registration methods, robust point matching (RPM) by Haili et al. [25, 122] and coherent point drift (CPD) by Myronenko et al. [107] appear to be the most frequently used algorithms for non-rigid point set registration. Each method uses a relatively different approach for

finding the correspondence between two point sets as well as estimating the parameters of the transformation function. The following sections describe our derivation of the CPD and RPM methods as a basis for comparison since they are the most relevant to our research.

7.2.1 Coherent Point Drift

In this method, the registration task is defined as a problem of probability density estimation, such that individual points in one set are considered Gaussian mixture model (GMM) centroids and those in the other set are considered data points. Divided into two steps, an expectation-maximisation (EM) algorithm, [41, 103], is used to find the probabilistic (fuzzy) correspondence of each data point to each distribution by maximising the posterior probability of GMM in its E-step, and to estimate the transformation parameters using the current correspondence in its M-step iteratively. To avoid undesirable deformations, a regulariser is used to force points to move coherently.

The non-rigid registration of a source point X to a target point Y is defined below as:

$$X = \left[\mathbf{x}_1 \cdots \mathbf{x}_n \cdots \mathbf{x}_N \right] \xrightarrow{T} Z = \left[\mathbf{z}_1 \cdots \mathbf{z}_n \cdots \mathbf{z}_N \right] \approx Y = \left[\mathbf{y}_1 \cdots \mathbf{y}_m \cdots \mathbf{y}_M \right] \quad (7.3)$$

where point set Z approximates the target point set Y and is obtained using a mapping function F as:

$$\mathbf{z}_n = T(\mathbf{x}_n; \Theta) \text{ or } Z = T(X; \Theta) \text{ such that } Z \approx Y \quad (7.4)$$

All points have dimensionality D . An illustration of a 2D case is given in

Figure 7.1. In addition to finding the parameters Θ of the mapping T , the

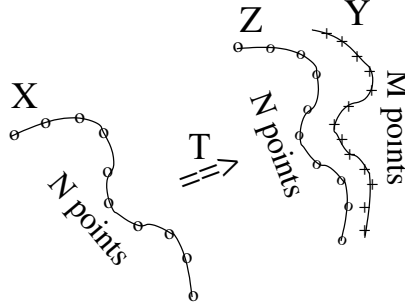


Figure 7.1: Illustration of mapping/registration of 2D points X and Y using function T as in eqn (7.4).

correspondence between points X and Y needs to be determined. To solve the correspondence problem, the GMM is defined as:

$$p(\mathbf{y}_m) = \sum_{n=1}^{N+1} P(n)p(\mathbf{y}_m|n). \quad (7.5)$$

To calculate eqn (7.5), it is assumed that the gaussian distributions are centred around $z_n \in Z$, and have equal isotropic covariance σ^2 .

For each $n \in (1, \dots, N)$:

$$p(\mathbf{y}_m|n) = \frac{1}{(2\pi\sigma^2)^{D/2}} \exp\left(-\frac{\|\mathbf{y}_m - \mathbf{z}_n\|^2}{2\sigma^2}\right) = \frac{1}{(2\pi\sigma^2)^{D/2}} \exp\left(-\frac{h_{nm}}{2\sigma^2}\right), \quad (7.6)$$

where h_{nm} are the squares of the Euclidean distances between points \mathbf{y}_m and \mathbf{z}_m defined as:

$$h_{nm} = \|\mathbf{y}_m - \mathbf{z}_n\|^2 = (\mathbf{z}_n - \mathbf{y}_m)^T \cdot (\mathbf{z}_n - \mathbf{y}_m), \quad H = [h_{nm}]_{N \times M}, \quad (7.7)$$

and H is an $N \times M$ matrix of the squared distances between points \mathbf{z}_n and

\mathbf{y}_m . An equal membership probability is defined for all distributions:

$$P(n) = \frac{1}{N}. \quad (7.8)$$

An additional uniform distribution ($n = N + 1$) accounts for noise and outliers as

$$p(\mathbf{y}_m|N + 1) = \frac{1}{M}. \quad (7.9)$$

For each \mathbf{y}_m , the uniform distribution contributes the weight $0 \leq \omega \leq 1$ to the model so that the complete mixture model of eqn (7.5) is:

$$p(\mathbf{y}_m) = \frac{\omega}{M} + \frac{1 - \omega}{N} \sum_{n=1}^N p(\mathbf{y}_m|n), \quad (7.10)$$

where $p(\mathbf{y}_m|n)$ are Gaussians as in eqn (7.6).

The first task is to find the optimal parameters Θ of the mapping $Z = T(X; \Theta)$ and σ^2 of the distribution $p(\mathbf{y}_m|n)$. This is done by minimising the negative log-likelihood function

$$\mathcal{E}(\Theta, \sigma^2) = - \sum_{m=1}^M \log p(\mathbf{y}_m) = - \sum_{m=1}^M \log \sum_{n=1}^{N+1} P(n)p(\mathbf{y}_m|n). \quad (7.11)$$

Thus, the correspondence between points \mathbf{z}_n (\mathbf{x}_n) and \mathbf{y}_m is defined as the posterior probability of the GMM centroids \mathbf{z}_n given the points \mathbf{y}_m , that is,

$$P(n|\mathbf{y}_m) = \frac{P(n)p(\mathbf{y}_m|n)}{p(\mathbf{y}_m)}. \quad (7.12)$$

To estimate the transformation parameters Θ and covariance σ^2 , an EM algorithm minimises eqn (7.11) using a complete log-likelihood function,

namely:

$$Q = - \sum_{m=1}^M \sum_{n=1}^{N+1} P(n|\mathbf{y}_m) \log(P(n)p(\mathbf{y}_m|n)). \quad (7.13)$$

Ignoring terms independent of (Θ, σ^2) , the objective function Q can be written as

$$Q(\Theta, \sigma^2) = \frac{1}{2\sigma^2} \sum_{m=1}^M \sum_{n=1}^N p_{nm} h_{nm} + \frac{\bar{p}D}{2} \log \sigma^2 \quad (7.14)$$

where

$$p_{nm} = P(n|\mathbf{y}_m); \quad P = \{p_{nm}\}_{N \times M} \quad (7.15)$$

and

$$\bar{p} = \sum_{m=1}^M \sum_{n=1}^N P(n|\mathbf{y}_m) = \mathbf{1}_N^T \cdot P \cdot \mathbf{1}_M = \mathbf{1}_M^T \cdot P^T \cdot \mathbf{1}_N. \quad (7.16)$$

Note that $\bar{p} \leq M$ and $\bar{p} = M$ only if $\omega = 0$. We denote by $\mathbf{1}_M$ a column vector of M ones. Such a vector of ones is convenient to describe summation and also replication of another vector.

The posterior probabilities can be evaluated using eqn (7.12) as:

$$p_{nm} = P(n|\mathbf{y}_m) = \frac{\frac{1-\omega}{N} \frac{1}{(2\pi\sigma^2)^{D/2}} \exp(-\frac{h_{nm}}{2\sigma^2})}{\frac{\omega}{M} + \frac{1-\omega}{N} \frac{1}{(2\pi\sigma^2)^{D/2}} \sum_{k=1}^N \exp(-\frac{h_{km}}{2\sigma^2})}$$

and can be re-written as:

$$p_{nm} = P(n|\mathbf{y}_m) = \frac{\exp(-\frac{h_{nm}}{2\sigma^2})}{c + \sum_{k=1}^N \exp(-\frac{h_{km}}{2\sigma^2})} \quad (7.17)$$

where:

$$c = \frac{\omega}{1-\omega} \frac{N}{M} (2\pi\sigma^2)^{\frac{D}{2}} \quad (7.18)$$

or, in a matrix form:

$$P = E /_r (c + \mathbf{1}_N \cdot E) \quad ; \quad E = \exp\left(-\frac{H}{2\sigma^2}\right) \quad (7.19)$$

where the matrix H is specified in eqn (7.7) and $/_r$ denotes division of a matrix by a row vector on a row-by-row basis.

Now, to perform a non-rigid registration, the mapping transformation T is implicitly defined as a displacement function v :

$$\mathbf{z}_n = \mathbf{x}_n + v(\mathbf{x}_n) \quad \text{or} \quad Z = X + v(X). \quad (7.20)$$

In order to force points to deform smoothly and coherently, a regularisation term is added to the objective function in eqn (7.14) to get:

$$Q(v, \sigma^2) = \frac{1}{2\sigma^2} \sum_{m=1}^M \sum_{n=1}^N p_{nm} h_{nm} + \frac{\bar{p}D}{2} \log \sigma^2 + \frac{\lambda}{2} \|Lv\|^2 \quad (7.21)$$

where L is a differential regularisation operator acting on the function v and $\|Lv\|^2$ is the square of its norm. Also, the coefficient λ is used to trade-off between transformation forces and the regularisation term. It is a well-known fact that the function v that minimises the objective function 7.21 must satisfy the following Euler–Lagrange differential equation:

$$\frac{1}{\sigma^2 \lambda} \sum_{m=1}^M \sum_{n=1}^N p_{nm} (\mathbf{z}_n - \mathbf{y}_m) \delta(\mathbf{u} - \mathbf{x}_n) = \hat{L}Lv(\mathbf{u}) \quad (7.22)$$

for all vectors \mathbf{u} , where \hat{L} is the adjoint operator to L and \mathbf{z}_n is given in eqn (7.20). The solution to such a differential equation is written in terms of a Green’s function G of the self-adjoint operator $\hat{L}L$ in the following form:

$$v(\mathbf{u}) = \frac{1}{\sigma^2 \lambda} \sum_{m=1}^M \sum_{n=1}^N p_{nm}(\mathbf{z}_n - \mathbf{y}_m) \cdot G(\mathbf{u}, \mathbf{x}_n) = \sum_{n=1}^N \mathbf{w}_n \cdot G(\mathbf{u}, \mathbf{x}_n) \quad (7.23)$$

where:

$$\mathbf{w}_n = \frac{1}{\lambda \sigma^2} \sum_{m=1}^M p_{nm}(\mathbf{z}_n - \mathbf{y}_m) \quad (7.24)$$

where \mathbf{w}_n is a $D \times 1$ vector of coefficients being an n th column of a respective matrix W . The Green's function can be selected to be a matrix of Gaussians with the entries:

$$g_{k,n} = G(\mathbf{x}_k, \mathbf{x}_n) = \exp\left(-\frac{\|\mathbf{x}_k - \mathbf{x}_n\|^2}{2\beta^2}\right). \quad (7.25)$$

This can be calculated as:

$$\mathcal{X} = X^T \cdot X, \quad G = \exp\left(-\frac{\mathcal{X}}{2\beta^2}\right). \quad (7.26)$$

Re-writing eqn (7.23) in the matrix form yields the displacement function:

$$v(X) = W \cdot G. \quad (7.27)$$

Having $v(X)$ calculated, new positions of point set X are updated according to eqn (7.20) as:

$$Z = X + W \cdot G. \quad (7.28)$$

The optimal value of σ^2 is given by

$$\sigma^2 = \frac{1}{\bar{p}D} \text{tr}(H \cdot P^T), \quad (7.29)$$

where H is specified in eqn (7.7).

Overall, the EM algorithm updates the probabilistic correspondence matrix P in the E-step (eqn 7.19) and the displacement function $v(X)$ in the M-step (eqn 7.27) iteratively. The source points X and covariance σ^2 are also updated in the M-step according to eqns (7.28) and (7.29) respectively. Meanwhile, parameters λ and β control the amount of smoothness regularisation. Finally, the algorithm converges when the value of σ^2 drops below a certain threshold.

7.2.2 Robust Point Matching

RPM constitutes a dual-step optimisation algorithm for finding both the point correspondence and spatial mapping function iteratively, in which the correspondence between two point sets is defined as a linear assignment problem, [115], and spatial transformation is based on a thin-plate spline (TPS) [17]. Hence, the general objective function to map a point set X to Y involves two interlocking optimisation criteria as correspondence matrix C and spatial function T , namely:

$$\begin{aligned}
E(C, T) = & \sum_{i=1}^N \sum_{j=1}^M c_{ij} \|\mathbf{x}_i - T(\mathbf{y}_j)\|^2 + \lambda \|LT\|^2 - \alpha \sum_{i=1}^N \sum_{j=1}^M c_{ij} \\
& + \tau \sum_{i=1}^N \sum_{j=1}^M c_{ij} \log c_{ij} ; \quad C = [c_{ij}]_{N \times M}
\end{aligned} \tag{7.30}$$

where L is an operator constraining the mapping function T to perform reasonably smoothly and the parameter λ weights this smoothness. Further, a detailed discussion will be given in regard to the smoothness measure and the type of mapping function. Each element $c_{ij} \in \{0, 1\}$ of matrix C indicates a binary correspondence between the i^{th} point in set X to the j^{th} point in the set Y , such that $C_i \cdot \mathbf{1}_{M+1} = 1$ for $i \in \{1, 2, \dots, N\}$ and $\mathbf{1}_{N+1}^T \cdot C_j = 1$

for $j \in \{1, 2, \dots, M\}$. These constraints are applied to guarantee one-to-one correspondence between pairs of points. The extra row $N + 1$ and column $M + 1$ are appended to the correspondence matrix to handle outliers. Thus, if point \mathbf{x}_i corresponds to point \mathbf{y}_j then $c_{ij} = 1$, otherwise $c_{ij} = 0$. Also, to comply with constraints, extra entries will take non-zero values in case a point is rejected as an outlier. An example of a correspondence matrix including outlier can be represented as:

$$\begin{array}{c}
 \mathbf{y}_1 \\
 \mathbf{y}_2 \\
 \mathbf{y}_3 \\
 \mathbf{y}_4 \\
 \text{outlier}
 \end{array}
 \begin{array}{c}
 \mathbf{x}_1 \quad \mathbf{x}_2 \quad \mathbf{x}_3 \quad \mathbf{x}_4 \quad \mathbf{x}_5 \quad \mathbf{x}_6 \quad \text{outlier} \\
 \left[\begin{array}{cccccc|c}
 0 & 0 & 0 & 1 & 0 & 0 & 0 \\
 0 & 0 & 0 & 0 & 0 & 0 & 1 \\
 0 & 0 & 1 & 0 & 0 & 0 & 0 \\
 1 & 0 & 0 & 0 & 0 & 0 & 0 \\
 \hline
 0 & 1 & 0 & 0 & 1 & 1 & 0
 \end{array} \right],
 \end{array}$$

wherein points $\mathbf{y}_1, \mathbf{y}_3, \mathbf{y}_4$ in set Y correspond to points $\mathbf{x}_4, \mathbf{x}_3, \mathbf{x}_1$ in set X respectively. The remaining points are all indicated as outliers with a value of 1 in the related outlier row/column such that the two constraints are satisfied. Relatively, the amount of point rejection as outliers is controlled by the third term of the objective function and the weight parameter α adjusts this term.

Since the correspondence matrix C and the transformation function T are discrete and continuous respectively, optimising both criteria simultaneously becomes somewhat difficult. An alternative way to tackle this problem is to not allow the correspondence matrix to approach binary values until convergence of the transformation function to a reasonable solution. Thus, two techniques, Softassign and deterministic annealing, introduced by approaches [24, 58, 122] are used for optimising the main objective function. Conceptually, the Softassign idea is to relax the binary elements in matrix C into continuous values in the interval of $[0 \ 1]$, making a fuzzy correspondence between two

point sets while following row and column constraints. Deterministic annealing [58, 182], on the other hand, adds an entropy function $c_{ij} \log c_{ij}$ to the objective function (7.30) in order to control this fuzziness directly. Therefore, controlled by the temperature parameter τ , the objective function is optimised by a process similar to physical annealing, such that the entropy term forces the correspondence matrix to be more fuzzy at higher temperatures and, as it decreases gradually, the matrix C approaches binary values, where the non-rigid mapping function converges to a reasonably sufficient solution.

Similar to the EM algorithm, the RPM method consists of two steps, an updating process under an annealing scheme to estimate both the correspondence and the non-rigid transformation function. Hence, having two point sets X and Y , the objective function (7.30) is iteratively optimised, namely:

Step 1: Updating with respect to the correspondence matrix for points $i \in \{1, 2, \dots, N\}$ and $j \in \{1, 2, \dots, M\}$:

$$c_{ij} = \frac{1}{\tau} \exp\left(-\frac{\|\mathbf{x}_i - T(\mathbf{y}_j)\|^2}{2\tau}\right) \quad (7.31)$$

and for outliers:

$$c_{N+1,j} = \frac{1}{\tau_0} \exp\left(-\frac{\|\mathbf{x}_{N+1} - T(\mathbf{y}_j)\|^2}{2\tau_0}\right) ; \begin{cases} i = N + 1 \\ j = 1, 2, \dots, M \end{cases} \quad (7.32)$$

$$c_{i,M+1} = \frac{1}{\tau_0} \exp\left(-\frac{\|\mathbf{x}_i - T(\mathbf{y}_{M+1})\|^2}{2\tau_0}\right) ; \begin{cases} i = 1, 2, \dots, N \\ j = M + 1 \end{cases}$$

where parameter τ_0 indicates a large variance for the outlier clusters

centered at \mathbf{x}_{N+1} and \mathbf{y}_{M+1} . To satisfy the constraints, iterated row and column normalisation algorithm is accordingly applied, such that:

$$C_j = \frac{C_j}{\mathbf{1}_{N+1}^T \cdot C_j} , \quad j \in \{1, 2, \dots, M\} \quad (7.33)$$

$$C_i = \frac{C_i}{C_i \cdot \mathbf{1}_{M+1}} , \quad i \in \{1, 2, \dots, N\}.$$

Step 2: Updating with respect to the mapping function. This leads to solving the objective function while eliminating terms independent of T as

$$E(T) = \sum_{i=1}^N \sum_{j=1}^M c_{ij} \|\mathbf{x}_i - T(\mathbf{y}_j)\|^2 + \lambda \|LT\|^2. \quad (7.34)$$

To simplify this least-square problem, it is reformulated as:

$$E(T) = \sum_{j=1}^M \|\mathbf{z}_j - T(\mathbf{y}_j)\|^2 + \lambda \|LT\|^2, \quad (7.35)$$

where

$$\mathbf{z}_i = C_i \cdot \mathbf{1}_M \cdot \mathbf{x}_i , \quad i \in \{1, 2, \dots, N\}. \quad (7.36)$$

Thus, \mathbf{z}_i is represented as the estimated position of any point within set X that corresponds to current point \mathbf{y}_j in the set Y .

As mentioned at the beginning of this section, a TPS method is used to estimate a smoothly interpolated mapping function between the two point sets. This is followed by a smoothness measure (operator L) to control deformations that are too arbitrary . Thus, the TPS function is constrained by its integral of the square of the second derivative as

$$E_{TPS}(T) = \sum_{j=1}^M \|\mathbf{z}_j - T(\mathbf{y}_j)\|^2 + \lambda \iint \left[\left(\frac{\partial^2 T}{\partial x^2} \right)^2 + 2 \left(\frac{\partial^2 T}{\partial x \partial y} \right)^2 + \left(\frac{\partial^2 T}{\partial y^2} \right)^2 \right] dx dy. \quad (7.37)$$

The spatial function T maps each point \mathbf{y}_j to its corresponding \mathbf{z}_j using a rigid transformation matrix (A) combined with a warping coefficient matrix (U) which accounts for the non-rigid deformation part. This is formulated as

$$T_{tps}(\mathbf{y}_j, A, U) = \mathbf{y}_j \cdot A + \phi(\mathbf{y}_j) \cdot U, \quad (7.38)$$

where $\phi_b(\mathbf{y}_a) = \|\mathbf{y}_b - \mathbf{y}_a\|$ is the TPS kernel describing internal structural relationships in a point set. Substituting the TPS function into eqn (7.37) results in the following energy function

$$E_{TPS}(A, U) = \|Z - YA + \Phi U\|^2 + \lambda \text{trace}(U^T \Phi U). \quad (7.39)$$

A QR factorisation technique [165] is then used to decompose the TPS energy function into affine and local non-affine space, as this allows solving the least squares function for rigid and non-rigid parts separately. Thus, QR decomposition of point set Y becomes

$$Y = \begin{bmatrix} Q_1 & | & Q_2 \end{bmatrix} \begin{pmatrix} R \\ 0 \end{pmatrix} \quad (7.40)$$

where Q_1 and Q_2 are orthonormal matrices, and R an upper triangular matrix. Accordingly, eqn (7.39) is then reformulated as:

$$E_{TPS}(A, \gamma) = \|Q_2^T Z - Q_2^T \Phi Q_2 \gamma\|^2 + \|Q_1^T Z - RA - Q_1^T \Phi Q_1 \gamma\|^2 + \lambda \gamma^T Q_2^T \Phi Q_2 \gamma, \quad (7.41)$$

where $U = Q_2\gamma$ and γ is a $(M - 1 - D) \times (D + 1)$ matrix. Minimising the TPS energy function w.r.t. γ and w.r.t. A in turn results in:

$$\hat{U} = Q_2\gamma = Q_2(Q_2^T\Phi Q_2 + \lambda I_{M-D-1})^{-1}Q_2^T Z \quad (7.42)$$

and

$$\hat{A} = R^{-1}(Q_1^T Y - \Phi \hat{U}). \quad (7.43)$$

Hence, the location of a moving points \mathbf{y}_j is updated as

$$\hat{\mathbf{y}}_j = \mathbf{y}_j \cdot A + \Phi \cdot U. \quad (7.44)$$

Therefore, based on an annealing scheme, the RPM algorithm iterates between updating the correspondence and TPS transformation function steps and gradually minimises the temperature parameter (τ) until it drops below a pre-defined threshold.

7.3 Registration Methods for MRI-TRUS

Fusion

The methods used for registration of MRI to TRUS images are categorised into rigid and non-rigid ones, as described in the following sections.

7.3.1 Rigid Registration

One of the earliest pieces of research for MRI-ultrasound rigid fusion was conducted by [78], where six reference points were selected on slices of each image modality and an affine transformation was used for registration. To improve the accuracy, a similar transformation was later used on large sets

of 3D points from US and MRI to register them automatically [124, 172]. In [173], Sheng et al. reconstructed a 3D US image based on axial sweeps of 2D US probe throughout the prostate gland and then registered it manually with MRI before biopsy. During biopsy, the 2D US probe was used to scan the prostate. Spatial tracking of the probe and registration of the MRI coordinate system and the tracking coordinate system enabled a real-time live fusion of US with MRI. Image-based registration was used for motion compensation. Rigid motion compensation was between the reference 3D US and intra-operative 2D US. The accuracy of the system was evaluated using a phantom. Further, this research group used a larger number of MRI and TRUS images to create a statistical model of the prostate for segmentation, and with a similar approach for registration [77].

In [135], Shah et al. presented an open-source library for rigid registration of pre-operative positron emission tomography (PET) and MRI with intra-operative TRUS images during prostate biopsy. To achieve this, an optical tracking system was used for spatial and temporal calibration between TRUS video frames and the optical target (the US probe). Using a landmark-based method, four corresponding points were manually selected to rigidly align PET/MRI with TRUS images. This method was evaluated by preliminary clinical examination of two patients.

Rigid registration only accounts for global transformation, such as rotation and translation, of the prostate images in MRI and TRUS. However, the prostate may undergo local deformations caused by the US probe or patient movement during a surgery. To compensate for these deformations, non-rigid components are used to account for local changes.

7.3.2 Deformable Registration

Moradi et al. proposed two solutions for the MRI-TRUS registration problem [104]. In the first solution, both MRI and TRUS images were manually segmented and triangulated using an open-source 3D slicer software package [119]. The iterative closest point (ICP) was used to find one-to-one correspondence between surface meshes and also to perform an initial alignment. ICP is a popular algorithm for assigning correspondence between two point sets based on proximity [13, 44]. A B-spline non-rigid transformation [127] was then used to register the MRI surface mesh onto the TRUS coordinate space. Finally, the objective function was optimised using the mutual information maximisation approach [95]. In the second solution, with a moderate modification, Moradi et al. added a biomechanical model as a regulariser to smooth the transformation between MRI and TRUS surface meshes. In addition, they used spherical harmonic representation of the prostate surfaces in order to simplify the objective function and estimates the rotational transform only. Based on the experimental results, the second solution outperformed the first one with a slightly smaller target registration error. The second method of Moradi et al. was later improved by Fedorov et al. [49].

Another approach used a surface-to-surface registration method to achieve MRI-TRUS fusion for brachytherapy [99]. In this work, individual points in each modality were represented using a shape-context descriptor, whereby the correspondence between points was obtained by matching these descriptors using the Hungarian algorithm [106]. At the end, a 3D B-spline grid was used to register the corresponding points in both surfaces.

Accordingly, Mitra et al. used a TPS method for co-registration of

the segmented slices between TRUS and MRI [102]. To do this, the corresponding slices between MRI and TRUS were observationally selected and then segmented manually. A set of points were uniformly sampled from the segmented slices. Each sample point from one of the modal image was represented using a shape descriptor that was a vector of log-polar (polar coordinate i.e. r, θ in which the log of r is used) relative distance to the point in the other image. The shape descriptor binned into a histogram that was uniform in log-polar space and used as the shape-context representation of a contour point. The Bhattacharyya distance was then calculated between the shape-context histograms of two shapes to find the point correspondence. In the next stage, a bijective transformation was used to align a pair of fixed and moving binary images.

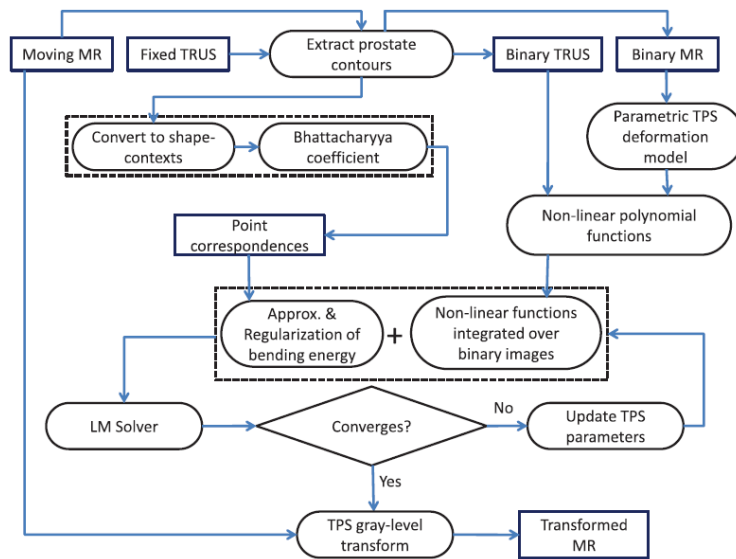


Figure 7.2: “Schema diagram of the proposed registration framework.” [102]

In Sun et al. primary research [147], the local similarity between MRI and US images was measured by using the method of multi-channel modality independent neighbourhood descriptor (MIND) [64]. Both MIND features, obtained from MRIs and TRUS images, were aligned using a proposed

duality-based convex optimisation algorithm. The TRE metric was used to evaluate the accuracy of registration using 41 intrinsic fiducial pairs across all regions of the prostate gland. This method was extensively presented in [146]. Further, Sun et al. proposed a surface-based registration method for image-guided prostate biopsy [143]. The prostate’s surface in each modality was represented by a set of points. These points were sampled from the boundary of the prostate in each segmented slice. A TPS-based registration algorithm was then proposed to transform the prostate surface points in MRI to corresponding points in TRUS. To improve the registration accuracy, Sun et al. extended their previous work by adding extra components for finding a more accurate correspondence between two surfaces [144]. As an initialisation step, both TRUS and MR images were roughly aligned (rigid transformation) using 6 manually identified corresponding points which were apex, left-most, right-most, top-most, bottom-most points of the largest prostate cross-section of axial slices and the urethra at its entrance into the prostate. Both images were resized to the same voxel size. The prostate segmentation was performed manually for each image. To find the corresponding surface points, each pair of TRUS and MR images was re-sliced around a specified rotational axis. This was followed by TPS registration for mapping MRI surface points to their counterparts in TRUS. The summary of this method is shown in Figure 7.3.

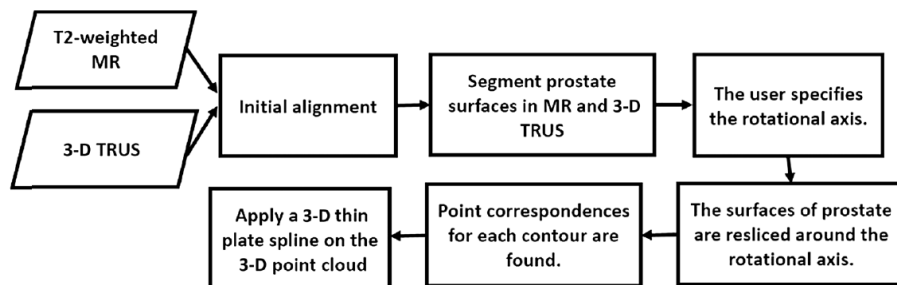


Figure 7.3: “Workflow of landmark-based non-rigid registration.” [144]

Zetting et al. developed a multi-modal fusion system for non-rigid

registration of PET/MRI and US images in application to prostate biopsy [184]. This approach, as an improvement of their earlier work in [135], changed the registration strategy from rigid to elastic such that, first, PET and MR images were intrinsically registered to each other in advance, since they were acquired and reconstructed simultaneously under the same coordinate system. The US image was automatically segmented using the Hough forest approach. Both MRI and TRUS surface models were created using triangulation and meshing techniques. To elastically register the two surface meshes, they used a modified version of the CPD method.

Alternatively, a model-to-image framework was proposed by Hu et al. for a patient-specific MRI-TRUS registration [67, 66]. This method waived the manual segmentation of the prostate in TRUS by propagating a statistical model into TRUS image space and performing an implicit registration using a modified algorithm. The statistical model was created through several steps in advance. At first, the prostate gland, along with its surrounding organs in the MR image, was manually segmented to create a patient-specific finite element mesh. To capture the prostate deformations caused by the US probe, a series of FE analysis was performed to simulate the different orientations and possible positions of the US probe during a surgery. Each simulation resulted in a vector of FE node displacement. Finally, a statistical deformation model (SDM) was constructed by applying PCA to the obtained vectors. Figure 7.4 shows an overview of this method.

Similarly, a model-to-surface based method was proposed by Yi Wang et al., in which the SDM was constructed based on FE analysis and the patient-specific tissue parameters measured from the US elastography [168]. This was followed by integrating the advantages of the MIND similarity measure and the PPM algorithm for achieving a hybrid point-matching

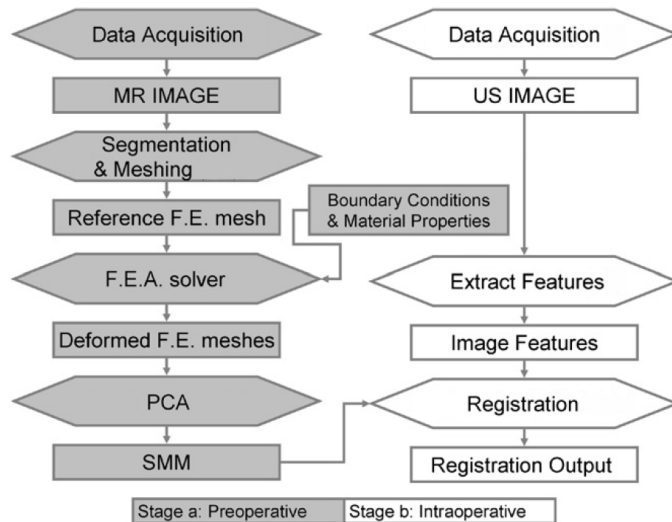


Figure 7.4: “An overview of the registration method. Preoperative processes and data are shaded grey, whereas intra-operative processes and data are not shaded.” [66]

method. The RPM was then guided by the obtained SDM for MRI-TRUS fusion. Further, Onofrey et al. extended the subject-dependent SDM to a generic model by creating the statistical deformation model using a large set of MRI and TRUS images from patients who underwent prostate biopsy [112, 110, 111]. Primarily, each image modality was segmented manually and the prostate surface represented as points within a triangulated mesh. Segmenting all images, the obtained training data was normalised for volume differences and individual subjects were mapped into a common reference template. This was then followed by:

- (i) intra-subject alignment of MRI and TRUS surfaces
- (ii) non-rigid registration of both surfaces with the reference surface
- (iii) normalisation of the deformed surfaces from the previous step.

At the end, a PCA was applied on the remaining distribution of deformations between MRI and TRUS surfaces to keep the significant modes of variation.

Having the SDM created, the RPM algorithm was used for non-rigid registration of new cases, wherein the estimation of the free deformation field was constrained to lie within the SDM search space.

FE techniques have shown to be robust for predicting internal deformation of the prostate [67, 66, 161, 162]. Khallaghi et al. developed an FE-based method to perform a robust MRI-TRUS fusion [81]. This method is known as GMM-FEM, in which a GMM framework is used to establish a probabilistic correspondence between MRI and TRUS surface points, and an FEM is used to regularise the deformation of the prostate. Further, to improve the registration accuracy, Khallaghi et al. employed an additional statistical shape model (SSM) as a geometric prior, enabling partial-to-partial registration of MRI/TRUS images [80]. The SSM was created using a group-wise GMM-based framework in order to be utilised as a bias-free reference model for guiding the registration task [123]. An overview of the SSM-FEM method is shown in Figure 7.5.

Recently, deep learning approaches have been adopted for non-rigid registration of medical images [91, 85, 90, 40]. For multi-modal image fusion, deep learning methods are typically proposed either to learn a similarity metric to govern an iterative optimisation strategy [23, 47, 63] or to directly estimate the parameters of the transformation model using deep regression networks [136, 19, 9, 46]. Although review of these approaches is beyond the scope of this research, the experimental results of MRI-TRUS fusion by some deep learning approaches show the potential of CNNs for improving the accuracy of image-guided prostate intervention in the near future [69, 70, 68, 174, 63].

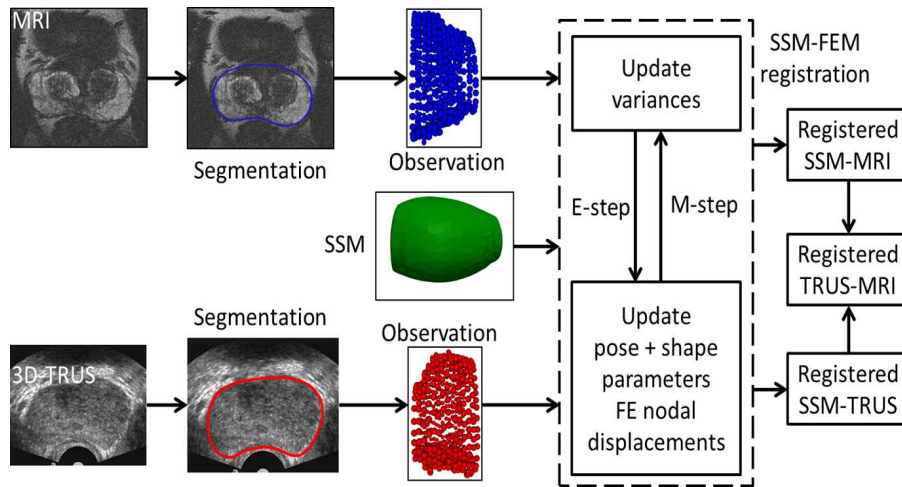


Figure 7.5: “Overview of the MR-TRUS fusion workflow. The pre-operative (MR) image is acquired before the procedure and is segmented to create a surface representation of the anatomy (e.g. the prostate). At the beginning of the procedure, an intra-operative (3D-TRUS) image is acquired and parts of the anatomy (mid-gland) are segmented. SSM-FEM maps both surfaces and their interior to a common intermediate SSM instance. Subsequently, the MRI is registered to the TRUS through this intermediate shape.” [80]

7.4 MRI-TRUS Fusion Challenges and Implications for Current Research

Given the variety of approaches in the literature and currently under development, specifying a single best method of deformable registration for MRI and TRUS remains an open question.

In general, a deformable (as opposed to rigid or global) registration method should specify the relationships between MRI and TRUS images by establishing a spatial correspondence between two surfaces, and applying a non-linear transformation to map individuals surface points from the MRI to their counterparts in the TRUS surface.

Establishing a spatial correspondence is itself a non-trivial task when there is significant uncertainty in the segmented prostate image. For example, the

base and apex of the prostate are difficult regions to identify in the TRUS image and unclear segmentation of these parts causes ambiguity when finding their spatial correspondence in MRI. This ambiguity can later affect the registration performance. In addition, the presence of noise or outliers in either images poses a problem for one-to-one matching of point sets in MRI and TRUS surfaces and manual pre-processing is a cumbersome way to remove them from the point sets.

The transformation function can warp a prostate shape in many directions. In some cases, unrealistic deformations in the shape of the prostate are unavoidable when the deformation field is not constrained precisely. Such non-linear functions are said to be ill-posed, where there is not a unique solution to the problem due to their large search space [142]. Thus, a robust non-rigid registration algorithm which can preserve the prostate topology under such deformations is needed.

A point-matching objective function consists of both correspondence and non-linear transformation terms for optimisation. A unique solution to such a combinatorial optimisation problem is achievable only if one of the terms to be held is fixed. However, it may not be meaningful to solve for the correspondence when the estimated transformation function performs poorly. Thus, the challenge arises when the spatial correspondence and transformation function are to be estimated simultaneously.

This research investigates an automatic surface-based registration method for MRI-TRUS fusion. To achieve this, we address the following objectives for our registration algorithm in the following chapter.

- to develop an automatic algorithm for one-to-one correspondence estimation between MRI and TRUS surface points that mitigates errors caused by arbitrary prostate poses,

- to derive a regularisation model for constraining the non-linear transformation function that incorporate forces to imitate realistic deformations that a prostate may undergo,
- to establish an optimisation strategy to simultaneously estimate both the correspondence and the transformation function under an iterative scheme within an efficient time-frame.

It is expected that incorporating the local topological structure of the prostate shape into a similarity-based matching function can reinforce the accuracy of point correspondence estimation. Preserving the local structures can also help to prevent optimisers being stuck in local minima. Moreover, MRI-TRUS fusion can be further improved by embedding a regulariser into the non-rigid transformation function to filter out undesirable deformation forces from the search space according to an a priori knowledge of the biomechanical states of the prostate. Having both correspondence and transformation problems defined in this manner, a metaheuristic optimisation strategy can then be proposed to approximate a global solution for each term simultaneously using an iterative scheme.

Chapter 8

MRI-TRUS Fusion

Overview

This chapter presents our novel algorithm for performing a robust MRI-TRUS registration under the assumption that each image modality has been already segmented and represented as a 3D point cloud (surface). The goal of the registration is to align and fit the two 3D surfaces while preserving the prostate topological structure under deformations, with a high degree of accuracy. Upon successful registration, locations of targeted body structures in pre-operative MR images can be transformed into intra-operative TRUS images, where this can later provide more accurate guidance in clinical applications of image-guided prostate intervention.

8.1 Proposed Fusion Method

In this research, we present a surface-based algorithm for non-rigid registration of MRI and TRUS images under a unified optimisation framework. An overview of the proposed method is shown in Figure 8.1, where, from left to

right, the first and second chunks indicate MRI and TRUS images along with their segmentations which are provided prior to fusion. Having the surface

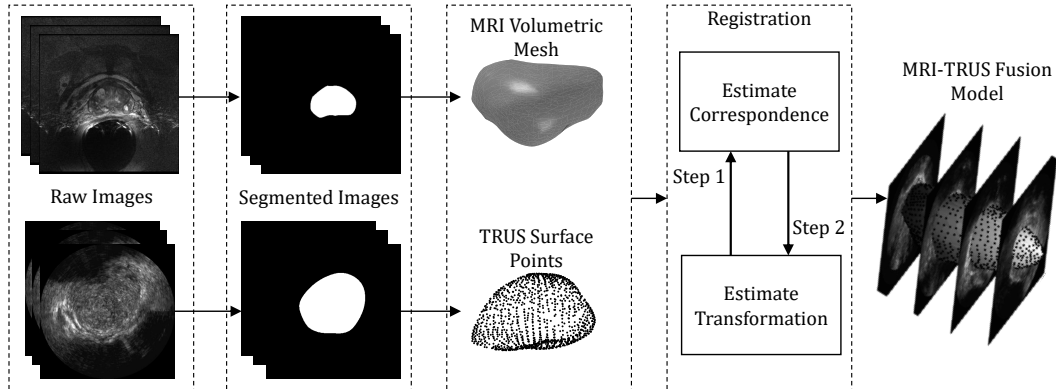


Figure 8.1: The proposed MRI-TRUS fusion workflow.

model and volumetric mesh constructed from the segmented images for TRUS and MRI respectively in advance, the proposed algorithm iterates between two main steps for estimating correspondence and transformation parameters simultaneously until it fulfils the stopping criteria for MRI-TRUS fusion. This is achieved by minimising the energy function ,defined as:

$$\min_{\mathcal{M}, \mathcal{T}} \mathcal{E}(\mathcal{M}, \mathcal{T}) = \sum_{i=1}^N \sum_{j=1}^M \mathcal{M}_{ij} \|\mathbf{x}_i - \mathcal{T}(\mathbf{y}_j)\|^2 + \lambda \mathcal{R}(\mathcal{T}), \quad (8.1)$$

where $\mathbf{x}_i \in X$ and $\mathbf{y}_j \in Y$ represent TRUS and MRI surface points in D dimensions, respectively. $\mathcal{M}_{ij} \in \{0, 1\}$ are elements of a binary matrix indicating one-to-one correspondence between MRI and TRUS surface points. The spatial transformation function is denoted by \mathcal{T} and is regularised by the $\mathcal{R}(\mathcal{T})$ term. The parameter λ controls the magnitude of the regulariser. The energy function (8.1) is then minimised with respect to correspondence \mathcal{M} and transformation \mathcal{T} using an iterative optimisation scheme.

In order to simplify the description of our method, it is divided into three components. namely, the correspondence estimation, the transformation

(including the regularisation part), and the optimisation. Each component is then discussed separately throughout following sections.

8.1.1 Correspondence Estimation

We propose a distance-based metric for correspondence estimation by considering the spatial relationship between the topological structure of points in MRI and TRUS models. The distance-based metric was adopted from an approach in [180]. This metric measures both global and local differences between points and combines them to form a cost matrix that gives the distance between all points in X and Y. The cost matrix is minimised using a linear assignment algorithm to establish a one-to-one correspondence between MRI and TRUS surface points. Estimation of the correspondence matrix is step 1 in our algorithm and it is determined by undertaking the following instructions.

8.1.1.1 Global Topological Structure

Global topological structure (GTS), as shown in Figure 8.2, measures the squared Euclidean distance of point \mathbf{x}_i in a set from individual points \mathbf{y}_j in the other set as:

$$\mathcal{G}_{ij} = \|\mathbf{x}_i - \mathbf{y}_j\|^2 \quad ; \text{ for } \begin{cases} i = 1, 2, \dots, N \\ j = 1, 2, \dots, M \end{cases} . \quad (8.2)$$

The distance matrix \mathcal{G} indicates the global difference in topological structure between MRI and TRUS surface points. If \mathcal{G} is interpreted as a global cost matrix, then minimising it by a linear assignment solution results in a correspondence based on the global difference in topological structure.

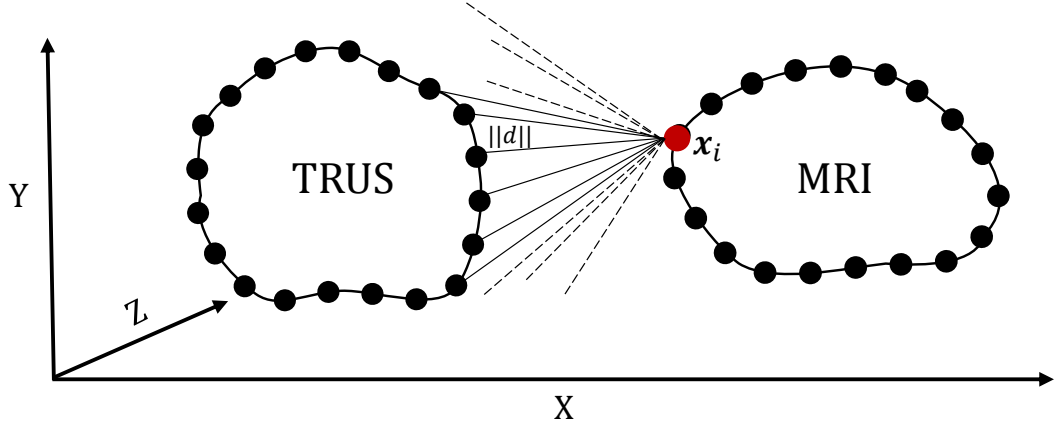


Figure 8.2: Measuring GTS for the current point $\mathbf{x}_i \in X$.

8.1.1.2 Local Topological Structure

In addition to GTS, local topological structure (LTS) is designed to capture local changes between two surfaces. For this, the corresponding clusters of points in each surface, represented by their centres of mass and consisting of K neighbouring points, form local segments. The local segments for TRUS and MRI are denoted by $L_k(\mathbf{x}_i)$ and $L_k(\mathbf{y}_j)$ respectively, where \mathbf{x}_i and \mathbf{y}_j indicate the the centre points. Having two sets of local segments computed for both MRI and TRUS surfaces, the LTS is then measured by the sum of squared Euclidean distances between these two, such that:

$$\mathcal{L}_{ij} = \sum_{k=1}^K \left\| L_k(\mathbf{x}_i) - f(L_k(\mathbf{y}_j) ; \mathbf{x}_i) \right\|^2, \quad (8.3)$$

where:

$$f(L_k(\mathbf{y}_j) ; \mathbf{x}_i) = L_k(\mathbf{y}_j) + (\mathbf{x}_i - \mathbf{y}_j). \quad (8.4)$$

Matrix \mathcal{L} is denoted the LTS distance measure. The transformation function f in eqn (8.4) is used to translate the current local segment in the MRI surface to its counterpart in TRUS based on the centre of the mass. A pictorial example of this is shown in Figure 8.3. Therefore, if \mathcal{L} is interpreted as the

local cost matrix, then minimising it by a linear assignment solution results in a correspondence based on local differences in topological structure.

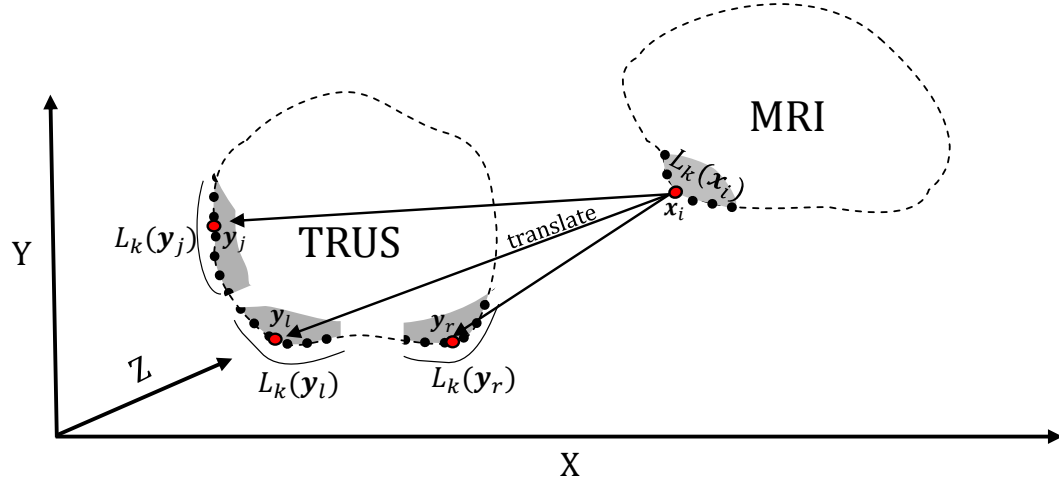


Figure 8.3: An example of local topological structure (LTS) measurement, where neighbouring points $K = 5$ and $\{y_j, y_l, y_r\} \in Y$.

Since local segments are principally constructed based on centre points and their neighbours, specifying the number of neighbouring points plays a key role in measuring local similarities of MRI and TRUS surfaces, preserving the topological structure of the prostate, and mitigating the impact of outliers on the performance of registration algorithm. This also can empower the LTS measure to substantially handle the prostate's arbitrary poses by minimising the rotation angle between the common local similarities in the two surfaces.

8.1.1.3 Combined GTS and LTS Differences

Once GTS and LTS are computed, they are unified into a single form as:

$$\mathcal{C} = \mathcal{G} + \alpha\mathcal{L}, \quad (8.5)$$

where \mathcal{C} is a cost matrix that consists of both global and local topological structure differences (GLTSD). The weighting parameter α establishes a

trade-off between global and local costs in \mathcal{C} , where its large value is accounted for by minimising matrix \mathcal{C} with respect to LTS. In contrast, a small value of α minimises the \mathcal{C} with respect to GTS. Hence, such a combination yields a flexible way for the \mathcal{C} matrix to estimate the correspondence by minimising the global or local structural differences between MRI and TRUS surface points.

Posed in this manner, the correspondence for the given list of points in the MRI surface at each iteration (step 1) is estimated by minimising the total GLTSD-based cost function as:

$$\mathcal{E}(\mathcal{M}) = \sum_{i=1}^N \sum_{j=1}^M \mathcal{M}_{ij} \mathcal{C}_{ij}, \quad (8.6)$$

where matrix \mathcal{M} establishes a one-to-one correspondence from TRUS (X) to MRI (Y) surface points and satisfies the condition $\sum_{j=1}^M \mathcal{M}_{ij} = 1$ for the individual points in the set X with $\mathcal{M}_{ij} \in \{0, 1\}$. As denoted, each element c_{ij} in the matrix \mathcal{C} indicates costs from \mathbf{x}_i to \mathbf{y}_j and contains the weighting parameter α . Thus, the optimisation process relies merely on α which is controlled by an annealing rate, gradually changing the minimisation of $\mathcal{E}(\mathcal{M})$ from the LTS distance to the GTS distance.

This way, the correspondence matrix \mathcal{M} is estimated by minimising the total cost using a linear assignment solution by using the well-known Hungarian algorithm [86], where it conceptually performs a sets of row and column operations to find the minimum value of each row (or column) and then to subtract this from the individual elements of the row (or column) which owns that minimum value. This process is repeated for all rows and columns until each point in the set X is assigned to its corresponding point in the set Y with the lowest cost. The Jonker–Volgenant algorithm is one of the most popular versions of the Hungarian algorithm which solves the linear

assignment problem based on the shortest augmenting path [74]. Since the original algorithm was designed to work with integer-based square matrices, each element in the GLTSD-based cost matrix is rescaled by a large number $\{R \gg 10^4 \mid c_{ij} \times R\}$ and then is rounded accordingly. For non-square matrices (this may happen when the number of points in a set is not the same as in the other set due to the presence of outliers), dummy entries are assigned to the cost matrix such that it is converted to a square type matrix. This will not affect the total cost and the original Jonker–Volgenant algorithm can be used to solve the assignment problem with the best solution [101]. In this manner, the algorithm guarantees to output a binary correspondence for the matrix \mathcal{M} . Hence, the new corresponding points are updated as:

$$\mathbf{z}_j = \sum_{i=1}^N \mathcal{M}_{ij} \mathbf{x}_i, \quad (8.7)$$

where \mathbf{z}_j is the estimated point in the set X that corresponds to the current transformed point $\mathcal{T}(\mathbf{y}_j)$ in the set Y . To update the correspondence in next iterations, GTS and LTS are determined for each \mathbf{z}_i and $\mathcal{T}(\mathbf{y}_j)$. Since LTS is measured from small local segments $L_k(\mathbf{z}_i)$ and $L_k(\mathcal{T}(\mathbf{y}_j))$ with the determined neighbouring points which are fixed during the transformation step, minimising it preserves the topological structure of MRI surface points under deformation forces.

8.1.2 Transformation Estimation

After establishing correspondence, the MRI points are non-rigidly registered to their counterparts on the TRUS surface by the following transformation:

$$\mathcal{T}(\mathbf{y}_j) = \mathcal{T}(\mathbf{y}_j, \mathcal{V}) = \mathbf{y}_j + \mathcal{V}_j(\mathbf{u}), \quad (8.8)$$

where \mathcal{V} is a displacement function with vector \mathbf{u} , estimating the shortest distance from \mathbf{y}_j to its corresponding point in the other set. Thus, by estimation of the transformation function \mathcal{T} through \mathcal{V} , MRI surface points can be non-rigidly registered to TRUS surface points (step 2), while the correspondence has been determined beforehand (step 1). This procedure then leads to an MRI-TRUS fusion. However, using \mathcal{T} alone may lead the MRI-TRUS fusion to become an ill-posed problem [154, 155], since there is not a unique way of mapping points from MRI to TRUS surface points due to the intrinsic non-linearity of the transformation function. As such, the prostate volume may deform in an unrealistic way and cause an inaccuracy in identification of distinct anatomical structures within the prostate. Thus, the transformation function must be constrained to only produce deformation forces which are meaningful from the prostate point of view.

In this research, a finite element model (FEM) is incorporated into the regularisation term for constraining \mathcal{T} , as the deformation of the prostate during biopsy or brachytherapy is known to be biomechanical in nature [104, 130, 18]. In fact, the FEM constrains the deformation forces produced by the mapping function according to the prior biomechanical states of the prostate for a specific patient. Conceptually, in the FEM, the prostate volume is modelled by a set of finite elements that are interconnected at nodes. Each node has a nodal displacement in the form of a vector which includes rotation, scaling and translation. Thus, moving of nodes will drag the related elements along in a certain way such that this movement can deform the volumetric shape based on physical properties of the prostate which are affected by the magnitude of the deformation force. The physical properties are described by Young's modulus and Poisson's ratio, where the former controls stiffness and the latter specifies how much the prostate can be compressed or expanded

perpendicular to the direction of the deformation force. In our method, the MRI surface is used by a FE-mesh tool called TetGen to generate the FEM volumetric mesh, where the generated exterior nodes correspond to MRI surface points and the remaining internals are appended to the end of the nodal index list [139]. Therefore, \mathcal{V} in eqn (8.8) is defined as a function of FEM nodal displacements $\{\mathbf{u}_a \in U \mid a = 1, 2, \dots, A\}$, such that:

$$\mathcal{V}_j(\mathbf{u}) = \Phi_j \mathbf{u} \ ; \ \Phi = \begin{bmatrix} I_{DM \times DM} & 0 \\ 0 & 0 \end{bmatrix}, \quad (8.9)$$

where the concatenated vector \mathbf{u} is created from FEM nodal displacements in matrix U , such that $\mathbf{u} = \text{vec}(U) = [u_{11}, u_{12}, u_{13}, \dots, u_{A1}, u_{A2}, u_{A3}]^T$. Φ is a sparse matrix relating MRI surface points to their corresponding nodes in the volumetric mesh. If such a correspondence cannot be established between surface points and the generated FEM nodes, Φ is directly derived from the shape function of the FEM elements. Consequently, for spatial transformation (which is now a function of nodal displacement vector) to move points smoothly and coherently, it is constrained by the regularisation term as:

$$\mathcal{R}(\mathcal{T}) = \mathbf{u}^T \Psi \mathbf{u}, \quad (8.10)$$

where $\mathcal{R}(\mathcal{T})$ penalises the total energy function in eqn (8.1) based on the volumetric strain energy of the FEM derived from a linear stress–strain relationship, with linear stiffness component Ψ [80, 16]. The sparse matrix Ψ is created based on the physical properties of the prostate which is parametrised by Young’s modulus E and Poisson’s ratio γ . These are initialised as inputs to our algorithm. Estimation of the transformation function is step 2 in our algorithm.

Estimating correspondence and transformation components in (8.7) and (8.8) respectively, and adding the penalty term (8.10) to the total energy function in eqn (8.1), it is reformulated as:

$$\begin{aligned}\mathcal{E}(\mathbf{u}) &= \sum_{j=1}^M \|\mathbf{z}_j - (\mathbf{y}_j + \mathcal{V}_j(\mathbf{u}))\|^2 + \lambda \mathbf{u}^T \Psi \mathbf{u} \\ &= \|\vec{Z} - \vec{Y} - \Phi \mathbf{u}\|^2 + \lambda \mathbf{u}^T \Psi \mathbf{u}\end{aligned}\tag{8.11}$$

where λ acts as a weighting parameter and regularises the non-rigid deformations of vector \mathbf{u} based on the Tikhonov regularisation framework [164]. Similar to the parameter α in eqn (8.5), λ is controlled by the same annealing scheme. To minimise $\mathcal{E}(\mathbf{u})$, eqn (8.11) is differentiated with respect to FEM nodal displacement vector \mathbf{u} as:

$$(\Phi^T \Phi + \lambda \Psi) \mathbf{u} = \Phi^T (\vec{Z} - \vec{Y}),\tag{8.12}$$

and as a result \mathbf{u} is given by:

$$\mathbf{u} = (\Phi^T \Phi + \lambda \Psi)^{-1} \Phi^T (\vec{Z} - \vec{Y}).\tag{8.13}$$

Having \mathbf{u} computed, the new positions of point set Y are updated according to eqns (8.8) and (8.9). This process is repeated all through again from step 1 (section 8.1.1) until the algorithm fulfils the stopping criteria.

8.1.3 Optimisation Strategy

To minimise the total energy function given by eqn (8.1), a single framework optimisation strategy based on a variant of simulated annealing is used to estimate the correspondence matrix \mathcal{M} and the spatial transformation \mathcal{T} simultaneously. Simulated annealing approximates the global optimum of

a given function based on its heuristic and prevents getting stuck in local minima [25, 82]. Such a capability makes it an excellent candidate for difficult combinatorial optimisation problems (like ours), especially when dealing with a large discrete search space [24, 72, 187]. Conceptually, under an annealing scheme, the minimisation process often begins with an initial high temperature t and ends when parameter t reaches its specified lowest amount. This is done by using an exponential annealing schedule, namely:

$$t = t \times \rho \tag{8.14}$$

where the starting temperature t is lowered gradually by the annealing rate ρ which is a constant with a value of $0 < \rho < 1$. Thus, exploiting the same annealing scheme, parameters α and λ in eqns (8.5) and (8.13) are in turn reduced gradually, where this enables our algorithm to iteratively minimise the GLTSD-based cost matrix from local to global, and to transform the FEM nodal displacement from rigid to non-rigid, respectively.

Overall, three parameters t , α and λ are assigned large values right before starting the optimisation process. Initialised in this manner, the registration algorithm starts with a high temperature to estimate the correspondence matrix \mathcal{M} with emphasis on searching for local similarities between MRI (X) and TRUS (Y) surface points, where this preserves the topological structure of the warping points in the set X and handles possible outliers and arbitrary rotations. Meanwhile, a large λ strongly penalises the magnitude of the forces produced by the current estimated transformation \mathcal{T} to avoid an unrealistic deformation in the shape of the prostate, hence emphasising the rigidity at early stages to preserve the topological structure. Iterating the algorithm simultaneously, both α and λ become smaller as temperature decreases such

that at lower temperatures, the concentration from local similarities shifts to global for estimating \mathcal{M} and the registration algorithm performs more non-rigidly for estimating \mathcal{T} as well. The process stops when the temperature reaches t_f which is its specified lowest amount.

8.1.4 Proposed GLTSD-FEM Algorithm

We refer to our algorithm as GLTSD-FEM, since it uses GLTSD cost matrix and FEM nodal displacement components to estimate correspondence and transformation, respectively. The pseudo code of the GLTSD-FEM algorithm is shown in Algorithm 2.

<pre> Data: Surface points X,Y • Initialisation: $t, \rho, t_f, \alpha, \lambda, E, \gamma$; • Set K neighbouring points and determine $L_k(\mathbf{x})$ and $L_k(\mathbf{y})$; • Compute FEM volumetric mesh and $\Phi, \Psi(\gamma, E)$ matrices; while $t > t_f$ do Step 1: Estimate the current correspondence matrix ; begin • Compute \mathcal{G} and $\mathcal{L} \rightarrow (8.2)$ and (8.3); • $\mathcal{C} = \mathcal{G} + \alpha\mathcal{L}$; • Minimise $\mathcal{E}(\mathcal{M})$ in (8.6); • $Z = \mathcal{M}^T X \rightarrow (8.7)$ end Step 2: Estimate FEM displacement vector ; begin • $\mathbf{u} = (\Phi^T \Phi + \lambda \Psi)^{-1} \Phi^T (\vec{Z} - \vec{Y})$; • $\mathcal{T}(Y, \mathcal{V}) = Y + \Phi \mathbf{u} \rightarrow (8.8)$ and (8.9); end $t \leftarrow t \times \rho$; $\alpha \leftarrow \alpha \times \rho$; $\lambda \leftarrow \lambda \times \rho$; end </pre>
--

Algorithm 2: The proposed GLTSD-FEM algorithm

As seen from the algorithm, MRI surface points X and TRUS surface points Y are the main inputs to our algorithm. Parameters t and t_f are initial

and final temperature parameters, followed by the annealing rate ρ , weighting parameter α which controls the balance between local and global cost, and λ which does the same between rigid and non-rigid point mapping. Young’s modulus E and Poisson’s ratio γ , as constant values, are inputted to build the linear stiffness matrix Ψ which is used by FEM [81]. The value of K specifies how many neighbouring points should be included in the local segments for point sets X and Y . This is followed by creating the FEM volumetric mesh along with the interpolation matrix Φ and stiffness matrix Ψ . Having set all parameters, under a deterministic annealing scheme, the correspondence matrix \mathcal{M} and the transformation function \mathcal{T} are simultaneously updated in step 1 and step 2 in turn. In between, at each temperature, matrix \mathcal{M} is updated with the solution obtained from the previous iteration. This prevents \mathcal{T} from immature convergence to local minima due to the inter-dependencies that exists between the mapping function and correspondence matrix, and as a result, the registration algorithm is encouraged to explore the search space of the mapping function for a good approximation to global minima. Plugging the estimated mapping function back in to the total energy function and minimising this time with respect to the correspondence matrix reinforce the total accuracy of the algorithm. The GLTSD-FEM reduces t , α and λ at the end of each iteration until it reaches the final temperature t_f .

8.2 Experimental Results

After implementation, we evaluated the performance of the GLTSD-FEM registration algorithm on real clinical data using pairs of MR and TRUS image sets from patients who underwent a prostate biopsy examination. These images were manually segmented, so as not to propagate potential errors

resulting from automatic segmentation. This section discusses the image data in Section 8.2.1, the algorithm configuration and parameter initialisation in Section 8.2.2, and the qualitative and quantitative results given by the GLTSD-FEM algorithm in Section 8.2.3.

8.2.1 Data

We evaluated the performance of our GLTSD-FEM registration algorithm on the clinical data of patients who underwent a prostate biopsy examination. The dataset consists of 38 pairs of MRI and TRUS images which had been manually segmented. This was originally collected by the Robarts Research Institute at the University of Western Ontario in Canada and used with permission. T2-weighted MRIs were mainly obtained in a body coil, where a whole-body 3.0 T Excite 12.0 MRI system (GEHC, Milwaukee, WI, USA) was used to create 3D Axial images with dimensions of $512 \times 512 \times 36$ and voxel size of $0.27 \times 0.27 \times 2.2 \text{ mm}^3$. Mechanically scanned 3D TRUS images were acquired using a Philips HDI-5000 US scanner with a Philips end-firing C9-5 transducer (Philips, Bothell, WA, USA) [12]. This resulted in images having dimensions of $448 \times 448 \times 350$ and voxel size of $0.19 \times 0.19 \times 0.19 \text{ mm}^3$. In addition to these data, 5 sets of MRI and TRUS images of varying dimensions were provided by the Alfred Hospital in Melbourne. Each segmented image was formatted as a 3D polygon using the Visualisation Toolkit (VTK) [132]. We used vertices of these polygons as: MRI (set Y) and TRUS (set X) surface points. Each MRI polygon was input to TetGen [139] to automatically create a tetrahedral volumetric mesh for the FEM component of our algorithm.

8.2.2 Parameter Settings of GLTSD-FEM Algorithm

The main processing of the GLTSD-FEM algorithm was implemented in MATLAB. The original Jonker–Volgenant algorithm, TetGen and a finite element model library were available in C++ and were compiled using the MATLAB MEX function. To run the program, the following parameters of the GLTSD-FEM algorithm were first tuned, based on a set of experiments to find the optimal value of each one. The Robarts image dataset was used for tuning these hyperparameters. These are now discussed in turn:

- *Annealing temperatures*: The starting temperature t is initialised at the value of the variance between the two point sets. t is gradually reduced by the annealing rate $\rho = 0.8$ until it reaches the final temperature t_f (stopping criterion), where t_f is determined as the average of the squared distance between the neighbouring points in the MRI set multiplied by $1/8$. These three parameters were chosen to give the registration algorithm adequate time to explore the search space until it converged to a reasonable solution.
- *Quantity of neighbouring points*: The parameter k was chosen based on the minimum number of points required to discern local structures from each other. For example, it is necessary to have at least four neighbouring points to discern a cross (formed by four neighbouring points) from a corner (formed by two neighbouring points). Thus, the value of K is set as 5 throughout our experiment as default.
- *Weighting parameter in the cost matrix*: To preserve the local topological structures at the start of correspondence estimation, the initial value of the weighting parameter α is set to a moderately large amount, equal to

the value of $k^{4.15}$ for $k = 5$. α is gradually lowered as a function of the annealing rate ρ .

- *Regularisation parameter:* To preserve the prostate’s topological structure at the early stages of estimating transformation, λ is assigned a large value, equal to the number of points (M) divided by 0.8 to constrain the magnitude of the forces produced by the current mapping function in order to perform mainly rigid registration. α is then reduced by ρ at lower temperatures to allow for performing non-rigid registration.

8.2.3 Evaluation of GLTSD-FEM Algorithm

The GLTSD-FEM algorithm was evaluated and compared with the modified rigid and affine registration algorithms [107]. It was also compared with state-of-the-art approaches: CPD by [107] and GMM-FEM by [81], since these algorithms have a similar workflow to our GLTSD-FEM algorithm. The workflow of the 3 algorithms consists of estimating two components: correspondence and transformation, using an iterative optimisation algorithm. CPD and GMM-FEM use a fuzzy approach to finding correspondence between surfaces based on global structure whereas the GLTSD-FEM uses binary global-local topological structure to establish correspondence. In the following section, it will be shown that using local structures improves the accuracy of correspondence. Finite element modelling is used by GMM-FEM and our GLTSD-FEM for transforming the surface model created from MRI to that created from TRUS. By contrast CPD uses a Gaussian kernel-based function for point mapping between the surfaces. Experimental results will show that using the finite element model as a physical prior to guide deformation improves the accuracy of co-registration over the Gaussian kernel approach.

All 3 three algorithms were performed under the same conditions and with the same datasets.

8.2.3.1 Qualitative Registration Results

Figure 8.4 shows an example of qualitative results for 5 registration algorithms (including ours) on an image dataset of a patient who underwent prostate biopsy.

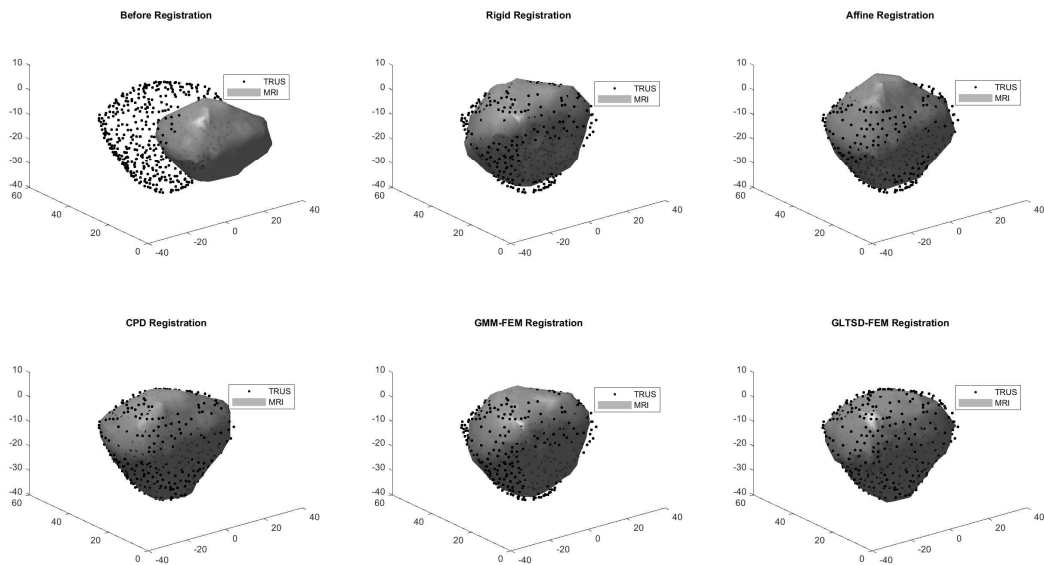


Figure 8.4: Qualitative comparison of surface matching given by 5 registration algorithms. The first row, from left to right, shows results before registration, followed by Rigid and Affine algorithms, the second row shows results of CPD, GMM-FEM and our GLTSD-FEM method.

As seen in this figure, both rigid and affine algorithms fail to transform the whole MRI surface mesh into all of the TRUS surface points due to global deformations within the prostate shape. Our GLTSD-FEM algorithm was found to be more robust against these deformations compared with the other four methods. This is mainly because the GLTSD component of our objective function compensates for these changes by penalising the cost matrix \mathcal{C} for strong deformation forces applied to the prostate surface model.

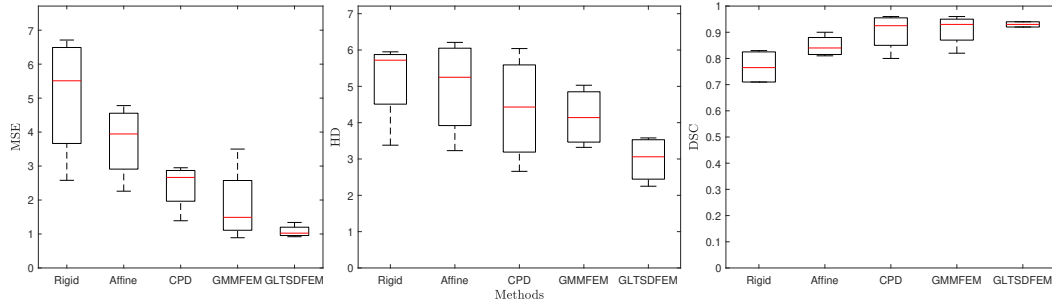


Figure 8.5: Comparison of 5 registration algorithms based on MSE, HD and DSC metrics using the Robarts image dataset for MRI-TRUS fusion. The boxplots show the median, 25th and 75th percentiles, minima and maxima.

Table 8.1: Comparison of 5 registration algorithms showing mean and standard deviation of MSE, HD, and DSC metrics from the Robarts image dataset.

Method	MSE	HD	DSC
Rigid	5.8 ± 1.86	5.19 ± 1.21	0.77 ± 0.06
Affine	3.33 ± 1.1	4.99 ± 1.35	0.85 ± 0.04
CPD	2.42 ± 0.7	4.39 ± 1.49	0.9 ± 0.07
GMM-FEM	1.84 ± 1.5	4.15 ± 0.82	0.91 ± 0.06
GLTSD-FEM	1.08 ± 0.34	2.99 ± 0.64	0.93 ± 0.01

8.2.3.2 Quantitative Registration Results

To measure the correspondence between MRI and TRUS surface points, the mean squared error (MSE) and HD metrics were used to quantify the error. To measure the quality of volumetric overlap, the registered MRI surface was first converted and resampled into a 3D binary map, following the same voxel resolution and image dimensions as the TRUS data. The DSC metric was then used to measure the accuracy of overlap between TRUS and the registered MRI binary slices. The quantitative results for the five registration algorithms on all 38 image sets from the Robarts facility are shown in Figure 8.5 and Table 8.1.

The GLTSD-FEM algorithm outperformed the Rigid, Affine, CPD and GMM-FEM approaches, having average values of 1.08, 2.99 and 0.93 for

the MSE, HD, and DSC metrics respectively. The GLTSD-FEM algorithm also has the smallest standard deviations across three metrics, showing its consistent accuracy over all 38 cases. Furthermore, since both GMM-FEM and GLTSD-FEM use the identical methods for estimating the transformation, compared to CPD they achieved lower MSE and HD, and higher DSC. This demonstrates the advantage of using a finite element model as a physical prior for constraining the estimated transformation over a kernel-based method.

8.2.3.3 Validation of Proposed MRI-TRUS Fusion Method

To validate the MRI-TRUS image fusion obtained by our method, we used distinct anatomical points (DAPs) contain in three image datasets prepared by Fedorov et. al, available on the public domain¹, along with another additional DAPs from the source work² of Khallaghi et. al in [81]. The corresponding DAPs in TRUS and MR images were marked up by an experienced clinical specialist (for example, a radiologist) as ground truth information prior to fusion. The DAPs were mainly selected at urethral entry points at the base and apex of the prostate gland. Subject to their visibility on both images, cysts, calcifications, and verumontanum were also used as DAPs. Altogether, the collected DAPs included 14 anatomical landmarks distributed throughout the 4 prostate glands. Once the GLTSD-FEM algorithm completed the registration task, the L_2 distance between the corresponding DAPs was calculated to quantify the targeted registration error (TRE). The TRE results are shown in Figure 8.6 for all methods.

The Rigid, Affine, and GMM-FEM algorithms gave a TRE of approximately 2.5 mm on average, with CPD having the greatest TRE of approximately 3.8 mm on average. The GLTSD-FEM had the lowest TRE of

¹<http://doi.org/10.5281/zenodo.16396>

²<https://github.com/siavashk/GMM-FEM>

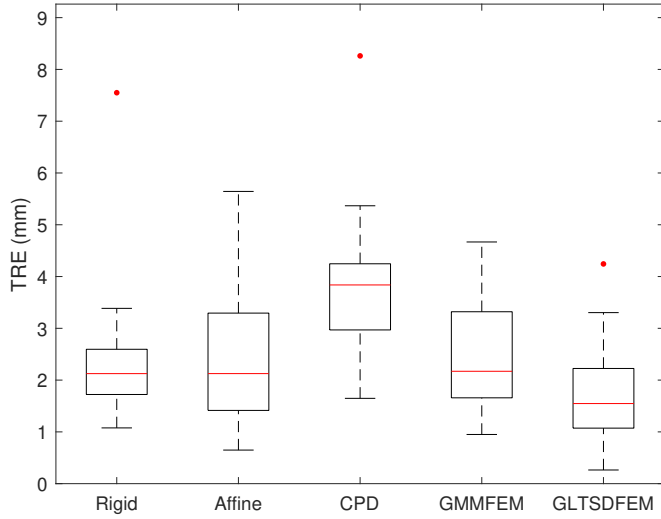


Figure 8.6: Comparison of targeted registration error (TRE) on 4 datasets for all registration methods. The boxplot shows the median, 25th and 75th percentiles, extremes, and outliers.

approximately 1.8 mm on average over the 14 DAPs, indicating the algorithm’s robustness for MRI-TRUS fusion under deformations of the prostate. Table 8.2 provides a detailed comparison of the TRE result for each method. The homologous anatomical landmarks are classified into separate groups as UB = urethra entry point at base, UA = urethra entry points at apex, VM = verumontanum, CT = cyst and CL = calcification. Based on the specified

Table 8.2: TRE comparison of five methods based on mean and standard deviation of 14 DAPs. DAPs were categorised as UB = urethra entry at base, UA = urethra entry point at apex, VM = verumontanum, CT = cyst and CL = calcification.

DAPs (#)	Rigid	Affine	CPD	GMM-FEM	GLTSD-FEM
UB (3)	3.95±3.13	2.64±2.61	4.10±0.14	3.64 ±1.39	1.32±0.27
UA (4)	1.99±0.54	3.38±1.48	4.48±2.75	2.94±0.86	2.25±1.4
VM (3)	1.92±0.51	2.81±1.2	3.54±0.5	2.29±0.93	1.75±0.76
CT (2)	1.71±0.27	1.32±0.95	2.79±0.94	1.42±0.67	1.39±0.81
CL (2)	2.23±1.63	2.21±1.52	2.99±0.38	1.53±0.63	1.59±1.88
All (14)	2.5±1.58	2.54±1.5	3.86±1.58	2.47±1.15	1.8±1.09

number of DAPs per anatomical landmark, the GLTSD-FEM achieved the lowest TRE for all categories except at UA which is slightly higher compared to the Rigid method. This exception may be related to the deformation of the prostate based on a slightly weak estimation of the corresponding points at the apex region of the prostate. Note that both UB and UA are challenging regions for registration due to their locations at the distal and proximal ends of the prostate, where they are associated with neighbouring organs. This vicinity sometimes causes ambiguity in distinguishing a true corresponding point from an outlier. It is worth noting that although the Rigid algorithm achieved a slightly lower TRE at UA, it resulted in a large error at the UB in comparison with the GLTSD-FEM method, which achieved the lowest TRE at the UB among all methods. From this, we may infer that the Rigid method, in some cases, fails to reduce the error between the 3D TRUS and MRI models at the apex or base of the prostate significantly, whereas our method remains consistent in reducing error over all anatomical landmarks. Figure 8.7 shows qualitative TRE from the GLTSD-FEM algorithm for each anatomical landmark.

Based on the qualitative fusion results, and despite large deformations in the MRIs due to the use of an endorectal coil for imaging, the GLTSD-FEM algorithm can consistently transform the DAPs from the MRI onto the TRUS images with minimal uncertainty.

8.3 Analysis and Discussion

The correspondence and the deformation forces estimated by the GLTSD-FEM are to some degree affected by the algorithm's initial parameters. To analyse the influence of each parameter on the registration's performance based on

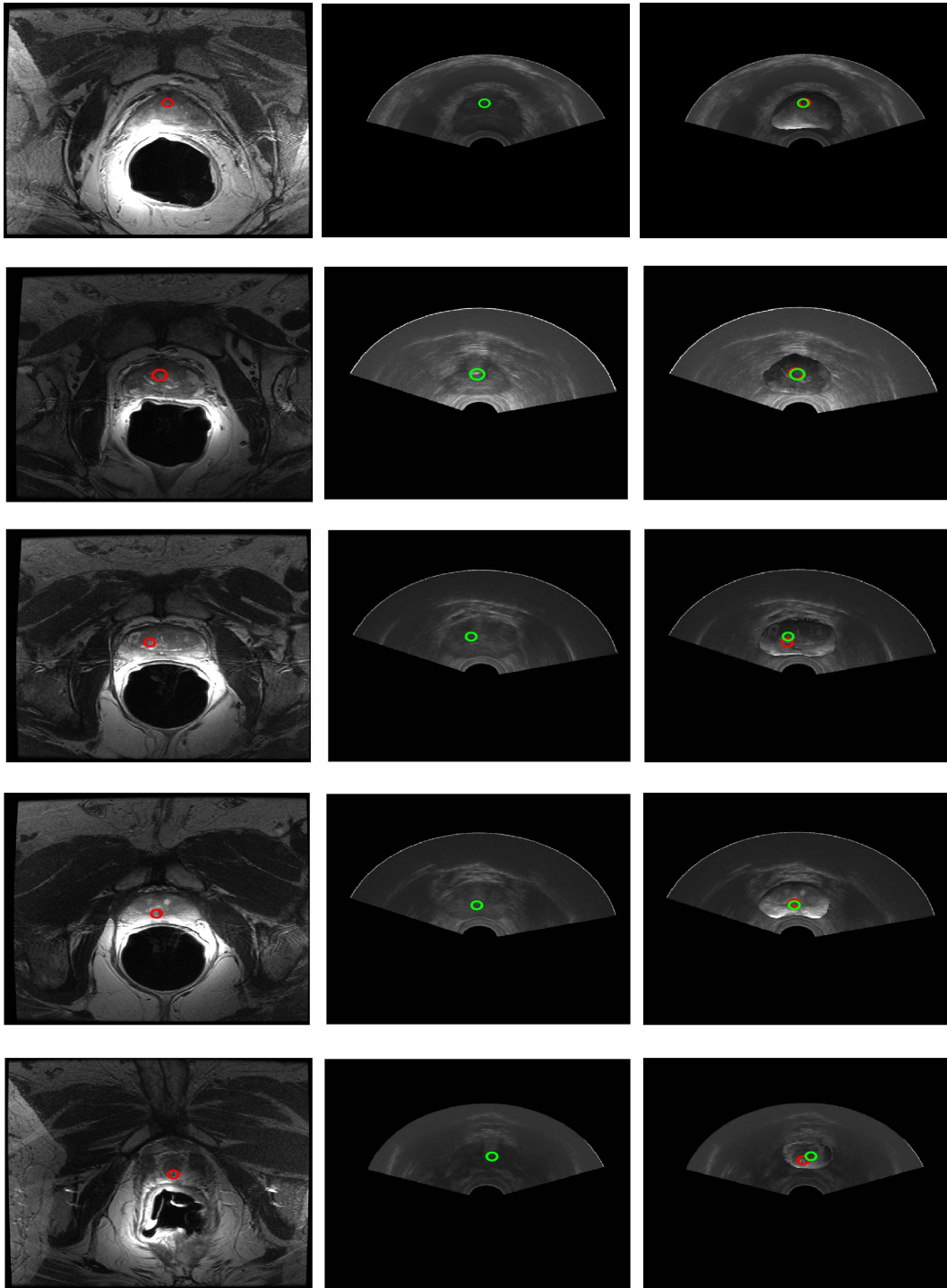


Figure 8.7: Qualitative TRE given by GLTSD-FEM algorithm for individual anatomical landmarks. From left, the first and second columns illustrate MRI and TRUS images by their annotated DAPs before registration, respectively. The right column shows fusion results by GLTSD-FEM for UB, CL, CT, VM and UA from top to bottom, respectively.

an empirical examination, the GLTSD-FEM algorithm was executed over perturbations of individual parameters and the resulting registration errors for each of which were recorded accordingly. Figure 8.8 shows the average registration error given by the GLTSD-FEM algorithm for a range of values allocated to each parameter.

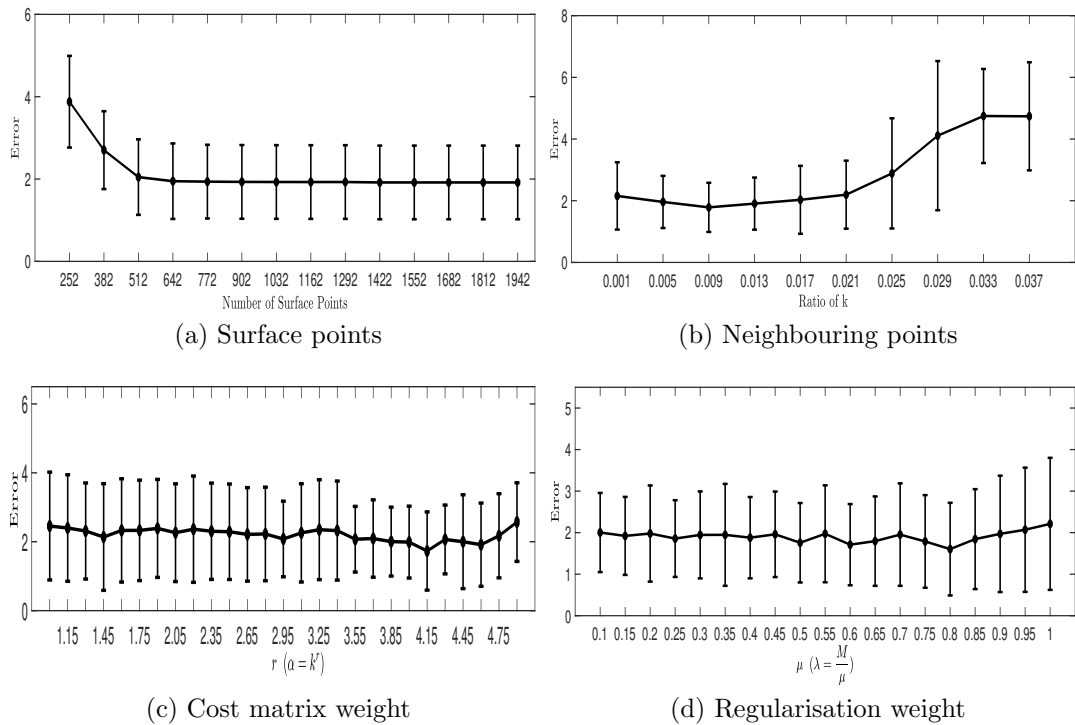


Figure 8.8: Influence of parameters of GLTSD-FEM algorithm on registration performance. The vertical bar indicates the standard deviation of the averaged errors.

The number of surface points is one of the parameters that affects the scheme for initial correspondence establishment and mesh creation for the finite element model. In Figure 8.8a, the average registration error is shown for MRI-TRUS fusion of image sets (including the DAPs) based on specifying varying numbers of surface points. The GLTSD-FEM algorithm consistently returned almost the same minimum error for cases with 640 surface points or more. When the number of surface points was below 640, error increased

unacceptably.

Another factor in initialising our registration algorithm is the quantity of neighbouring points (k), which is set independent of the number of surface points. Specifying different numbers of k affects the quality of the match between the local structures of two surfaces. To analyse this, the quality was tested by varying the number of neighbouring points from minimum 2 points to larger values based on the ratio of given surface, namely $k = [2 + \text{surface points} \times \text{ratio}]$. As shown in Figure 8.8b, our GLTSD-FEM algorithm achieved the lowest error when we set the value of k equal to 8 based on the ratio of 0.009 for 640 surface points. It was found that large values of k reduced the registration performance. We can interpret that assigning a large number of neighbouring points may lead to constructing more complex local structures, making the identification of correct local similarities between MRI and TRUS surfaces somewhat difficult. We can infer that the local structures are best described if the number of neighbouring points falls within the interval of [5 15], since there are only minor changes in the average registration error when k is set to a value in this range. To tune our algorithm, we decided to set the value of k to 5 as default, as this causes a negligible change in the error while speeding up the computation time.

In addition, α and λ as weighting parameters may impact on the robustness of the algorithm in estimating the correspondence matrix and transformation function. The robustness is affected by modifying (α) the importance of global and local structures in cost minimisation of the GLTSD matrix, and by varying (λ) the magnitude of linear and non-linear motions in updating the FEM nodal displacements, respectively. Since the neighbouring points and GLTSD cost matrix are intimately related, the weighting parameter α was defined based on the value of k in the form of $\alpha = k^r$. The regularisation weight λ was initialised

with a range of values based on the length of MRI surface points divided by the ratio of μ . The experimental results for different values of α and λ are shown in Figure 8.8c and Figure 8.8d in turn. The proposed method recorded the lowest errors when $r = 4.15$ and $\mu = 0.8$ from which the optimum values of α and λ could be calculated respectively. The GLTSD-FEM algorithm seems to be less sensitive to variations of these parameters as there were only slight fluctuations in the value of the registration error over the range of values tested.

To evaluate computation speeds, all algorithms were run under the same conditions for the MRI-TRUS fusion of the Robarts image dataset on a PC with a 2.5 GHz Intel Xeon (3 core) and 13 GB of RAM. The average time taken by each method (in seconds) in 38 cases is shown in Figure 8.9.

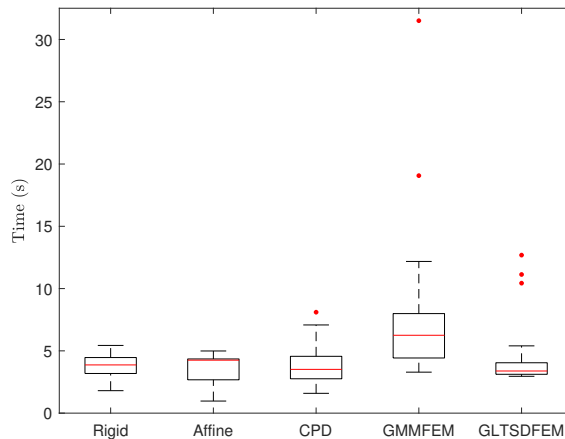


Figure 8.9: Average computation times for all registration methods over 38 cases. The boxplot shows the median, 25th and 75th percentiles, extremes, and outlier values.

The results show that the GLTSD-FEM algorithm has an average computation time comparable with the Rigid, Affine and CPD algorithms, despite having higher accuracy compared with these approaches. This is due to the computationally efficient estimation of the correspondence in a binary form. By contrast, the GMM-FEM algorithm has a computation time almost double the other approaches. Table 8.3 describes the average computation cost

of the GLTSD-FEM for each step.

Table 8.3: Time (seconds) required by each element of the GLTSD-FEM algorithm for MRI-TRUS fusion of Robarts image dataset.

Initialising	Neighbouring Points	FE-meshing	Processing Time of each Iteration	Total Time
0.03 ± 0.07	0.06 ± 0.009	0.65 ± 0.26	0.14 ± 0.08	4.27 ± 2.43

Since the other algorithms tested require at least 100 iterations for convergence due to the choice of a fuzzy scheme for estimating the correspondence matrix, we can conclude that our algorithm is computationally efficient for MRI-TRUS fusion as it converges within 32 iterations, taking less than 5 seconds.

8.4 Summary

In this study, we proposed a surface-based method for robust registration of MRI and TRUS images for clinical applications of image-guided prostate interventions. To establish a one-to-one correspondence between MRI and TRUS surface points, we incorporated global and local similarities of the two point sets into a distance-based cost matrix, which was then minimised as a linear assignment problem. To register the corresponding points, we augmented our algorithm with a physical prior to regularise the non-linear transformation function. This deformed the MRI surface into the TRUS image space in a realistic manner, reflecting the biomechanical states of the prostate. We then designed an optimisation strategy to approximate the optimal solution for both the correspondence matrix and transformation function simultaneously using simulated annealing.

To test the quality of surface matching a dataset of 38 cases from Robarts

Research Institute was used for measuring MSE, HD, and DSC between the MRI and TRUS surfaces. To test the accuracy of the TRUS-MRI fusion, a second dataset from public domain sources (3 image sets from Fedorov et. al³ and 1 image set from Khallaghi et. al⁴), comprising 14 DAPs was used for measuring TRE. We compared our algorithm against state-of-the-art co-registration methods using qualitative and quantitative evaluations of the registration results. The GLTSD-FEM method outperformed other approaches for MRI-TRUS fusion with the lowest average TRE of all methods, and computation times comparable to the state-of-the-art algorithms which had similar workflows.

³<http://doi.org/10.5281/zenodo.16396>

⁴<https://github.com/siavashk/GMM-FEM>

Chapter 9

Conclusions and Future

Directions

The goal of this research has been to develop the necessary techniques to perform reliable MRI-TRUS fusion in order to reduce the uncertainty in image-guided prostate cancer surgical interventions. The MRI-TRUS fusion framework was developed to improve the localisation of anatomical structures within the prostate gland during clinical procedures associated with diagnosis and treatment of prostate cancer. The proposed method consists of two main components, segmentation and registration, with an intermediate step for modelling the prostate surface. Segmentation is used to outline the prostate contour for creating a 3D surface model from each imaging modality, and registration for fusing the created models. For intra-operative procedures, it is important to compute each of these components efficiently to achieve a fast MRI-TRUS fusion model applicable for practical use. This requires automation of the segmentation task over the current manual approaches as the primary step. To address this requirement, three methods, based on elliptical filter models, active shape models (ASMs) and active appearance models (AAMs),

were proposed and discussed in Chapters 4, 5, and 6 respectively for automatic segmentation of the prostate from MR images. After segmentation, a robust surface-based algorithm was developed in Chapter 8 to register 3D models of the prostate, created from segmented MRI and TRUS images, with a high degree of reliability and under a computationally fast optimisation framework.

9.1 Contributions of the Thesis

The main contributions of this thesis are as follows:

- A model-based algorithm was developed to propagate an active appearance model (AAM) of the prostate in MR images for automatic segmentation. While the AAM-based method contributes to improving the accuracy of automatic segmentation, it benefits from a computationally fast iterative optimisation scheme to estimate the model parameters for segmenting new unsighted MRIs. This work was presented at the IEEE International Conference on Image Processing (ICIP 2017) [54].
- An accurate statistical shape model of the prostate was created for use in the AMM-based method. This was achieved by automating the landmark annotation process to create the active shape model (ASM) of the prostate using an algorithm based on rotation at equi-angular increment around the boundary. This modification increased the speed of the segmentation, while preserving the accuracy. The preliminary results of this work were presented at the Annual Scientific Meeting of the Australasian Brachytherapy Group (ABG 2017) [6].
- A filter-based algorithm was developed to approximate the initial shape

of the prostate to an ellipse for fast localisation. The approximated model, when combined with either AAM or ASM approaches, can significantly improve the segmentation speed, since it can constrain the whole search space to a region where the prostate shape is initially segmented by an ellipse.

- A novel surface-based method was developed to non-rigidly register the MRI 3D model to the TRUS surface model for the MRI-TRUS fusion. The proposed GLTSD-FEM algorithm used global-local structural differences between MRI and TRUS 3D models to establish an accurate correspondence, along with a physical prior to compensate for potential deformations of the prostate in a non-linear transformation of corresponding points. Both correspondence and transformation components were estimated under a unified optimisation framework with fast computation time. This work has been submitted to the MICCAI 2019 conference¹.
- The accuracy of the 3D fused model was validated by measuring the targeted registration error (TRE) between pairs of distinct anatomical points (DAPs) within the prostate gland available in both MRI and TRUS images of patients who underwent brachytherapy. An average TRE of 1.8 mm over 14 DAPs in 4 prostate images indicates that the GLTSD-FEM registration algorithm is reasonably robust against deformations of the prostate for transforming the DAPs from MRI to TRUS images. This robustness makes the proposed algorithm a potential candidate for practical use.

¹<http://www.miccai2019.org/>

9.2 Future Work

While the thesis contributes to developing a robust MRI-TRUS fusion method for clinical applications of image-guided prostate procedures, fusion of high-quality pre-operative MRIs with intra-operative TRUS images for image-guided prostate intervention is still an open problem. The computational speeds of the procedures developed in this thesis are fast enough for practical use. Also, the TRE of the GLTSD-FEM is sufficiently accurate for procedures where an uncertainty in position estimation of up to 3mm is clinically acceptable, for example, biopsy or LDR brachytherapy. The current results are based on manual segmentation prior to automatic fusion. Thus, we would expect automatic segmentation to increase the error of TRE by a small degree. In addition to further optimisation of the models developed in the current research, several interesting areas for future research are:

- A more extensive TRE analysis of a larger set of clinical images is desirable. The medical partners of this research study at the Alfred Hospital are currently defining a wider range of visible DAPs on both MRI and TRUS images as an independent reference for a more definitive TRE assessment and model validation.
- In Chapter 8, the proposed GLTSD-FEM algorithm work assumes that both MRI and TRUS images have been fully segmented and their surface models generated. Since it may be difficult to segment some regions of the prostate due to either poor contrast or tissue ambiguity, which are prevalent in TRUS images, obtaining the whole segmented prostate may not be possible in some cases. An extended analysis of MRI-TRUS fusion by our method based on partially segmented images would be valuable.

- To compensate for prostate deformations, a finite element model (FEM) was created to imitate the biomechanical state of the prostate based on a homogeneous elasticity assumption. However, other physical characteristics such as calcification, cysts and tumours within the prostate may cause inhomogeneous elasticity. The model would be improved by incorporating these features into the FEM by an appropriate assignment of the stiffness coefficient for each class by an expert. Research is currently underway by others to estimate the stiffness coefficients using elastography, for example [128, 105, 52].
- The registration method presented in this thesis was compared with two surface-based state-of-the-art approaches. To obtain better insight into the validity and capability of the GLTSD-FEM algorithm, an extended comparison is suggested against other approaches which apply a surface-based MRI-TRUS fusion using different techniques [66, 168, 111].

Bibliography

- [1] Aarnink, R., Pathak, S. D., de la Rosette, J. J., Debruyne, F. M., Kim, Y., and Wijkstra, H. (1998). Edge detection in prostatic ultrasound images using integrated edge maps. *Ultrasonics*, 36(1):635–642.
- [2] Abreu, A. D. C., Oishi, M., Lin-Brandt, M., Cacciamani, G., Ashrafi, A., Shin, T., Freitas, D., Fay, C., Ohe, C., Winter, M., et al. (2018). The urologist’s learning curve for MRI/TRUS fusion guided prostate biopsy. *European Urology Supplements*, 17(2):898–899.
- [3] Acton, S. T. and Ray, N. (2006). Biomedical image analysis: tracking. *Synthesis Lectures on Image, Video, and Multimedia Processing*, 2(1):1–152.
- [4] Ahdoot, M., Lebastchi, A. H., Bloom, J., Gomella, P., Sanford, T., Gurrum, S., Hale, G. R., Gold, S., DiBianco, J., Mehralivand, S., et al. (2019). MP13-02 does MRI-TRUS fusion biopsy obviate the need for systemic biopsy? *The Journal of Urology*, 201(Supplement 4):177–177.
- [5] Akbari, H. and Fei, B. (2012). 3D ultrasound image segmentation using wavelet support vector machines. *Medical Physics*, 39(6Part1):2972–2984.
- [6] Ali Jan Ghasab, M., Paplinski, A., Betts, J., Reynolds, H., and Haworth, A. Towards augmented reality: Intraoperative prostate modelling for biopsy and brachytherapy. 26th Annual Scientific Meeting of the Australasian Brachytherapy Group, 23-25 Feb 2017, Melbourne VIC, Australia.
- [7] Antonelli, M., Cardoso, M. J., Johnston, E. W., Appayya, M. B., Presles, B., Modat, M., Punwani, S., and Ourselin, S. (2019). Gas: A genetic atlas selection strategy in multi-atlas segmentation framework. *Medical Image Analysis*, 52:97–108.
- [8] Baker, S. and Matthews, I. (2004). Lucas-kanade 20 years on: A unifying framework. *International Journal of Computer Vision*, 56(3):221–255.
- [9] Balakrishnan, G., Zhao, A., Sabuncu, M. R., Guttag, J., and Dalca, A. V. (2018). An unsupervised learning model for deformable medical

- image registration. In *Proceedings of the IEEE Conference on Computer Vision and Pattern Recognition*, pages 9252–9260.
- [10] Bandyk, M. G. (2016). Evaluation of MRI/TRUS fusion targeted biopsy versus 12-core standard biopsy with pre-biopsy 1.5 tesla multi-parametric MRI for diagnosis of prostate cancer in a community cancer center. In *ASCO Annual Meeting Proceedings*, volume 34, page 139.
- [11] Barrett, T. (2016). MRI in prostate cancer diagnosis. 488:13–14.
- [12] Bax, J., Cool, D., Gardi, L., Knight, K., Smith, D., Montreuil, J., Sherebrin, S., Romagnoli, C., and Fenster, A. (2008). Mechanically assisted 3D ultrasound guided prostate biopsy system. *Medical Physics*, 35(12):5397–5410.
- [13] Besl, P. J. and McKay, N. D. (1992). Method for registration of 3-d shapes. In *Sensor Fusion IV: Control Paradigms and Data Structures*, volume 1611, pages 586–607. International Society for Optics and Photonics.
- [14] Betts, J. M., Mears, C., Reynolds, H. M., Tack, G., Leo, K., Ebert, M. A., and Haworth, A. (2015). Optimised robust treatment plans for prostate cancer focal brachytherapy. *Procedia Computer Science*, 51:914–923.
- [15] Bjurlin, M. A., Meng, X., Le Nobin, J., Wysock, J. S., Lepor, H., Rosenkrantz, A. B., and Taneja, S. S. (2014). Optimization of prostate biopsy: the role of magnetic resonance imaging targeted biopsy in detection, localization and risk assessment. *The Journal of Urology*, 192(3):648–658.
- [16] Bonet, J. and Wood, R. D. (1997). *Nonlinear continuum mechanics for finite element analysis*. Cambridge University Press.
- [17] Bookstein, F. L. (1989). Principal warps: Thin-plate splines and the decomposition of deformations. *IEEE Transactions on Pattern Analysis and Machine Intelligence*, 11(6):567–585.
- [18] Boubaker, M. B. and Ganghoffer, J.-F. (2017). Bladder/prostate/rectum: Biomechanical models of the mobility of pelvic organs in the context of prostate radiotherapy. In *Biomechanics of Living Organs*, pages 307–324. Elsevier.
- [19] Cao, X., Yang, J., Zhang, J., Wang, Q., Yap, P.-T., and Shen, D. (2018). Deformable image registration using a cue-aware deep regression network. *IEEE Transactions on Biomedical Engineering*, 65(9):1900–1911.

- [20] Catalona, W. J., Smith, D. S., and Ornstein, D. K. (1997). Prostate cancer detection in men with serum PSA concentrations of 2.6 to 4.0 ng/ml and benign prostate examination: enhancement of specificity with free PSA measurements. *Jama*, 277(18):1452–1455.
- [21] Chan, T. F. and Vese, L. A. (2001). A level set algorithm for minimizing the mumford-shah functional in image processing. In *Proceedings IEEE Workshop on Variational and Level Set Methods in Computer Vision*, pages 161–168. IEEE.
- [22] Cheng, R., Turkbey, B., Gandler, W., Agarwal, H. K., Shah, V. P., Bokinsky, A., McCreedy, E., Wang, S., Sankineni, S., Bernardo, M., et al. (2014). Atlas based AAM and SVM model for fully automatic MRI prostate segmentation. In *2014 36th Annual International Conference of the IEEE Engineering in Medicine and Biology Society*, pages 2881–2585. IEEE.
- [23] Cheng, X., Zhang, L., and Zheng, Y. (2018). Deep similarity learning for multimodal medical images. *Computer Methods in Biomechanics and Biomedical Engineering: Imaging & Visualization*, 6(3):248–252.
- [24] Chui, H., Rambo, J., Duncan, J., Schultz, R., and Rangarajan, A. (1999). Registration of cortical anatomical structures via robust 3D point matching. In *Biennial International Conference on Information Processing in Medical Imaging*, pages 168–181. Springer.
- [25] Chui, H. and Rangarajan, A. (2003). A new point matching algorithm for non-rigid registration. *Computer Vision and Image Understanding*, 89(2-3):114–141.
- [26] Churukanti, G. and Siddiqui, M. M. (2015). Prostate cancer: MRI-TRUS fusion biopsy versus 12-core systematic biopsy. *Nature Reviews. Urology*, 12(7):369–371.
- [27] Cohen, D., Mayer, E., Chen, D., Anstee, A., Vale, J., Yang, G.-Z., Darzi, A., et al. (2010). Augmented reality image guidance in minimally invasive prostatectomy. In *International Workshop on Prostate Cancer Imaging*, pages 101–110. Springer.
- [28] Cool, D. W., Zhang, X., Romagnoli, C., Izawa, J. I., Romano, W. M., and Fenster, A. (2015). Evaluation of MRI-TRUS fusion versus cognitive registration accuracy for MRI-targeted, TRUS-guided prostate biopsy. *American Journal of Roentgenology*, 204(1):83–91.
- [29] Cootes, T. F., Edwards, G. J., and Taylor, C. J. (1998). Active appearance models. In *European Conference on Computer Vision*, pages 484–498. Springer.

- [30] Cootes, T. F., Edwards, G. J., Taylor, C. J., et al. (2001). Active appearance models. *IEEE Transactions on Pattern Analysis and Machine Intelligence*, 23(6):681–685.
- [31] Cootes, T. F., Hill, A., Taylor, C. J., and Haslam, J. (1994). Use of active shape models for locating structures in medical images. *Image and Vision Computing*, 12(6):355–365.
- [32] Cootes, T. F., Taylor, C. J., Cooper, D. H., and Graham, J. (1995). Active shape models-their training and application. *Computer Vision and Image Understanding*, 61(1):38–59.
- [33] Cootes, T. F., Taylor, C. J., et al. (2004). Statistical models of appearance for computer vision.
- [34] Cosío, F. A. (2008). Automatic initialization of an active shape model of the prostate. *Medical Image Analysis*, 12(4):469–483.
- [35] Crum, W. R., Hartkens, T., and Hill, D. (2014). Non-rigid image registration: theory and practice. *The British Journal of Radiology*.
- [36] De Craene, M., du Bois d’Aische, A., Macq, B., and Warfield, S. K. (2004). Multi-subject registration for unbiased statistical atlas construction. In *International Conference on Medical Image Computing and Computer-Assisted Intervention*, pages 655–662. Springer.
- [37] De Maesschalck, R., Jouan-Rimbaud, D., and Massart, D. L. (2000). The mahalanobis distance. *Chemometrics and Intelligent Laboratory Systems*, 50(1):1–18.
- [38] De Silva, T., Fenster, A., Cool, D. W., Gardi, L., Romagnoli, C., Samarabandu, J., and Ward, A. D. (2013a). 2D-3D rigid registration to compensate for prostate motion during 3D TRUS-guided biopsy. *Medical Physics*, 40(2):022904.
- [39] De Silva, T., Fenster, A., Cool, D. W., Gardi, L., Romagnoli, C., Samarabandu, J., and Ward, A. D. (2013b). 2D-3D rigid registration to compensate for prostate motion during 3D TRUS-guided biopsy. *Medical Physics*, 40(2):022904.
- [40] de Vos, B. D., Berendsen, F. F., Viergever, M. A., Sokooti, H., Staring, M., and Išgum, I. (2019). A deep learning framework for unsupervised affine and deformable image registration. *Medical Image Analysis*, 52:128–143.
- [41] Dempster, A. P., Laird, N. M., and Rubin, D. B. (1977). Maximum likelihood from incomplete data via the EM algorithm. *Journal of the Royal Statistical Society. Series B (methodological)*, pages 1–38.

- [42] Diaz, K. and Castaneda, B. (2008). Semi-automated segmentation of the prostate gland boundary in ultrasound images using a machine learning approach. In *Medical Imaging 2008: Image Processing*, volume 6914, page 69144A. International Society for Optics and Photonics.
- [43] Dimmen, M., Vlatkovic, L., Hole, K.-H., Nesland, J. M., Brennhovd, B., and Axcrona, K. (2012). Transperineal prostate biopsy detects significant cancer in patients with elevated prostate-specific antigen (PSA) levels and previous negative transrectal biopsies. *BJU International*, 110(2b):E69–E75.
- [44] Dong, J., Cai, Z., and Du, S. (2016). Improvement of affine iterative closest point algorithm for partial registration. *IET Computer Vision*, 11(2):135–144.
- [45] Dowling, J. A., Fripp, J., Chandra, S., Pluim, J. P. W., Lambert, J., Parker, J., Denham, J., Greer, P. B., and Salvado, O. (2011). Fast automatic multi-atlas segmentation of the prostate from 3D MR images. In *International Workshop on Prostate Cancer Imaging*, pages 10–21. Springer.
- [46] Eppenhof, K. A., Lafarge, M. W., Moeskops, P., Veta, M., and Pluim, J. P. (2018). Deformable image registration using convolutional neural networks. In *Medical Imaging 2018: Image Processing*, volume 10574, page 105740S. International Society for Optics and Photonics.
- [47] Fan, J., Cao, X., Xue, Z., Yap, P.-T., and Shen, D. (2018). Adversarial similarity network for evaluating image alignment in deep learning based registration. In *International Conference on Medical Image Computing and Computer-Assisted Intervention*, pages 739–746. Springer.
- [48] Fan, S., Voon, L. K., and Sing, N. W. (2002). 3D prostate surface detection from ultrasound images based on level set method. In *International Conference on Medical Image Computing and Computer-Assisted Intervention*, pages 389–396. Springer.
- [49] Fedorov, A., Khallaghi, S., Sánchez, C. A., Lasso, A., Fels, S., Tuncali, K., Sugar, E. N., Kapur, T., Zhang, C., Wells, W., et al. (2015). Open-source image registration for MRI-TRUS fusion-guided prostate interventions. *International Journal of Computer Assisted Radiology and Surgery*, 10(6):925–934.
- [50] Fiard, G., Hohn, N., Descotes, J.-L., Rambeaud, J.-J., Troccaz, J., and Long, J.-A. (2013). Targeted MRI-guided prostate biopsies for the detection of prostate cancer: initial clinical experience with real-time 3-dimensional transrectal ultrasound guidance and magnetic resonance/transrectal ultrasound image fusion. *Urology*, 81(6):1372–1378.

- [51] Flores-Tapia, D., Thomas, G., Venugopal, N., McCurdy, B., and Pistorius, S. (2008). Semi automatic MRI prostate segmentation based on wavelet multiscale products. In *2008 30th Annual International Conference of the IEEE Engineering in Medicine and Biology Society*, pages 3020–3023. IEEE.
- [52] Fovargue, D., Kozerke, S., Sinkus, R., and Nordsletten, D. (2018). Robust MR elastography stiffness quantification using a localized divergence free finite element reconstruction. *Medical Image Analysis*, 44:126–142.
- [53] Gao, Q., Asthana, A., Tong, T., Hu, Y., Rueckert, D., and Edwards, P. J. (2014). Hybrid decision forests for prostate segmentation in multi-channel MR images. In *International Conference on Pattern Recognition (ICPR)*, pages 3298–3303.
- [54] Ghasab, M. A. J., Paplinski, A. P., Betts, J. M., Reynolds, H. M., and Haworth, A. (2017). Automatic 3D modelling for prostate cancer brachytherapy. In *Image Processing (ICIP), 2017 IEEE International Conference on*, pages 4452–4456. IEEE.
- [55] Ghose, S., Mitra, J., Oliver, A., Martí, R., Lladó, X., Freixenet, J., Vilanova, J. C., Sidibé, D., and Meriaudeau, F. (2012a). A random forest based classification approach to prostate segmentation in MRI. *MICCAI Grand Challenge: Prostate MR Image Segmentation*, 2012.
- [56] Ghose, S., Oliver, A., Martí, R., Lladó, X., Vilanova, J. C., Freixenet, J., Mitra, J., Sidibé, D., and Meriaudeau, F. (2012b). A survey of prostate segmentation methodologies in ultrasound, magnetic resonance and computed tomography images. *Computer Methods and Programs in Biomedicine*, 108(1):262–287.
- [57] Ghose, S., Oliver, A., Mitra, J., Martí, R., Lladó, X., Freixenet, J., Sidibé, D., Vilanova, J. C., Comet, J., and Meriaudeau, F. (2013). A supervised learning framework of statistical shape and probability priors for automatic prostate segmentation in ultrasound images. *Medical Image Analysis*, 17(6):587–600.
- [58] Gold, S., Rangarajan, A., Lu, C.-P., Pappu, S., and Mjolsness, E. (1998). New algorithms for 2D and 3D point matching: Pose estimation and correspondence. *Pattern Recognition*, 31(8):1019–1031.
- [59] Gonzalez, R. C., Woods, R. E., et al. (2002). Digital image processing. *Publishing House of Electronics Industry*, 141(7).
- [60] Goodall, C. (1991). Procrustes methods in the statistical analysis of shape. *Journal of the Royal Statistical Society. Series B (Methodological)*, pages 285–339.

- [61] Gross, R., Matthews, I., and Baker, S. (2005). Generic vs. person specific active appearance models. *Image and Vision Computing*, 23(12):1080–1093.
- [62] Guo, Y., Werahera, P. N., Narayanan, R., Li, L., Kumar, D., Crawford, E. D., and Suri, J. S. (2009). Image registration accuracy of a 3-dimensional transrectal ultrasound-guided prostate biopsy system. *Journal of Ultrasound in Medicine*, 28(11):1561–1568.
- [63] Haskins, G., Kruecker, J., Kruger, U., Xu, S., Pinto, P. A., Wood, B. J., and Yan, P. (2019). Learning deep similarity metric for 3D MR-TRUS image registration. *International Journal of Computer Assisted Radiology and Surgery*, 14(3):417–425.
- [64] Heinrich, M. P., Jenkinson, M., Bhushan, M., Matin, T., Gleeson, F. V., Brady, M., and Schnabel, J. A. (2012). Mind: Modality independent neighbourhood descriptor for multi-modal deformable registration. *Medical Image Analysis*, 16(7):1423–1435.
- [65] Hodge, A. C., Fenster, A., Downey, D. B., and Ladak, H. M. (2006). Prostate boundary segmentation from ultrasound images using 2D active shape models: Optimisation and extension to 3D. *Computer Methods and Programs in Biomedicine*, 84(2):99–113.
- [66] Hu, Y., Ahmed, H. U., Taylor, Z., Allen, C., Emberton, M., Hawkes, D., and Barratt, D. (2012). MR to ultrasound registration for image-guided prostate interventions. *Medical Image Analysis*, 16(3):687–703.
- [67] Hu, Y., Carter, T. J., Ahmed, H. U., Emberton, M., Allen, C., Hawkes, D. J., and Barratt, D. C. (2011). Modelling prostate motion for data fusion during image-guided interventions. *IEEE Transactions on Medical Imaging*, 30(11):1887–1900.
- [68] Hu, Y., Gibson, E., Ghavami, N., Bonmati, E., Moore, C. M., Emberton, M., Vercauteren, T., Noble, J. A., and Barratt, D. C. (2018a). Adversarial deformation regularization for training image registration neural networks. In *International Conference on Medical Image Computing and Computer-Assisted Intervention*, pages 774–782. Springer.
- [69] Hu, Y., Modat, M., Gibson, E., Ghavami, N., Bonmati, E., Moore, C. M., Emberton, M., Noble, J. A., Barratt, D. C., and Vercauteren, T. (2018b). Label-driven weakly-supervised learning for multimodal deformable image registration. In *2018 IEEE 15th International Symposium on Biomedical Imaging (ISBI 2018)*, pages 1070–1074. IEEE.

- [70] Hu, Y., Modat, M., Gibson, E., Li, W., Ghavami, N., Bonmati, E., Wang, G., Bandula, S., Moore, C. M., Emberton, M., et al. (2018c). Weakly-supervised convolutional neural networks for multimodal image registration. *Medical Image Analysis*, 49:1–13.
- [71] Iglesias, J. E. and Sabuncu, M. R. (2015). Multi-atlas segmentation of biomedical images: a survey. *Medical image analysis*, 24(1):205–219.
- [72] Jian, B. and Vemuri, B. C. (2011). Robust point set registration using gaussian mixture models. *IEEE Transactions on Pattern Analysis and Machine Intelligence*, 33(8):1633–1645.
- [73] Jolliffe, I. (2002). *Principal component analysis*. Wiley Online Library.
- [74] Jonker, R. and Volgenant, A. (1987). A shortest augmenting path algorithm for dense and sparse linear assignment problems. *Computing*, 38(4):325–340.
- [75] Kachouie, N. N. and Fieguth, P. (2007). A medical texture local binary pattern for TRUS prostate segmentation. In *2007 29th Annual International Conference of the IEEE Engineering in Medicine and Biology Society*, pages 5605–5608. IEEE.
- [76] Kachouie, N. N., Fieguth, P., and Rahnamayan, S. (2006). An elliptical level set method for automatic TRUS prostate image segmentation. In *2006 IEEE International Symposium on Signal Processing and Information Technology*, pages 191–196. IEEE.
- [77] Kadoury, S., Yan, P., Xu, S., Glossop, N., Choyke, P., Turkbey, B., Pinto, P., Wood, B. J., and Kruecker, J. (2010). Realtime TRUS/MRI fusion targeted-biopsy for prostate cancer: a clinical demonstration of increased positive biopsy rates. In *International Workshop on Prostate Cancer Imaging*, pages 52–62. Springer.
- [78] Kaplan, I., Oldenburg, N. E., Meskell, P., Blake, M., Church, P., and Holupka, E. J. (2002). Real time MRI-ultrasound image guided stereotactic prostate biopsy. *Magnetic Resonance Imaging*, 20(3):295–299.
- [79] Kass, M., Witkin, A., and Terzopoulos, D. (1988). Snakes: Active contour models. *International Journal of Computer Vision*, 1(4):321–331.
- [80] Khallaghi, S., Sánchez, C. A., Rasouljan, A., Nouranian, S., Romagnoli, C., Abdi, H., Chang, S. D., Black, P. C., Goldenberg, L., Morris, W. J., et al. (2015a). Statistical biomechanical surface registration: application to MR-TRUS fusion for prostate interventions. *IEEE Transactions on Medical Imaging*, 34(12):2535–2549.

- [81] Khallaghi, S., Sánchez, C. A., Rasoulian, A., Sun, Y., Imani, F., Khojaste, A., Goksel, O., Romagnoli, C., Abdi, H., Chang, S. D., et al. (2015b). Biomechanically constrained surface registration: Application to MR-TRUS fusion for prostate interventions. *IEEE Transactions on Medical Imaging*, 34(11):2404–2414.
- [82] Kirkpatrick, S., Gelatt, C. D., and Vecchi, M. P. (1983). Optimization by simulated annealing. *Science*, 220(4598):671–680.
- [83] Klein, S., van der Heide, U. A., Lips, I. M., van Vulpen, M., Staring, M., and Pluim, J. P. (2008). Automatic segmentation of the prostate in 3D MR images by atlas matching using localized mutual information. *Medical Physics*, 35(4):1407–1417.
- [84] Korsager, A. S., Fortunati, V., van der Lijn, F., Carl, J., Niessen, W., Østergaard, L. R., and van Walsum, T. (2015). The use of atlas registration and graph cuts for prostate segmentation in magnetic resonance images. *Medical Physics*, 42(4):1614–1624.
- [85] Krebs, J., Mansi, T., Delingette, H., Zhang, L., Ghesu, F. C., Miao, S., Maier, A. K., Ayache, N., Liao, R., and Kamen, A. (2017). Robust non-rigid registration through agent-based action learning. In *International Conference on Medical Image Computing and Computer-Assisted Intervention*, pages 344–352. Springer.
- [86] Kuhn, H. W. (1955). The hungarian method for the assignment problem. *Naval Research Logistics Quarterly*, 2(1-2):83–97.
- [87] Lee, D.-T. and Schachter, B. J. (1980). Two algorithms for constructing a delaunay triangulation. *International Journal of Computer & Information Sciences*, 9(3):219–242.
- [88] Lee, M. C. and Jones, J. S. (2015). Transrectal ultrasound-guided prostate biopsy. In *Surgical Techniques for Prostate Cancer*, pages 7–14. Springer.
- [89] Li, B. and Acton, S. T. (2007). Active contour external force using vector field convolution for image segmentation. *IEEE Transactions on Image Processing*, 16(8):2096–2106.
- [90] Li, H. and Fan, Y. (2018). Non-rigid image registration using self-supervised fully convolutional networks without training data. In *2018 IEEE 15th International Symposium on Biomedical Imaging (ISBI 2018)*, pages 1075–1078. IEEE.
- [91] Litjens, G., Kooi, T., Bejnordi, B. E., Setio, A. A. A., Ciompi, F., Ghafoorian, M., Van Der Laak, J. A., Van Ginneken, B., and Sánchez,

- C. I. (2017). A survey on deep learning in medical image analysis. *Medical Image Analysis*, 42:60–88.
- [92] Liu, X., Langer, D., Haider, M., Van der Kwast, T., Evans, A., Wernick, M., and Yetik, I. (2009a). Unsupervised segmentation of the prostate using MR images based on level set with a shape prior. In *2009 Annual International Conference of the IEEE Engineering in Medicine and Biology Society*, pages 3613–3616. IEEE.
- [93] Liu, X., Langer, D. L., Haider, M. A., Yang, Y., Wernick, M. N., and Yetik, I. S. (2009b). Prostate cancer segmentation with simultaneous estimation of markov random field parameters and class. *IEEE Transactions on Medical Imaging*, 28(6):906–915.
- [94] LoganJennifer, K., ChoykePeter, L., WoodBradford, J., PintoPeter, A., et al. (2014). Magnetic resonance imaging/transrectal ultrasound fusion-guided biopsy of the prostate to detect high-grade cancer. *Journal of Endourology Part B, Videourology*.
- [95] Maes, F., Collignon, A., Vandermeulen, D., Marchal, G., and Suetens, P. (1997). Multimodality image registration by maximization of mutual information. *IEEE Transactions on Medical Imaging*, 16(2):187–198.
- [96] Mahadeo, N. K., Papliński, A. P., and Ray, S. (2012). Model-based pupil and iris localization. In *Proceeding of The 2012 International Joint Conference on Neural Networks (IJCNN)*, pages 1–7. IEEE.
- [97] Manavalan, R. and Thangavel, K. (2011). TRUS image segmentation using morphological operators and DBSCAN clustering. In *2011 World Congress on Information and Communication Technologies*, pages 898–903. IEEE.
- [98] Matthews, I. and Baker, S. (2004). Active appearance models revisited. *International Journal of Computer Vision*, 60(2):135–164.
- [99] Mayer, A., Zholkover, A., Portnoy, O., Raviv, G., Konen, E., and Symon, Z. (2016). Deformable registration of trans-rectal ultrasound (TRUS) and magnetic resonance imaging (MRI) for focal prostate brachytherapy. *International Journal of Computer Assisted Radiology and Surgery*, 11(6):1015–1023.
- [100] McInerney, T. and Terzopoulos, D. (1996). Deformable models in medical image analysis: a survey. *Medical Image Analysis*, 1(2):91–108.
- [101] Miller, M. L., Stone, H. S., and Cox, I. J. (1997). Optimizing Murty’s ranked assignment method. *IEEE Transactions on Aerospace and Electronic Systems*, 33(3):851–862.

- [102] Mitra, J., Kato, Z., Martí, R., Oliver, A., Lladó, X., Sidibé, D., Ghose, S., Vilanova, J. C., Comet, J., and Meriaudeau, F. (2012). A spline-based non-linear diffeomorphism for multimodal prostate registration. *Medical Image Analysis*, 16(6):1259–1279.
- [103] Moon, T. K. (1996). The expectation-maximization algorithm. *IEEE Signal Processing Magazine*, 13(6):47–60.
- [104] Moradi, M., Janoos, F., Fedorov, A., Risholm, P., Kapur, T., Wolfsberger, L. D., Nguyen, P. L., Tempany, C. M., and Wells, W. M. (2012). Two solutions for registration of ultrasound to MRI for image-guided prostate interventions. In *Engineering in Medicine and Biology Society (EMBC), 2012 Annual International Conference of the IEEE*, pages 1129–1132. IEEE.
- [105] Mountris, K. A., Bert, J., Noailly, J., Aguilera, A. R., Valeri, A., Pradier, O., Schick, U., Promayon, E., Ballester, M. G., Troccaz, J., et al. (2017). Modeling the impact of prostate edema on LDR brachytherapy: a monte carlo dosimetry study based on a 3D biphasic finite element biomechanical model. *Physics in Medicine & Biology*, 62(6):2087.
- [106] Munkres, J. (1957). Algorithms for the assignment and transportation problems. *Journal of the Society for Industrial and Applied Mathematics*, 5(1):32–38.
- [107] Myronenko, A. and Song, X. (2010). Point set registration: Coherent point drift. *IEEE Transactions on Pattern Analysis and Machine Intelligence*, 32(12):2262–2275.
- [108] Nouranian, S., Mahdavi, S. S., Spadinger, I., Morris, W. J., Salcudean, S. E., and Abolmaesumi, P. (2015). A multi-atlas-based segmentation framework for prostate brachytherapy. *IEEE Transactions on Medical Imaging*, 34(4):950–961.
- [109] of Health, A. I. and Welfare. Cancer incidence projections: Australia 2011 to 2020.
- [110] Onofrey, J. A., Oksuz, I., Sarkar, S., Venkataraman, R., Staib, L. H., and Papademetris, X. (2016). MRI-TRUS image synthesis with application to image-guided prostate intervention. In *International Workshop on Simulation and Synthesis in Medical Imaging*, pages 157–166. Springer.
- [111] Onofrey, J. A., Staib, L. H., Sarkar, S., Venkataraman, R., Nawaf, C. B., Sprenkle, P. C., and Papademetris, X. (2017). Learning non-rigid deformations for robust, constrained point-based registration in image-guided MR-TRUS prostate intervention. *Medical Image Analysis*, 39:29–43.

- [112] Onofrey, J. A., Staib, L. H., Sarkar, S., Venkataraman, R., and Papademetris, X. (2015). Learning nonrigid deformations for constrained point-based registration for image-guided MR-TRUS prostate intervention. In *Biomedical Imaging (ISBI), 2015 IEEE 12th International Symposium on*, pages 1592–1595. IEEE.
- [113] Osher, S. and Sethian, J. A. (1988). Fronts propagating with curvature-dependent speed: algorithms based on Hamilton-Jacobi formulations. *Journal of Computational Physics*, 79(1):12–49.
- [114] Ozer, S., Langer, D. L., Liu, X., Haider, M. A., Van der Kwast, T. H., Evans, A. J., Yang, Y., Wernick, M. N., and Yetik, I. S. (2010). Supervised and unsupervised methods for prostate cancer segmentation with multispectral MRI. *Medical Physics*, 37(4):1873–1883.
- [115] Papadimitriou, C. H. and Steiglitz, K. (1998). *Combinatorial optimization: algorithms and complexity*. Courier Corporation.
- [116] Papliński, A. P. (1998). Directional filtering in edge detection. *IEEE Transactions on Image Processing*, 7(4):611–615.
- [117] Pathak, S. D., Haynor, D., and Kim, Y. (2000). Edge-guided boundary delineation in prostate ultrasound images. *IEEE Transactions on Medical Imaging*, 19(12):1211–1219.
- [118] Petrou, M. and Kittler, J. (1991). Optimal edge detectors for ramp edges. *IEEE Transactions on Pattern Analysis & Machine Intelligence*, (5):483–491.
- [119] Pieper, S., Lorensen, B., Schroeder, W., and Kikinis, R. (2006). The NA-MIC kit: ITK, VTK, pipelines, grids and 3D slicer as an open platform for the medical image computing community. In *3rd IEEE International Symposium on Biomedical Imaging: Nano to Macro*, pages 698–701. IEEE.
- [120] Qiu, W., Yuan, J., Ukwatta, E., Tessier, D., and Fenster, A. (2012). Rotational-slice-based prostate segmentation using level set with shape constraint for 3D end-firing TRUS guided biopsy. In *International Conference on Medical Image Computing and Computer-Assisted Intervention*, pages 537–544. Springer.
- [121] Qiu, W., Yuan, J., Ukwatta, E., Tessier, D., and Fenster, A. (2013). Three-dimensional prostate segmentation using level set with shape constraint based on rotational slices for 3D end-firing TRUS guided biopsy. *Medical Physics*, 40(7).
- [122] Rangarajan, A., Chui, H., Mjolsness, E., Pappu, S., Davachi, L., Goldman-Rakic, P., and Duncan, J. (1997). A robust point-matching

- algorithm for autoradiograph alignment. *Medical Image Analysis*, 1(4):379–398.
- [123] Rasoulia, A., Rohling, R., and Abolmaesumi, P. (2012). Group-wise registration of point sets for statistical shape models. *IEEE Transactions on Medical Imaging*, 31(11):2025–2034.
- [124] Reynier, C., Troccaz, J., Fournieret, P., Dusserre, A., Gay-Jeune, C., Descotes, J.-L., Bolla, M., and Giraud, J.-Y. (2004). MRI/TRUS data fusion for prostate brachytherapy. preliminary results. *Medical Physics*, 31(6):1568–1575.
- [125] Richard, W. D. and Keen, C. G. (1996). Automated texture-based segmentation of ultrasound images of the prostate. *Computerized Medical Imaging and Graphics*, 20(3):131–140.
- [126] Rueckert, D. and Aljabar, P. (2010). Nonrigid registration of medical images: Theory, methods, and applications [applications corner]. *IEEE Signal Processing Magazine*, 27(4):113–119.
- [127] Rueckert, D., Sonoda, L. I., Hayes, C., Hill, D. L., Leach, M. O., and Hawkes, D. J. (1999). Nonrigid registration using free-form deformations: application to breast MR images. *IEEE Transactions on Medical Imaging*, 18(8):712–721.
- [128] Salcudean, S. E., French, D., Bachmann, S., Zahiri-Azar, R., Wen, X., and Morris, W. J. (2006). Viscoelasticity modeling of the prostate region using vibro-elastography. In *International Conference on Medical Image Computing and Computer-Assisted Intervention*, pages 389–396. Springer.
- [129] Salimi, A., Pourmina, M. A., and Moin, M.-S. (2018). Fully automatic prostate segmentation in MR images using a new hybrid active contour-based approach. *Signal, Image and Video Processing*, 12(8):1629–1637.
- [130] Samavati, N., McGrath, D. M., Jewett, M. A., van der Kwast, T., Ménard, C., and Brock, K. K. (2014). Effect of material property heterogeneity on biomechanical modeling of prostate under deformation. *Physics in Medicine & Biology*, 60(1):195.
- [131] Samiee, M., Thomas, G., and Fazel-Rezai, R. (2006). Semi-automatic prostate segmentation of MR images based on flow orientation. In *2006 IEEE International Symposium on Signal Processing and Information Technology*, pages 203–207. IEEE.
- [132] Schroeder, W. J., Lorensen, B., and Martin, K. (2004). *The visualization toolkit: an object-oriented approach to 3D graphics*. Kitware.

- [133] Serefoglu, E. C., Altinova, S., Ugras, N. S., Akincioglu, E., Asil, E., and Balbay, D. (2013a). How reliable is 12-core prostate biopsy procedure in the detection of prostate cancer? *Canadian Urological Association Journal*, 7(5-6):293–8.
- [134] Serefoglu, E. C., Altinova, S., Ugras, N. S., Akincioglu, E., Asil, E., and Balbay, D. (2013b). How reliable is 12-core prostate biopsy procedure in the detection of prostate cancer? *Canadian Urological Association Journal*, 7(5-6):293–8.
- [135] Shah, A., Zettinig, O., Maurer, T., Precup, C., zu Berge, C. S., Weiss, J., Frisch, B., and Navab, N. (2014). An open source multimodal image-guided prostate biopsy framework. In *Workshop on Clinical Image-Based Procedures*, pages 1–8. Springer.
- [136] Shan, S., Yan, W., Guo, X., Chang, E. I., Fan, Y., Xu, Y., et al. (2017). Unsupervised end-to-end learning for deformable medical image registration. *arXiv preprint arXiv:1711.08608*.
- [137] Sharifi, M., Fathy, M., and Mahmoudi, M. T. (2002). A classified and comparative study of edge detection algorithms. In *Information Technology: Coding and Computing, 2002. Proceedings. International Conference on*, pages 117–120. IEEE.
- [138] Shewchuk, J. R. (2002). Delaunay refinement algorithms for triangular mesh generation. *Computational Geometry*, 22(1-3):21–74.
- [139] Si, H. and TetGen, A. (2006). A quality tetrahedral mesh generator and three-dimensional delaunay triangulator. *Weierstrass Institute for Applied Analysis and Stochastic*, Berlin, Germany, page 81.
- [140] Simpfendörfer, T., Baumhauer, M., Müller, M., Gutt, C. N., Meinzer, H.-P., Rassweiler, J. J., Guven, S., and Teber, D. (2011). Augmented reality visualization during laparoscopic radical prostatectomy. *Journal of endourology*, 25(12):1841–1845.
- [141] Skalski, A., Lagwa, J., Zielinski, T., Kedzierawski, P., and Kuszewski, T. (2013). Automatic prostate segmentation in MR images based on 3D active contours with shape constraints. In *Signal Processing: Algorithms, Architectures, Arrangements, and Applications (SPA), 2013*, pages 246–249. IEEE.
- [142] Sotiras, A., Davatzikos, C., and Paragios, N. (2013). Deformable medical image registration: A survey. *IEEE Transactions on Medical Imaging*, 32(7):1153–1190.
- [143] Sun, Y., Qiu, W., Romagnoli, C., and Fenster, A. (2014). 3D non-rigid surface-based MR-TRUS registration for image-guided

- prostate biopsy. In *Medical Imaging 2014: Image-Guided Procedures, Robotic Interventions, and Modeling*, volume 9036, page 90362J. International Society for Optics and Photonics.
- [144] Sun, Y., Qiu, W., Yuan, J., Romagnoli, C., and Fenster, A. (2015a). Three-dimensional nonrigid landmark-based magnetic resonance to transrectal ultrasound registration for image-guided prostate biopsy. *Journal of Medical Imaging*, 2(2):025002.
- [145] Sun, Y., Reynolds, H., Wraith, D., Williams, S., Finnegan, M. E., Mitchell, C., Murphy, D., Ebert, M. A., and Haworth, A. (2017). Predicting prostate tumour location from multiparametric mri using gaussian kernel support vector machines: a preliminary study. *Australasian physical & engineering sciences in medicine*, 40(1):39–49.
- [146] Sun, Y., Yuan, J., Qiu, W., Rajchl, M., Romagnoli, C., and Fenster, A. (2015b). Three-dimensional nonrigid MR-TRUS registration using dual optimization. *IEEE Transactions on Medical Imaging*, 34(5):1085–1095.
- [147] Sun, Y., Yuan, J., Rajchl, M., Qiu, W., Romagnoli, C., and Fenster, A. (2013). Efficient convex optimization approach to 3D non-rigid MR-TRUS registration. In *International Conference on Medical Image Computing and Computer-Assisted Intervention*, pages 195–202. Springer.
- [148] Tadayyon, H., Lasso, A., Kaushal, A., Guion, P., and Fichtinger, G. (2011). Target motion tracking in MRI-guided transrectal robotic prostate biopsy. *IEEE Transactions on Biomedical Engineering*, 58(11):3135–3142.
- [149] Tian, Z., Liu, L., and Fei, B. (2015a). A fully automatic multi-atlas based segmentation method for prostate MR images. In *Medical Imaging 2015: Image Processing*, volume 9413, page 941340. International Society for Optics and Photonics.
- [150] Tian, Z., Liu, L., and Fei, B. (2015b). A supervoxel-based segmentation method for prostate MR images. In *Medical Imaging 2015: Image Processing*, volume 9413, page 941318. International Society for Optics and Photonics.
- [151] Tian, Z., Liu, L., and Fei, B. (2017). Deep convolutional neural network for prostate MR segmentation. In *Medical Imaging 2017: Image-Guided Procedures, Robotic Interventions, and Modeling*, volume 10135, page 101351L. International Society for Optics and Photonics.
- [152] Tian, Z., Liu, L., Zhang, Z., and Fei, B. (2016). Superpixel-based segmentation for 3D prostate MR images. *IEEE Transactions on Medical Imaging*, 35(3):791–801.

- [153] Tian, Z., Liu, L., Zhang, Z., and Fei, B. (2018). PSNet: prostate segmentation on MRI based on a convolutional neural network. *Journal of Medical Imaging*, 5(2):021208.
- [154] Tikhonov, A. N. (1963). On the solution of ill-posed problems and the method of regularization. In *Doklady Akademii Nauk*, volume 151, pages 501–504. Russian Academy of Sciences.
- [155] Tikhonov, A. N., Goncharsky, A., Stepanov, V., and Yagola, A. G. (2013). *Numerical methods for the solution of ill-posed problems*, volume 328. Springer Science & Business Media.
- [156] Toth, R., Tiwari, P., Rosen, M., Kalyanpur, A., Pungavkar, S., and Madabhushi, A. (2008). A multi-modal prostate segmentation scheme by combining spectral clustering and active shape models. In *Medical Imaging 2008: Image Processing*, volume 6914, page 69144S. International Society for Optics and Photonics.
- [157] Toth, R., Tiwari, P., Rosen, M., Reed, G., Kurhanewicz, J., Kalyanpur, A., Pungavkar, S., and Madabhushi, A. (2011). A magnetic resonance spectroscopy driven initialization scheme for active shape model based prostate segmentation. *Medical Image Analysis*, 15(2):214–225.
- [158] Twining, C. J., Cootes, T., Marsland, S., Petrovic, V., Schestowitz, R., and Taylor, C. J. (2005). A unified information-theoretic approach to groupwise non-rigid registration and model building. In *Biennial International Conference on Information Processing in Medical Imaging*, pages 1–14. Springer.
- [159] Tzimiropoulos, G. and Pantic, M. (2013). Optimization problems for fast AAM fitting in-the-wild. In *Proceedings of the IEEE International Conference on Computer Vision*, pages 593–600.
- [160] Ukimura, O. and Gill, I. S. (2009). Image-fusion, augmented reality, and predictive surgical navigation. *Urologic Clinics*, 36(2):115–123.
- [161] van de Ven, W. J., Hu, Y., Barentsz, J. O., Karssemeijer, N., Barratt, D., and Huisman, H. J. (2013). Surface-based prostate registration with biomechanical regularization. In *Medical Imaging 2013: Image-Guided Procedures, Robotic Interventions, and Modeling*, volume 8671, page 86711R. International Society for Optics and Photonics.
- [162] van de Ven, W. J., Hu, Y., Barentsz, J. O., Karssemeijer, N., Barratt, D., and Huisman, H. J. (2015). Biomechanical modeling constrained surface-based image registration for prostate MR guided TRUS biopsy. *Medical Physics*, 42(5):2470–2481.

- [163] Vese, L. A. and Chan, T. F. (2002). A multiphase level set framework for image segmentation using the mumford and shah model. *International journal of Computer Vision*, 50(3):271–293.
- [164] VY, T. A. A. (1977). Solutions of ill-posed problems. *Washington, DC: VH Winston & Sons*.
- [165] Wahba, G. (1990). *Spline models for observational data*, volume 59. Siam.
- [166] Wang, H., Huang, T.-Z., Xu, Z., and Wang, Y. (2014). An active contour model and its algorithms with local and global Gaussian distribution fitting energies. *Information Sciences*, 263:43–59.
- [167] Wang, H., Suh, J. W., Das, S. R., Pluta, J. B., Craige, C., and Yushkevich, P. A. (2012). Multi-atlas segmentation with joint label fusion. *IEEE transactions on pattern analysis and machine intelligence*, 35(3):611–623.
- [168] Wang, Y., Cheng, J.-Z., Ni, D., Lin, M., Qin, J., Luo, X., Xu, M., Xie, X., Heng, P.-A., et al. (2016). Towards personalized statistical deformable model and hybrid point matching for robust MR-TRUS registration. *IEEE Transactions on Medical Imaging*, 35(2):589–604.
- [169] Warfield, S. K., Zou, K. H., and Wells, W. M. (2004). Simultaneous truth and performance level estimation (staple): an algorithm for the validation of image segmentation. *IEEE Transactions on Medical Imaging*, 23(7):903.
- [170] Xie, Q. and Ruan, D. (2014). Low-complexity atlas-based prostate segmentation by combining global, regional, and local metrics. *Medical Physics*, 41(4):041909.
- [171] Xu, C. and Prince, J. L. (1998). Snakes, shapes, and gradient vector flow. *IEEE Transactions on Image Processing*, 7(3):359–369.
- [172] Xu, S., Kruecker, J., Guion, P., Glossop, N., Neeman, Z., Choyke, P., Singh, A. K., and Wood, B. J. (2007). Closed-loop control in fused MR-TRUS image-guided prostate biopsy. In *International Conference on Medical Image Computing and Computer-Assisted Intervention*, pages 128–135. Springer.
- [173] Xu, S., Kruecker, J., Turkbey, B., Glossop, N., Singh, A. K., Choyke, P., Pinto, P., and Wood, B. J. (2008). Real-time MRI-TRUS fusion for guidance of targeted prostate biopsies. *Computer Aided Surgery*, 13(5):255–264.

- [174] Yan, P., Xu, S., Rastinehad, A. R., and Wood, B. J. (2018). Adversarial image registration with application for MR and TRUS image fusion. In *International Workshop on Machine Learning in Medical Imaging*, pages 197–204. Springer.
- [175] Yan, P., Xu, S., Turkbey, B., and Kruecker, J. (2010). Discrete deformable model guided by partial active shape model for TRUS image segmentation. *IEEE Transactions on Biomedical Engineering*, 57(5):1158.
- [176] Yang, X. and Fei, B. (2012). 3D prostate segmentation of ultrasound images combining longitudinal image registration and machine learning. In *Medical Imaging 2012: Image-Guided Procedures, Robotic Interventions, and Modeling*, volume 8316, page 83162O. International Society for Optics and Photonics.
- [177] Yang, X., Jani, A. B., Rossi, P. J., Mao, H., Curran, W. J., and Liu, T. (2016). Patch-based label fusion for automatic multi-atlas-based prostate segmentation in MR images. In *Medical Imaging 2016: Image-Guided Procedures, Robotic Interventions, and Modeling*, volume 9786, page 978621. International Society for Optics and Photonics.
- [178] Yang, X., Yu, L., Wu, L., Wang, Y., Ni, D., Qin, J., and Heng, P.-A. (2017a). Fine-grained recurrent neural networks for automatic prostate segmentation in ultrasound images. In *Thirty-First AAAI Conference on Artificial Intelligence*.
- [179] Yang, X., Zhan, S., Xie, D., Zhao, H., and Kurihara, T. (2017b). Hierarchical prostate mri segmentation via level set clustering with shape prior. *Neurocomputing*, 257:154–163.
- [180] Yang, Y., Ong, S. H., and Foong, K. W. C. (2015). A robust global and local mixture distance based non-rigid point set registration. *Pattern Recognition*, 48(1):156–173.
- [181] Yu, L., Yang, X., Chen, H., Qin, J., and Heng, P. A. (2017). Volumetric ConvNets with mixed residual connections for automated prostate segmentation from 3D MR images. In *Thirty-First AAAI Conference on Artificial Intelligence*.
- [182] Yuille, A. L. (1990). Generalized deformable models, statistical physics, and matching problems. *Neural Computation*, 2(1):1–24.
- [183] Zaim, A. and Jankun, J. (2007). An energy-based segmentation of prostate from ultrasound images using dot-pattern select cells. In *2007 IEEE International Conference on Acoustics, Speech and Signal Processing-ICASSP'07*, volume 1, pages I–297. IEEE.

- [184] Zettinig, O., Shah, A., Hennemersperger, C., Eiber, M., Kroll, C., Kübler, H., Maurer, T., Milletari, F., Rackerseder, J., zu Berge, C. S., et al. (2015). Multimodal image-guided prostate fusion biopsy based on automatic deformable registration. *International Journal of Computer Assisted Radiology and Surgery*, 10(12):1997–2007.
- [185] Zhang, J., Baig, S., Wong, A., Haider, M. A., and Khalvati, F. (2016). A local ROI-specific atlas-based segmentation of prostate gland and transitional zone in diffusion MRI. *Journal of Computational Vision and Imaging Systems*, 2(1).
- [186] Zhang, K., Song, H., and Zhang, L. (2010). Active contours driven by local image fitting energy. *Pattern Recognition*, 43(4):1199–1206.
- [187] Zhang, S., Yang, Y., Yang, K., Luo, Y., and Ong, S.-H. (2017). Point set registration with global-local correspondence and transformation estimation. In *Proceedings of the IEEE International Conference on Computer Vision*, pages 2669–2677.
- [188] Zhu, Q., Du, B., Turkbey, B., Choyke, P. L., and Yan, P. (2017). Deeply-supervised CNN for prostate segmentation. In *2017 International Joint Conference on Neural Networks (IJCNN)*, pages 178–184. IEEE.
- [189] Zwiggelaar, R., Zhu, Y., and Williams, S. (2003). Semi-automatic segmentation of the prostate. In *Iberian Conference on Pattern Recognition and Image Analysis*, pages 1108–1116. Springer.